

MARTIAN SURFACE ROUGHNESS AND STRATIGRAPHY

by

Ross Alan Beyer

A Dissertation Submitted to the Faculty of the
DEPARTMENT OF PLANETARY SCIENCES

In Partial Fulfillment of the Requirements
For the Degree of

DOCTOR OF PHILOSOPHY

In the Graduate College

THE UNIVERSITY OF ARIZONA

2004

UMI Number: 3145044

INFORMATION TO USERS

The quality of this reproduction is dependent upon the quality of the copy submitted. Broken or indistinct print, colored or poor quality illustrations and photographs, print bleed-through, substandard margins, and improper alignment can adversely affect reproduction.

In the unlikely event that the author did not send a complete manuscript and there are missing pages, these will be noted. Also, if unauthorized copyright material had to be removed, a note will indicate the deletion.

UMI[®]

UMI Microform 3145044

Copyright 2004 by ProQuest Information and Learning Company.

All rights reserved. This microform edition is protected against unauthorized copying under Title 17, United States Code.

ProQuest Information and Learning Company
300 North Zeeb Road
P.O. Box 1346
Ann Arbor, MI 48106-1346

The University of Arizona ®
Graduate College

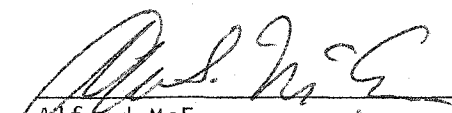
As members of the Final Examination Committee, we certify that we have read the

dissertation prepared by Ross Alan Beyer

entitled MARTIAN SURFACE ROUGHNESS AND STRATIGRAPHY

and recommend that it be accepted as fulfilling the dissertation requirement for the

Degree of Doctor of Philosophy


Alfred McEwen


7/20/2004
date


H. Jay Melosh

7/20/04
date


Victor Baker

7/20/04
date


Robert Strom


7/20/04
date


Elizabeth Turtle

20 July 2004
date

Final approval and acceptance of this dissertation is contingent upon the candidate's submission of the final copies of the dissertation to the Graduate College.

I hereby certify that I have read this dissertation prepared under my direction and recommend that it be accepted as fulfilling the dissertation requirement.


Dissertation Director: Alfred McEwen

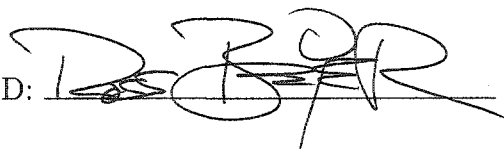
7/20/2004
date

STATEMENT BY AUTHOR

This dissertation has been submitted in partial fulfillment of requirements for an advanced degree at The University of Arizona and is deposited in the University Library to be made available to borrowers under rules of the Library.

Brief quotations from this dissertation are allowable without special permission, provided that accurate acknowledgment of source is made. Requests for permission for extended quotation from or reproduction of this manuscript in whole or in part may be granted by the head of the major department or the Dean of the Graduate College when in his or her judgment the proposed use of the material is in the interests of scholarship. In all other instances, however, permission must be obtained from the author.

SIGNED: _____

A handwritten signature in black ink, appearing to be 'D. B. R.', written over a horizontal line.

ACKNOWLEDGEMENTS

There are a great number of people and organizations that have helped me through the years.

I would like to thank the mentors that have guided me: Wayne Miller, John Dickel, You-Hua Chu, Harley Thronson, Michael Belton, Elizabeth Alvarez, Deborah Domingue, H. Jay Melosh, Robert Strom, Vic Baker, Laszlo Keszthelyi, Elizabeth Turtle, and Alfred McEwen.

I have been fortunate to have been funded throughout my career by many fellowships and grants, all of which ultimately draw their resources from the government of the United States of America. I would like to acknowledge the science programs and policies of our contry, for they have allowed me to learn amazing things and achieve my goals.

All of the research in this Dissertation has made use of NASA's Astrophysics Data System. In a more general sense, I am indebted to the Free and Open Source Software that I have used not only to to perform my scientific research, but also to live my personal life and stay in touch with friends and family.

There were a vast number of computer applications and utilities that I used during my tenure as a graduate student, too numerous and exhausting to list. However, I owe a great deal of thanks to their authors for writing quality software and then releasing it as Free and Open Source Software. It is that spirit of identifying a need or a problem, finding a solution, and then sharing that knowledge with the world that these software authors share with scientists.

There are a great number of friends that I have made through the years, and all have enriched my life. Here is a partial list of those people, please forgive me for not including everyone (these acknowledgements can only be one page). Sean Points, Robert Gruendl, Ian Barton, Daniel Goscha, and David Fong from the Astronomy Department at the University of Illinois. The vast number of friends I have made in Arizona: Jason Barnes, Moses Milazzo, Paul Withers, Fred Ciesla, Terry Hurfordt, David O'Brien, Jani Radebaugh, Pete Lanagan, Josh Emery, Devon Burr, Jonathan Fortney, Gwen Bart, Jennifer Grier, Andy Rivkin, Chris Schaller, Doug Dawson, Celinda Marsh, Zibi Turtle (again), Ralph Lorenz, Barb Cohen, Rob Coker, Betty Pierazzo, Nancy Chabot, Joe Plassmann, Brad Castalia, Linda Hickcox, Kathi Baker, and all the great guys on my soccer team.

Finally, I would like to thank my father, James, my mother, Cheryl, my sister, Amy, and my wife, Rachel, for all of their support and understanding over the years.

DEDICATION

To Rachel

*This accomplishment would have been far more difficult without her
love and support.*

TABLE OF CONTENTS

LIST OF FIGURES	8
LIST OF TABLES	11
ABSTRACT	12
CHAPTER 1 Introduction	14
CHAPTER 2 Meter-scale slopes of candidate MER landing sites	
from point phot clinometry	17
2.1 Overview	17
2.2 Introduction	18
2.3 Method	19
2.3.1 Image Processing	20
2.3.2 Photometry	26
2.3.3 Data Products	28
2.4 Calibration	30
2.4.1 Synthetic Fractal Topography	30
2.4.2 Comparison to Area Phot clinometry	36
2.4.3 Comparison to Previous Landing Sites	43
2.5 Application to MER 2003 Landing Sites	50
2.5.1 Athabasca Valles	50
2.5.2 Elysium Planitia	53
2.5.3 Eos Chasma	57
2.5.4 Gusev Crater	61
2.5.5 Isidis Planitia	66
2.5.6 Melas Chasma	72
2.5.7 Meridiani Planum	72
2.6 Conclusions	77
CHAPTER 3 A profiling phot clinometry technique for determining	
meter-scale topography	79
3.1 Introduction	79
3.2 Method	80
3.3 Applications	83
3.3.1 Flood-formed Dunes in Athabasca Valles	83

TABLE OF CONTENTS – *Continued*

3.3.2	Surface Texture on Surfaces with Dark Slope Streaks	85
3.3.3	Flexure of Europa's Elastic Lithosphere due to Ridge-loading .	86
3.3.4	Comparison of Methods Used to Constrain Aeolian Bedform Morphometry	90
3.4	Conclusion	90
CHAPTER 4 Stratigraphy of Eastern Coprates Chasma, Mars . .		93
4.1	Overview	93
4.2	Introduction	94
4.3	Layer Elevation Measurement Method	98
4.4	Observations	99
4.4.1	Massif in Eastern Coprates Chasma	99
4.4.2	Coprates Chasma, north of massif	112
4.4.3	Coprates Chasma, south of massif	114
4.4.4	Coprates Chasma, west of massif	119
4.4.5	Capri Chasma	125
4.4.6	Topmost Strong Layer Thickness and Extent	129
4.5	Discussion	135
4.5.1	Tectonic Implications	136
4.5.2	Boulders and Blocks	139
4.5.3	Wrinkle Ridges and Topmost Strong Layer Extent	140
4.5.4	Depositional Implications	144
4.6	Conclusions	148
CHAPTER 5 Constraints on the origin of fine layers in Ganges Mensa and Hebes Mensa, Mars		150
5.1	Overview	150
5.2	Introduction	150
5.3	Observations	156
5.3.1	Layer Dip Angles and Surface Slope Angles	156
5.3.2	Dip Angles in a Large Yardang	161
5.3.3	Dip Angles in a Finely Layered Sequence	161
5.4	Discussion	164
5.5	Conclusions	168
REFERENCES		169

LIST OF FIGURES

2.1	Photoclinometry Processing of MOC image M11/02414	24
2.2	MOC image E02/00665, Gusev 1d	38
2.3	MOC image E02/00665, Gusev 1e	38
2.4	MOC image E03/01763, Hematite 2a, b, & c	42
2.5	Viking 1 Landing Site RMS Roughness	45
2.6	Viking 1 Landing Site Slope Distribution	46
2.7	Viking 2 Landing Site RMS Roughness	48
2.8	Viking 2 Landing Site Slope Distribution	48
2.9	Pathfinder Landing Site RMS Roughness	49
2.10	Pathfinder Landing Site Slope Distribution	49
2.11	Athabasca Valles Site RMS Roughness	52
2.12	Athabasca Valles Site Slope Distribution	52
2.13	Athabasca Valles RMS Slope Image Mosaic	54
2.14	Athabasca Valles Point Photoclinometry Examples	55
2.15	Elysium Planitia Site RMS Roughness	56
2.16	Elysium Planitia Site Slope Distribution	56
2.17	Elysium Planitia and Eos Chasma RMS Slope Image Mosaic	58
2.18	Elysium Planitia Point Photoclinometry Examples	59
2.19	Eos Chasma Site RMS Roughness	60
2.20	Eos Chasma Site Slope Distribution	60
2.21	Eos Chasma Point Photoclinometry Examples	62
2.22	Gusev Crater Site RMS Roughness	64
2.23	Gusev Crater Site Slope Distribution	64
2.24	Gusev Crater Point Photoclinometry Examples	65
2.25	Gusev Crater RMS Slope Image Mosaic	67
2.26	Isidis Planitia Site RMS Roughness	69
2.27	Isidis Planitia Site Slope Distribution	69
2.28	Isidis Planitia RMS Slope Image Mosaic	70
2.29	Isidis Planitia Point Photoclinometry Examples	71
2.30	Meridiani Planum RMS Roughness	73
2.31	Meridiani Planum Slope Distribution	73
2.32	Meridiani Planum RMS Slope Image Mosaic	75
2.33	Meridiani Planum Point Photoclinometry Examples	76
3.1	MOC image E10/01384	84
3.2	Topography Profile from E10/01384	84

LIST OF FIGURES – *Continued*

3.3	MOC image M20/00014	87
3.4	Topographic Profile from M20/00014	87
3.5	MOC image M20/00897	88
3.6	Topographic Profile from M20/00897	88
3.7	Lithospheric Flexure Cartoon	91
3.8	Galileo image S0466670126	92
3.9	Topographic Profile from Europa image	92
4.1	Context mosaic of E Coprates Chasma	96
4.2	MOLA map of E Coprates Chasma, annotated	97
4.3	Elevation Measurement Cartoon	100
4.4	Images of westernmost flat-topped area on massif	102
4.5	THEMIS VIS image V03810003	103
4.6	Topmost Strong Layer Examples	104
4.7	MOC image M03/06302 with MOLA track	106
4.8	Topmost Strong Layer Outcrop Plot	108
4.9	MOC image E01/02131	110
4.10	MOC image M08/05277 with MOLA track	111
4.11	MOC image E03/02145	113
4.12	MOC and THEMIS images of a sectioned crater	115
4.13	Slope Map of E Coprates Chasma	117
4.14	Images of the South Rim of Coprates Chasma	118
4.15	THEMIS VIS image V03835003	120
4.16	Images of Promontory West of the Massif	121
4.17	MOC image E02/01171	123
4.18	MOLA map of Coprates Chasma	124
4.19	Locations of the Topmost Strong Layer	126
4.20	Geologic map of E Coprates Chasma	127
4.21	MOC image E05/02164	128
4.22	THEMIS IR image I01875001	130
4.23	Context mosaic of Capri Chasma	131
4.24	MOC image M02/03555	132
4.25	MOC image M09/04970	133
4.26	MOC image M07/01362	134
4.27	Boulders and Blocks in E Coprates Chasma	141
4.28	Resistant Outcrops at Chasmata Rims	143
4.29	Ophir and Aurorae Plana Cartoon	146
5.1	MDIM & MOLA Elevation Map of Ganges Mensa	152
5.2	MOLA Slope Map of Ganges Mensa	153

LIST OF FIGURES – *Continued*

5.3	MDIM & MOLA Elevation Map of Hebes Mensa	154
5.4	MOLA Slope Map of Hebes Mensa	155
5.5	Dipping Layers Cartoon	158
5.6	MOC image M09/03505	159
5.7	MOC image M08/06285	160
5.8	MOC image M03/00648	162
5.9	MOC image M00/02988	163
5.10	MOC image M04/01737 with MOLA profile	165
5.11	Cartoon of tilted and eroded layers	165

LIST OF TABLES

2.1	Slopes from Point Photoclinometry vs. Exact Values, Uniform Albedo	33
2.2	Slopes from Point Photoclinometry vs. Exact Values, Non-Uniform Albedo	35
2.3	Point Photoclinometry Slopes vs. Area Photoclinometry for MOC Images	40
2.4	Viking 1 Landing Site Images	44
2.5	Viking 2 Landing Site Images	45
2.6	Pathfinder Landing Site Images	47
2.7	Athabasca Valles Landing Site Images	51
2.8	Elysium Planitia Landing Site Images	53
2.9	Eos Chasma Landing Site Images	57
2.10	Gusev Crater Landing Site Images	63
2.11	Isidis Planitia Landing Site Images	68
2.12	Meridiani Planum Landing Site Images	74
4.1	Competent Layer Outcrop Elevations	105
4.2	Outcrop Elevations West of Massif	122

ABSTRACT

Orbital datasets can be combined and manipulated to learn about the three-dimensional structure of planetary surfaces, and the processes that have acted on them.

The Mars Orbital Camera (MOC) is providing high-resolution images. These images allow qualitative inspection of features, and contain quantitative information about the shape of the surface. Using a photoclinometry technique derived from a lunar-Lambert photometric function, I am able to obtain estimates of the down-sun slope of each pixel in an image. This technique was calibrated against synthetic topography, compared to an area photoclinometry technique, and applied to the Viking and Pathfinder landing sites. It is a robust technique for obtaining the roughness and slope characteristics of large areas. It was applied to the potential landing sites for the Mars Exploration Rovers to evaluate site safety. The slopes from this point photoclinometry technique can be used to obtain a rough estimate of topography, which I used in a number of studies where topographic information was crucial.

MOC images have shown that layering is pervasive on the martian surface. Mars Orbital Laser Altimeter (MOLA) data can be registered to MOC images to provide elevation constraints on layer outcrops. Such layers are observed in eastern Coprates Chasma both in the chasma rim and in a flat-topped massif. Observations indicate that the chasma stratigraphy consists of thin sequences of resistant layers and intervening thicker sequences of relatively less resistant layers. More resistant units cap the massif against erosion and result in steeper slopes than the weaker units would otherwise allow. These resistant layers can be used as stratigraphic markers which have allowed me to measure the subsidence and tilting of the massif relative to the chasma walls, providing evidence for tectonic motion in this portion of the Valles

Marineris. These outcrops indicate that some of these layers may be analogous to terrestrial flood basalts in both composition and extent.

I have constrained the dip angle of finely layered sequences in Ganges and Hebes Mensae. These layers are either flat lying or dip shallowly, but do not dip steeply, which places some constraints on the origin of these mensae.

CHAPTER 1

Introduction

The surfaces of other worlds have always fascinated me. They represent lands where no person has yet walked (with one nearby exception). They are a distant and yet attainable goal, a frontier to explore and understand. Much of my work has involved using orbital remote sensing data in an attempt to gain an understanding of the surface of Mars at the scale of meters, a length scale comparable to the human scale. I always wondered what might it be like if you were able to stand on that world and explore, and how what you might find would fit into the overall context of what we know.

In the past decade, robotic spacecraft have returned vast amounts of data from Mars, data of myriad varieties. These data contain individual key facts about that planet, and it has been my privilege to gather, understand, and interpret them in an attempt to gain a better understanding both of the current state of the surface of that planet, and some insight into how it got that way.

I was involved with the site selection process for the Mars Exploration Rovers, and it was a direct result of this involvement that I developed the photoclinometry algorithm I describe in chapter 2. This technique is not the most precise shape-from-shading algorithm, but it does have the advantage of being quick and robust. Therefore it can be applied to a large number of images in a short amount of time, ideal for the early stages of landing site selection. It ended up being useful to the work of the site selection committee for the Mars Exploration Rovers, and I look forward to participating in future site selection efforts.

This algorithm for determining the slopes of individual pixels can be extended to find a rough topographic profile. I detail that work in chapter 3, and it has led to some fabulous collaborations. It has allowed me to get involved with a greater number of scientific investigations than I would have managed to accomplish on my

own. The kind of rough topographic profile that this technique produces has often been a key element in these investigations, and it has been exciting to provide meter-scale slope and rough topographic data of Mars and Europa to these investigators.

I have become very interested in the stratigraphic layering below the surface of Mars, and how the geologic history of that planet is laid out in that stack. In my desire to pursue a greater understanding of the stratigraphy of Mars, I have focused on the Valles Marineris canyon system where many layered sequences are exposed.

I used a combination of high-resolution visual imagery, thermal imagery, and accurate topography from laser altimetry to study the layering in Coprates Chasma, as discussed in chapter 4. This study afforded an improved picture of the stratigraphy of this section of Valles Marineris. It shows the diversity of layering, and how tectonic forces acted after those layers had been emplaced.

My success of measuring layers within the slopes of the Valles Marineris led me to investigate the finely layered sequences present in some interior mensae. In chapter 5, I examine the details and implications of this very fine layering in the Ganges and Hebes Mensae, to the best abilities of the present data sets.

All of this work together has been an excellent and enjoyable exploration of the surface of Mars and its geologic history. The process of carrying out these investigations has taught me a great deal, and has raised many new questions that I hope to pursue.

The Shoulders of Giants

In a 1675 letter to Robert Hooke, Isaac Newton wrote, "If I have seen further, it is by standing on the shoulders of giants." Some historians seem to believe that this statement was a veiled insult to Hooke's height (he was short). However, it may have been a variation of a quote from John of Salisbury in 1159, which may itself be from an even older source. John of Salisbury wrote

We are like dwarfs sitting on the shoulders of giants. We see more, and things that are more distant, than they did, not because our sight is superior or because we are taller than they, but because they raise us up, and by their great stature add to ours.

The essence of these quotations has always resonated with me. All of our accomplishments are made possible by those who have gone before us and found the answers and methods that our own work is based on. When I work, I am quite happy not to have had to invent calculus or come up with my own theories for how light interacts with a surface.

In an individual sense, I have thanked those people in the Acknowledgments, and attributed the scientific works of others in the References for this Dissertation. However, there is a body of work that does not quite fit into either of those categories that I am as dependent on and grateful for as either of the others.

That is the realm of computers and information systems, without them this dissertation would not have been possible. From the systems that operate and run the spacecraft whose data I have analyzed, right down to the systems on which I type out these words. Modern planetary science, indeed all modern technological pursuits, depend as much on computers and data systems as they do on fundamental physics.

The FreeBSD operating system has been my operating system of choice for many years. Together with the KDE desktop environment and the VIM editor, these tools have been the computing framework for most of my graduate career. The L^AT_EX documentation preparation system typeset the document that you are reading, and programs like The Gimp, GnuPlot, Xfig, OpenDX, the Generic Mapping Tools Software (Wessel and Smith, 1991, 1998), and POV-Ray helped me produce the figures. The United States Geological Survey's Integrated Software for Imagers and Spectrometers (ISIS) was used to process and view much of the spacecraft data. When existing programs weren't up to producing the information or performing the analysis that I needed, I wrote software myself in the Perl, Java, and C++ programming languages.

CHAPTER 2

Meter-scale slopes of candidate MER landing sites from point photoclinometry

2.1 Overview

This chapter is based on the paper “Meter-scale slopes of candidate MER landing sites from point photoclinometry”, by Ross A. Beyer, Alfred S. McEwen, and Randolph L. Kirk, published in the *Journal of Geophysical Research* (Beyer et al., 2003). Randolph Kirk aided with calibration of this technique, he provided the synthetic fractal topography and used his area photoclinometry technique (Kirk et al., 2003) to provide comparison values. Alfred McEwen aided with the image processing concepts for this technique, he help to resolve haze compensation, albedo variation, and slope azimuth issues. Both co-authors contributed to the overall style and presentation of the manuscript.

Photoclinometry was used to analyze the small-scale roughness of areas that fall within the proposed Mars Exploration Rover (MER) 2003 landing ellipses. The landing ellipses presented in this study were those in Athabasca Valles, Elysium Planitia, Eos Chasma, Gusev Crater, Isidis Planitia, Melas Chasma, and Meridiani Planum. We were able to constrain surface slopes on length scales comparable to the image resolution (1.5 to 12 meters/pixel). The MER 2003 mission had various engineering constraints that each candidate landing ellipse must satisfy. These constraints indicate that the statistical value of the slopes at 5 m baselines are an important criterion. We used our technique to constrain maximum surface slopes across large swaths of each image, and built up slope statistics for the images in each landing ellipse. We are confident that all MER 2003 landing site ellipses in this study, with the exception of the Melas Chasma ellipse, are within the small-scale roughness constraints. Our results have provided input into the landing haz-

ard assessment process. In addition to evaluating the safety of the landing sites, our mapping of small-scale roughnesses can also be used to better define and map morphologic units. The morphology of a surface is characterized by the slope distribution and magnitude of slopes. In looking at how slopes are distributed, we can better define landforms and determine the boundaries of morphologic units.

2.2 Introduction

The Mars Exploration Rover (MER) mission (Crisp et al., 2003) sent two rovers to the surface of Mars in early 2004. In order to reduce the risks of damage during landing, the MER project determined a set of engineering constraints (Golombek et al., 2003) that potential landing ellipses must satisfy. Among these constraints are those which indicate that the percentage of slopes greater than 15 degrees should be minimized. The MER 2003 project had a short list of seven landing ellipses that they had identified for further study, and two of those sites were selected as landing sites for the MER rovers: the Gusev Crater site and the Meridiani Planum site.

The engineering constraints identify slopes on two length scales that are relevant to the mission (Golombek et al., 2003). On length scales of hundreds of meters, a shallow slope would cause increased rolling velocity once the air-bag-enveloped lander touches down and would cause increased bouncing across the surface. Steeper slopes may also contribute to fooling the landing altimeter, causing either early or late rocket firing, dubbed the “mesa” failure scenario. On length scales of several meters, the size of the spacecraft, steep slopes may affect rover deployment and mobility, but also may cause added or increased bouncing.

The Mars Orbital Laser Altimeter (MOLA) (Smith et al., 2001) data are ideal for determining slopes on length scales greater than the instrument’s shot-to-shot distance, which is about 300 m along track and ~ 1 km between tracks at the equator, and have been used to constrain landing site selection (Haldemann and Anderson, 2002; Golombek et al., 2003). Each MOLA shot also contains information about the roughness within the instrument’s footprint via the measured width of

the returned pulse. However, this roughness information has a length scale of about 75 m (Neumann et al., 2003; Garvin et al., 1999).

The best dataset available to evaluate surface slopes on the scale of meters is that of the Mars Orbital Camera (MOC) (Malin and Edgett, 2001). We use a point photoclinometry technique to analyze calibrated narrow angle MOC images, complementing and extending the area photoclinometry and stereogrammetry work by Kirk et al. (2003). Our point photoclinometry method allows us to obtain many slope measurements on all available MOC images and to build up statistics for the images that are in a given landing ellipse. This technique is a significant advance over qualitative evaluation of surface roughness. Our method normalizes the photometry for emission and incidence angles. Our results avoid misleading qualitative evaluations when the pixels of an image are scaled to increase contrast, or “stretched”.

The MOC images used in this study were mostly taken at a local solar time of ~ 2 P.M., but incidence angles vary from 20 to 70 degrees. Additionally most MOC images are nadir-looking and despite off-nadir pointing for some of the images in our study, the emission angles are mostly near zero degrees.

Early in the site selection process this study began with twenty-six candidate landing ellipses, but we will only present information on the seven landing ellipses that made it to the latter stages of the site selection process as well as calibration measurements of the Viking and Pathfinder landing sites. Any of these sites may be reconsidered for future landers.

2.3 Method

Photoclinometry, or shape-from-shading, is the general technique of obtaining slopes or topography from the brightness values in an image. It can be applied in a number of different ways, depending on how the individual brightness values of the pixels are integrated together (or not) and how ambiguity in slope azimuth is resolved, to produce final slope values for those pixels.

The photoclinometry method that we primarily use in this study is that of

“point” photoclinometry. We are measuring the brightness of a single pixel to yield a slope measurement, and we in turn take these point measurements of slope and perform statistical analyses directly on them thereby achieving high spatial resolution.

The term “ n -dimensional photoclinometry” is used where n refers to the dimensionality of the region over which information is built up. When slope information from individual points along a line is modeled, and the result is a height profile, this is known as “profiling” photoclinometry, or one-dimensional photoclinometry. Similarly, when slope information from many points in a grid (or a square region on an image) are modeled, and the result is a topographic surface, this is known as “area” photoclinometry, or two-dimensional photoclinometry. This terminology can be confusing since two-dimensional photoclinometry yields three-dimensional topographic information.

2.3.1 Image Processing

All MOC images that we used have been calibrated with the United States Geological Survey’s Integrated Software for Imagers and Spectrometers (*ISIS* version 010515) (e.g. Eliason et al., 2001; Gaddis et al., 1997). Initial processing of the images involved ingestion of the raw Planetary Data System (PDS) format images, elimination of obviously bad or corrupted pixels, and radiometric calibration. Many images have coarser down-track resolution than cross-track resolution, i.e. pixels do not represent a “square” area on the surface of Mars. In order to compensate for this and to preserve as much original pixel information as possible, we enlarged the image in the down-track direction such that the resolutions in the down-track and cross-track directions were the same. Most of the photometric information that we require for our technique, such as image resolution, incidence angle, and emission angle, was extracted from the labels of the calibrated images, which were derived from the SPICE data (e.g. Acton, 1996, 1999).

Slope statistics vary strongly with spatial scale (Shepard et al., 2001), so we needed to normalize slope statistics measured from images with different resolu-

tions. In order to facilitate this, we found that most of the images near the landing site ellipses had resolutions better than 6 meters per pixel, and so all images were degraded to that resolution. Doing this averages pixel information together, which potentially mixes slope information from many surfaces together, but it also increases the effective baseline over which slopes are measured. These two things together don't significantly contribute to errors in the slopes at these length scales. We explore the variation of slope information with baseline in Section 2.3.3, below.

Our technique measures the slope of each pixel directly. We do not produce a profile of heights in the down-Sun direction, and therefore we completely avoid the cumulative elevation errors involved in profiling photoclinometry. Similarly we are not solving for a smoothed topographic surface like area photoclinometry does. Despite these differences, our technique does share the three major sources of error for photoclinometry that other techniques suffer from: haze, albedo variations, and determination of slope azimuth.

Haze Compensation

The martian atmosphere scatters incident sunlight towards the camera and onto the surface, where it acts as a diffuse illumination source that brightens the image while contributing minimally to topographic shading. Additionally, there must be some scattered light within the MOC camera itself and an offset calibration residual within each image. We think of these factors together as a uniform brightness contribution to the image, or "haze" in the scene. This has an effect on the observed topography which causes both the human eye and our photoclinometry algorithm to misinterpret the value of the slopes. Therefore, we must find an estimate of the haze for each image, and subtract it from the brightness values so that our algorithm does not report gentle slopes where the true slopes are steeper.

Ideally, there would be some independent measure of the haze. For example, if the amplitude of the topography is known from another method such as stereogrammetry, then the haze value can be adjusted until the slopes reported by photoclinometry match those of the topography from stereogrammetry or altimetry (e.g. Kirk

et al., 2003; Soderblom et al., 2002). This approach is not feasible for the present work because our goal is to make photoclinometric slope estimates over much larger areas than can be mapped in stereo. Another way to measure the haze would be to directly estimate it from infrared data. We have found that Viking IRTM opacity estimates provide a consistent lower bound on atmospheric opacities derived from shadows in Viking Orbiter images, but frequently underestimate the visible opacity, so the IR data are not useful for calibrating photoclinometry directly (Kirk et al., 2001).

Another way to gain an estimate of the haze in an image would be to search for true shadows in average-albedo regions in the image and use the DN (data number) value within those areas as the haze value. Using shadows as haze estimators in this way introduces some error since shadows do not have a fixed brightness. The directionality of skylight means that shadow brightnesses vary with how much of the sky the surface sees, but this effect is only on the order of tens of percent (Kirk et al., 2001). A more significant problem for our work is that the 2 P.M. mean local time of the images means that only very steep slopes (greater than $\sim 60^\circ$) would cast true shadows. In addition, manual searching for believable shadows is quite time-consuming. In order to speed the process for the more than one hundred images in this study, we decided to use the minimum pixel value in each scene as the haze value to subtract. If there are no shadows in the image, this darkest pixel may simply be a low-albedo region of the surface, in which case using its brightness overestimates the true haze value of the scene. This provides a good upper limit to the slopes, because overestimating the haze results in measured slopes that will be steeper than the actual slopes.

An advantage of performing our technique on a number of images in the same area is that occasionally an image had anomalously steep model slopes when compared to images of similar or identical terrain. When this happened, we could tell that the automatic haze estimate was quite large, and it could be scaled back to bring the slope statistics of the image into better agreement with other images in the area. Consistency between images doesn't necessarily mean that an accurate haze

estimate has been found, merely that the darkest pixel in each image is comparable.

Compensation for Albedo Variations

Photoclinometry interprets light and dark shading in the scene as slopes on a surface of uniform albedo. If there are patches of significantly darker or lighter material than the majority of the scene, then the photoclinometry algorithm will misinterpret those variations as resulting from topography. Unfortunately, this is quite difficult to compensate for. Albedo variations commonly persist over large areas whereas there is a limit to the extents of dark or bright slopes, therefore changes in brightness over longer distances are more likely to be albedo and it is helpful to filter such broad changes.

In order to minimize the effect of albedo variations and large-scale topography on our measurements, we applied a divide boxcar filter on the image such that the resultant pixels are $D(i, j) = P(i, j) / (S(i, j) / N(i, j))$ where $P(i, j)$ is the original value of the pixel at the i, j location, $S(i, j)$ is the sum of valid points over the box centered at i, j , and $N(i, j)$ is the number of valid points in that box. The size of the boxcar filter was 600 m on a side, which is roughly equivalent to twice the MOLA shot spacing at the surface near the equator. This filtering effectively removes any topographic shading and albedo effects at scales greater than 600 m. MOLA data for the terrain in the landing ellipses indicated that the regional slopes for these areas were flat, and we therefore didn't feel the need to re-insert the MOLA regional slopes for our results. However, this boxcar filtering of the image only normalizes large scale albedo variations, and small scale albedo variations cannot be completely eliminated. An example of an image with initial calibration, automatic haze removal, and boxcar filtering can be found in Figures 2.1a and b.

One way to eliminate small scale albedo differences would be to take advantage of the fact that they are often correlated with color. However, the narrow-angle MOC camera is monochromatic, color differences between dark and bright materials on Mars are subtle, and the martian skylight is colored, so shadows are differently colored as well. For this study, the best way to minimize the problem is to utilize

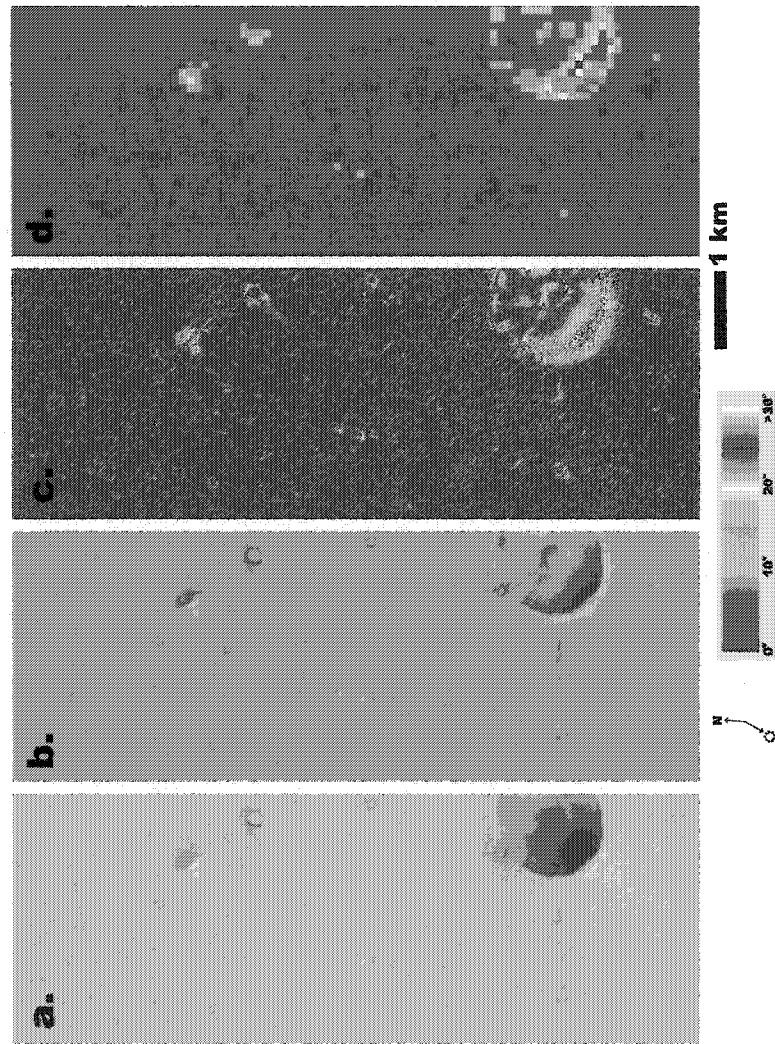


Figure 2.1: These figures contain an example of the processing done in this study. This image is M11/02414, the Pathfinder landing site is on this image. *a.* This image has undergone initial calibration and aspect ratio correction (*ISIS* Level 1). *b.* Haze removal and divide boxcar filtering result in this image. *c.* Absolute value of the slope image. *d.* RMS slope image at 100 m/pixel.

the complex image processing apparatus of the human eye/brain system to identify and avoid images, or regions of images, where severe albedo variations are visually evident.

Small-scale albedo variations that remain within images will cause the slope models to be steeper than they truly are. However, we still derive robust upper limits to slope angles.

Slope Azimuth

The azimuth, or dip direction, of slopes in real terrain will be oriented in various directions. The difficulty is in determining what that azimuth is. If the azimuth of a given slope is not specified, then there isn't a unique brightness for that slope. The work of Kirk et al. (2003) and other area photoclinometry techniques numerically model the azimuth of the slope and the value of the slope itself.

Our technique assumes a very simple geometry in which the azimuths of the model slopes we measure are constrained to be in the direction of solar illumination. Therefore the Sun, the spacecraft, and the portion of the surface imaged define a plane. It is within this plane that we obtain our model slopes. This constraint allows us to have a unique relationship between a given slope and a given brightness. However, since true slopes have a variety of azimuths, we are only measuring the true slope if its azimuth is in the down-Sun direction. For the most part, the azimuths of true slopes will not be in the down-Sun direction, and this assumption of azimuth will cause this technique to report a slope shallower than the true slope.

This is the only key assumption in our technique that underestimates the value of the true slopes. We have evaluated this error for fractal topography, as discussed below in Section 2.4.1, and found it to be only about 2% when compared to bidirectional slopes measured from the fractal topography. It is less than 1% for the smooth surfaces typical of the MER landing sites. This error would be larger if the slope azimuths had a systematic orientation orthogonal to the down-Sun direction.

The measurements from our technique result in bidirectional slopes in the down-Sun direction. In order to obtain an approximation of the adirectional slopes, one

could assume that the slope distribution is isotropic and Gaussian, in which case the adirectional slope distribution would be a factor of $\sqrt{2}$ greater than the bidirectional value (Shepard et al., 2001). Kirk et al. (2003) explicitly calculate the ratio of the adirectional root mean square (RMS) and bidirectional RMS slopes based on their data, and find empirically that this ratio is constant and nearly equal to $\sqrt{2}$. This is a statistical relation over an area that is large compared to the topographic features that contribute to the slopes.

However, in this study we report the bidirectional slope statistics that our technique produces.

2.3.2 Photometry

We start with a lunar-Lambert photometric function after McEwen (1991, 1986) of the form

$$I(\mu, \mu_0, \alpha) = Bo(\alpha) \left[\frac{2L(\alpha)\mu_0}{\mu + \mu_0} + (1 - L(\alpha))\mu_0 \right] \quad (2.1)$$

Where $I(\mu, \mu_0, \alpha)$ is the reflectance function, μ is the cosine of the emission angle ϵ , μ_0 is the cosine of the incidence angle ι , α is the phase angle, $Bo(\alpha)$ is the intrinsic albedo or the value of $I(1, 1, \alpha)$, and $L(\alpha)$ is equal to $Af(\alpha)/[Af(\alpha) + 2B]$, as defined by McEwen (1991). The above equation can be simplified if we create a ratio of the brightness value, I^* , of some topography with slope θ to the brightness of flat topography, I :

$$\frac{I^*}{I} = \frac{\frac{2L(\alpha)\mu_0^*}{\mu^* + \mu_0^*} + (1 - L(\alpha))\mu_0^*}{\frac{2L(\alpha)\mu_0}{\mu + \mu_0} + (1 - L(\alpha))\mu_0} \quad (2.2)$$

This leaves us with two unknowns (the values of μ^* and μ_0^* for the tilted terrain) to be solved for given the value of the ratio I^*/I . These two unknowns can be reduced to one under the assumption, discussed above, that local surface slopes are always in the up- or down-Sun direction. For each pixel in the image, we wish to know the angle, θ , at which the surface is tilted with respect to a flat surface (positive if tilted towards the light source). Since $\mu_0 = \cos(\iota)$ and $\mu = \cos(\epsilon)$, we seek $\mu_0^* = \cos(\iota - \theta)$ and μ^* . With the further simplifying assumption that not only the surface slope direction but also the spacecraft lies in the same plane as the Sun,

we have $\mu^* = \cos(\epsilon \pm \theta)$. Imagine a line that is the projection of the normal vector of the surface being imaged onto this plane. The negative sign then applies when the spacecraft is on the same side of this vertical as the Sun, and the positive sign when it is on the opposite side of the vertical. It is important to note that this expression for μ^* is strictly valid when the emission direction is in the plane defined by the Sun, but will be approximately valid when the emission direction is not far from that plane, in particular, when the emission angle itself is small. Most of the MOC images used in this study have emission angles of less than 1° . Many others are ROTO (Roll-Only Targeted Observations) images where the spacecraft rolled towards the east or west to take off-nadir images and the emission vector was thus close to the roughly east-west Sun direction. Images from mid-phase E07 and onwards, however, were taken from the “Relay- 16” position in which the Mars Global Surveyor (MGS) spacecraft was rotated sixteen degrees off of nadir in a north-south direction. The approximations made in our calculation of the photometric angles will therefore be poorest for these Relay-16 images, but the errors in the brightness calculated for a given slope are still small in a fractional sense.

We use the incidence and emission angles for the image and rotate a hypothetical surface through a range of surface slopes, θ , to generate a suite of known μ^* and μ_0^* values for which the I^*/I ratio is then obtained. From these values, we create a lookup table that allows us to read off a value of θ , quantized to the quarter degree, for any value of I^*/I .

From McEwen (1991) the value of $L(\alpha)$ for most of the images in this study should vary from 0.45 to about 0.65. However, the simulations conducted with fractal topography, discussed below, show that the error resulting from the assumption of fixed L is minor, on the order of ten percent. We therefore estimate the value of $L(\alpha)$ for this study as 0.55.

For some images the emission angle was large, around 20° , which also contributed to a large phase angle, yielding a small value for L . These two effects can cause the I^*/I as a function of θ curve to become double-valued for high values of I^*/I and θ . However, given that these images are of terrain that is flat at hundred-meter

baselines, we seek the solution with the lower slope when this curve is multi-valued.

If (as is generally the case) there is little or no overall tilt to the image region chosen, then the average DN value of this region is a reasonable approximation to the DN of a level surface. We therefore use the ratio of each individual pixel's DN to the average DN as our estimate of I^*/I , which can be compared with our lookup table to yield the value of θ that matches that brightness ratio.

2.3.3 Data Products

Slope Image

When we apply the above methods, we obtain a down-Sun slope value for every pixel in each image that we measure. We effectively have a “slope image” where the value of each pixel is the slope in degrees of the corresponding original image pixel. These slope values can be placed into a greyscale image format such that positive slopes are brighter than 50% grey and negative slopes are darker, so that this slope image effectively becomes a shaded relief image that is independent of viewing angle and illumination angle, but not illumination azimuth. It is also instructive to create an absolute value version of this slope image (Figure 2.1c).

Slope Statistics

We compute the average slope and the root-mean-square (RMS) deviation for each image, as well as creating a plot of what percentage of the image is steeper than a given slope. This gives us an idea of the slope distribution at 6 meters/pixel.

RMS deviation with length scale

We can also continue to reduce the resolution of the images and perform our photoclinometry measurements on them again, as well as measure the slopes at the intrinsic resolution of the image. This allows us to build up information about how slopes change as a function of length scale. Following Shepard et al. (2001) we have

degraded the resolution of the images to 10 m/pixel and 100 m/pixel. These resolution degradations (as well as the degradation to 6 m/pixel) are not achievable via integer summations of the original image pixels, instead a weighted average of the original pixel DN values is used to arrive at the desired degraded resolutions. We have found that the RMS slope deviations for an image at 6, 10, and 100 m/pixel fit the curve of RMS deviations versus length scale produced when we perform integer summing of the image. We use the 6 m/pixel values as a common resolution for the images in this study (there is no integer summable resolution to which all images in the study could be degraded), and we provide the 10 and 100 m/pixel values for comparison with other roughness studies.

RMS Slope Image

In addition to these statistical measures of slope, we also create an “RMS slope image” (Figure 2.1d) that is useful for landing site evaluations. We take the slope image and perform a number of operations that yield an image whose pixels are values in degrees representing the RMS slope of meter-scale slopes within 100 m “footprints” on the image. We take the slope image and square the values. We then run a lowpass boxcar filter, 100 m on a side, through the squared image such that the resultant pixels $L(i, j) = S(i, j)/N(i, j)$. We then take the square root of the pixels in the boxcar filtered image, and sum that image so that the resulting image has 100 m pixels. This is about the length scale that the airbag system will “see” from its first bounce to coming to a halt.

In the process of creating the various absolute value slope images, we found that the meter-scale slopes often changed when the underlying terrain changed morphology. This allowed us to use these slope images to help identify morphologic units, which we found to be consistent with the morphologic units identified by others.

It is important to note that due to our automatic maximum haze estimate and other assumption, the slopes that we report in this study are upper bounds to the down-Sun slope values, not the true slope values.

2.4 Calibration

2.4.1 Synthetic Fractal Topography

It is of interest to assess the accuracy of our point photoclinometry method by applying it to cases in which the slope statistics are known or can be estimated independently. One way to do this is to simulate images from known digital elevation model (DEM) data, which allows us to control the illumination geometry and the presence or absence of albedo variations and haze. Random self-affine fractal surface models (Turcotte, 1997) are especially convenient in that they are easy to generate and contain roughness that varies with horizontal scale in a way that crudely mimics natural surfaces. A series of such fractal models, 1025 elevation posts on a side (in order to simulate images with 1024 pixels on a side), were generated and used both for this study and that of the behavior of two-dimensional photoclinometry by Kirk et al. (2003). The Fourier-domain algorithm of Turcotte (1997) was not used; instead we constructed the terrains by interpolating white noise components to scales increasing by successive factors of two, scaling their variances to produce the desired value of the Hurst exponent, H , and adding them. The Hurst exponent, H , or Hausdorff parameter, governs the variation of roughness with baseline (e.g. Shepard et al., 2001; Turcotte, 1997). We verified that the value of H that results was equal to the intended value to high accuracy by using the Fourier analysis techniques discussed for slope versus baseline analysis by Kirk et al. (2003).

As shown in Table 2.1, these models differed in their RMS slope on a pixel-center-to-pixel-center baseline and also in their value of H . Models with $H = 0.8$ are most similar to the candidate landing sites (Kirk et al., 2003); smaller H corresponds to a greater preponderance of short-baseline roughness. Models based on the $H = 0.8$ fractal but highpass or lowpass filtered to exclude roughness at scales larger or smaller than 16 pixels were also examined. The majority of cases were scaled to have bidirectional RMS slopes (measured between pixel centers as discussed below) of 1° but cases with 10° slopes were also investigated.

Images of the fractal surface models were simulated with incidence and emission

angles of 45° and 0° respectively (typical of the MOC images used in this study) and illumination azimuths both on the sample axis and 22.5° oblique to it. Images were generated both with the $L = 0.55$ lunar-Lambert model used in our point photoclinometry analyses, and with a Minnaert (1941) photometric function with $k = 0.72$, appropriate to the martian surface with a 45° phase angle (Kirk et al., 2000). The difference between the results when these two models are used to synthesize the images gives some idea of the errors caused by our choice of constant $L = 0.55$. Uniform photometric properties were implicit in the generation of the synthetic images (Kirk et al., 2003, Figure 7). To test the effects of spatial albedo variations, a separate bandpass-filtered fractal albedo map was generated and applied multiplicatively to a subset of images (Kirk et al., 2003, Figure 8).

Table 2.1 shows the results for uniform albedo, comparing bidirectional RMS slopes measured directly from the synthetic DEMs to those recovered by point photoclinometry. For each case, two direct measurements are shown, differing in how the fractal DEM data are interpolated in order to calculate slopes. Excellent agreement ($\sim 0.5 - 1\%$ relative error in RMS slope for all but the roughest cases) is obtained between photoclinometry and direct measurements of the slope across the center of each pixel, from the midpoint of one edge to the midpoint of the opposite edge. Not surprisingly, this is equivalent to the average slope over the whole pixel, which enters into the pixel brightness and is then interpreted by photoclinometry. Slopes measured from the center of a pixel to the center of the adjacent pixel are smoother as a natural consequence of the roughness of the fractal surface model at small scales, including across individual pixels. The distinction matters for comparison of our results with those from area photoclinometry (e.g. Kirk et al., 2003). Although this technique produces height estimates at pixel corners, these are usually interpolated to pixel centers (in order to provide a DEM that has the same dimensions as the input image). Slope statistics calculated from these pixel-center heights will tend to be slightly smoother than statistics from point photoclinometry. The magnitude of the effect depends on the roughness of the surface at the single-pixel scale, e.g. on H . If the surface is smooth at this scale, as for our lowpass-filtered case and

surfaces in real images (which are smoothed slightly by the point-spread function of the camera) then the difference between bidirectional slopes calculated by point and area photoclinometry is much smaller than for a strictly fractal surface.

Slopes from Point Photoclinometry vs. Exact Values, Uniform Albedo

“Sun” Azimuth (degrees from sample axis)	Hurst Exponent H		Exact RMS Slope pixel centers pixel edges		Point PC RMS Slope $L = 0.55$ $k = 0.72$		Point PC/Exact Ratio $L = 0.55$ $k = 0.72$	
		Filter						
0°	0.2		1.00°	1.76°	1.76°	1.68°	0.9980	0.9527
	0.5		1.00°	1.62°	1.62°	1.54°	0.9999	0.9505
	0.8		1.00°	1.37°	1.38°	1.31°	1.0040	0.9531
	0.8	Highpass	0.90°	1.30°	1.31°	1.24°	1.0047	0.9510
	0.8	Lowpass	0.52°	0.52°	0.52°	0.50°	1.0002	0.9617
	0.8		9.99°	13.74°	13.62°	13.05°	0.9910	0.9496
22.5°	0.2		1.00°	1.76°	1.77°	1.68°	1.0037	0.9527
	0.5		1.00°	1.62°	1.62°	1.54°	0.9999	0.9505
	0.8		1.00°	1.37°	1.37°	1.31°	0.9967	0.9531
	0.8	Highpass	0.90°	1.30°	1.31°	1.25°	1.0047	0.9587
	0.8	Lowpass	0.52°	0.52°	0.52°	0.49°	1.0002	0.9425
	0.8		9.99°	13.74°	13.43°	12.88°	0.9772	0.9372

Table 2.1: This table shows how the point photoclinometry that we use in this study performs on synthetic fractal terrain illuminated from two different directions. The column labeled “Exact RMS Slope” has two columns, one for the down-Sun RMS slopes measured between pixel centers, and one for the down-Sun RMS slopes measured between pixel edges. “PC” is used as an abbreviation for photoclinometry. There are also two columns for the down-Sun slope measured with our point photoclinometry technique. One using a lunar-Lambert photometric function with $L = 0.55$ to illuminate the topography, and the other using a Minnaert photometric function with $k = 0.72$. The down-Sun RMS slopes are derived from our point photoclinometry method by using a lunar-Lambert photometric function with $L = 0.55$ in both instances. The “Point PC/Exact Ratio” column is a ratio of the results from our point photoclinometry technique and dividing them by the exact down-Sun RMS slope from the pixel edges of the synthetic topography images.

When the roughness of the surface is increased to 10° (pixel center-to-center; this is rougher than all but a few candidate sites described below), point photoclinometry underestimates the bidirectional RMS slope by a little more than 2%. As discussed above, our assumption that slopes lie in the plane of the Sun (where they have the maximum effect on image contrast) is responsible for this small underestimate. Table 2.1 also shows that using our lunar-Lambert photometric model to interpret images formed with a different (but equally Mars-like) Minnaert model results in a roughly 5% error in the bidirectional slope estimates. In the cases shown here, our photometric model causes the slopes to be underestimated. For images of the real surface of Mars, whose photometric behavior varies somewhat with phase angle, we anticipate that slopes will be sometimes overestimated, sometimes underestimated, but are unlikely to be in error by more than a few percent of the actual bidirectional slope value because of this effect. Finally, we note that similar results were obtained for illumination along the sample axis and at 22.5° (a typical solar azimuth for the MOC images), as well as at other azimuths not shown in Table 2.1.

Table 2.2 shows the results for cases where spatially nonuniform albedo was introduced into the images. A RMS albedo variation of 0.63% of the mean was selected for the test; this is the amount of brightness variation that would also result from a slope of 0.5° . The increase in inferred bidirectional RMS slope, from 1.31° to 1.41° is precisely what is expected in our simulation: because the true roughness and albedo-related “slopes” are independent, their variances add, giving a total bidirectional RMS slope estimate of $\sqrt{1.31^2 + 0.5^2} = 1.41$. In reality, albedo variations may not always be independent of roughness. Albedo changes can correspond to compositional changes, and different geologic materials can have different roughness properties.

Slopes from Point Photoclinometry vs. Exact Values, Non-Uniform Albedo								
“Sun” Azimuth (degrees from sample axis)	Hurst Exponent H	Fractional Albedo Variation	Exact RMS Slope		Point PC RMS Slope		Point PC/Exact Ratio	
			pixel centers	pixel edges	$L = 0.55$	$k = 0.72$	$L = 0.55$	$k = 0.72$
0°	0.8	0	1.00°	1.37°	1.37°	1.31°	0.9940	0.9531
	0.8	0.0063	1.00°	1.37°	1.47°	1.41°	1.0704	1.0258
22.5°	0.8	0	1.00°	1.37°	1.39°	1.31°	1.0110	0.9531
	0.8	0.0063	1.00°	1.37°	1.47°	1.40°	1.0664	1.0186

Table 2.2: This table shows how the point photoclinometry that we use in this study performs on the synthetic fractal terrain when albedo variations are added to the artificial surface. With the exception of the “Fractional Albedo Variation” column, the columns are identical to those in Table 2.1.

Although the amplitude (and spatial distribution) of albedo variations in a given real image will certainly differ from that assumed in this simulation, if this amplitude can be estimated then a similar calculation can be used to estimate the apparent roughening that will result. The magnitude of this albedo-induced apparent slope is independent of Sun direction, because point photoclinometry always gives the slope in the Sun direction rather than in a fixed direction. For area photoclinometry, in contrast, the albedo-induced roughening is much greater when the Sun crosses the slope baseline (e.g., the sample axis) at an angle. However, digital filtering of the DEM to suppress the artifacts due to albedo variations yields slope errors that are comparable to those for point photoclinometry regardless of the solar azimuth (Kirk et al., 2003).

2.4.2 Comparison to Area Photoclinometry

It is also of interest to compare slope estimates from our point photoclinometry with an independently developed method in cases based on real images of Mars. For such comparisons, we are of course not privy to the “true” slope distributions but can determine whether our results are consistent with other methods. In particular, we compared our results with those obtained by Kirk et al. (2003) from the same images by using area photoclinometry. It is useful to do such comparisons in several ways. By choosing an image in which albedo variations are minimal and using a relatively precise haze estimate obtained by comparing the image to a stereo DEM of the area (Kirk et al., 2003) we can establish whether point and area photoclinometry are as consistent for real martian topography as they are for synthetic, fractal surfaces. By relying instead on our darkest-pixel estimate for the haze we can quantify the effect this has on the accuracy of slopes. Finally, by looking at other areas with more extreme albedo variations, we can say something about the relative sensitivity of the two methods to such effects.

The area photoclinometry technique has a number of advantages over our point photoclinometry. It allows for the effect of cross-Sun slopes on brightness, rather than assuming all brightness variation comes from slopes up- or down-Sun, which is

true to first order but not precisely true. Area photoclinometry allows the modeling of slopes cross-Sun as well as down-Sun, and hence allows determination of adirectional slopes and slopes in particular baselines not tied to the Sun. The cross-Sun slopes will always be more weakly determined than those down-Sun since they have only a second order effect on brightness and most of the cross-Sun information comes from continuity of the surface.

The area photoclinometry method also suffers from the problems of haze and albedo, but in some ways they are easier to handle. The elevation model produced by the area method can be compared with an a priori DEM from stereo or altimetry in order to calibrate the haze by requiring that the heights of resolved features agree. Area photoclinometry assumes a constant albedo surface and is not immune to albedo-related artifacts. However, the DEM that is generated makes albedo artifacts very apparent as nonsensical topographic “stripes”. Finding these “stripes” is an excellent quality check, and makes it possible to reduce such artifacts by tailored filtering. In this process, stripes are isolated from other topography by first filtering the DEM with a lowpass filter along their length and then with a highpass filter across their narrowest extent. The estimated stripe component can then be subtracted from the original DEM. This filtering process must in general be done several times, each step removing stripes in a particular size range. Filtering reduces the erroneous contribution to slopes in the stripe (down-Sun) direction, and even more dramatically reduces the much greater errors in slopes along baselines that cut across the stripes.

Two portions of the MOC image E02/00665, which is in the Gusev Crater landing ellipse, were measured with both techniques. Kirk et al. (2003) refer to the portion of smooth cratered plains in Thira Crater as *Gusev 1d* (Figure 2.2), and the knobby etched plains south of Thira Crater as *Gusev 1e* (Figure 2.3), as do we.

Table 2.3 shows that area and point photoclinometry with the same haze estimates yield essentially identical bidirectional slope estimates for the smoother region, *Gusev 1d*, while the point photoclinometry bidirectional slope for the rougher region, *Gusev 1e*, is about 5% lower than that from the area method. The tendency

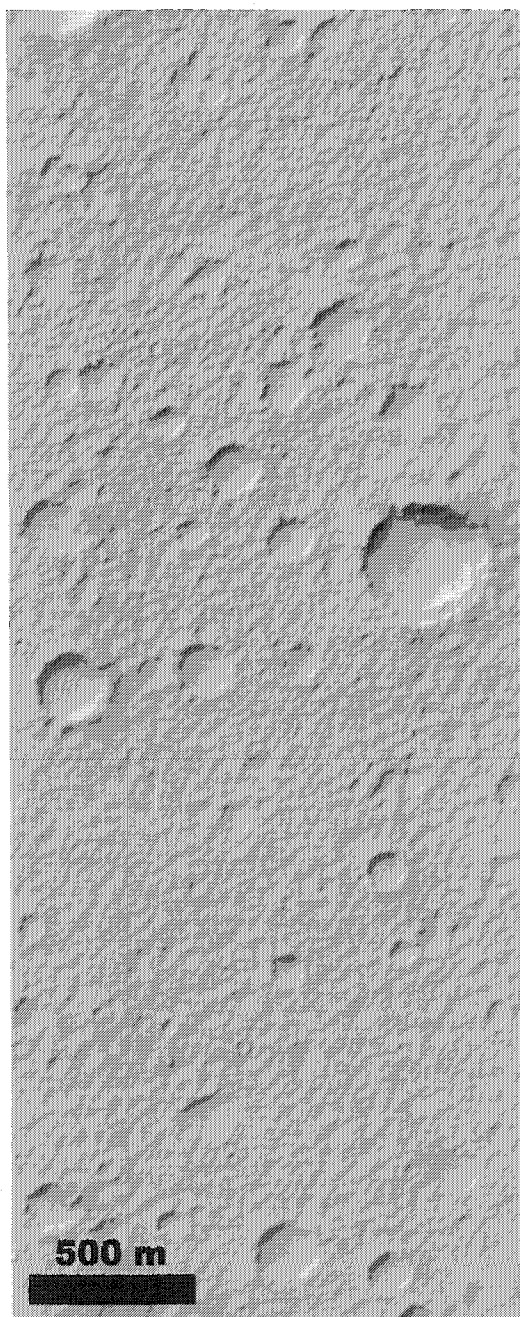


Figure 2.2: Portion of MOC image E02/00665 in Gusev Crater, referred to as image *Gusev 1d* by Kirk et al. (2003) and here.

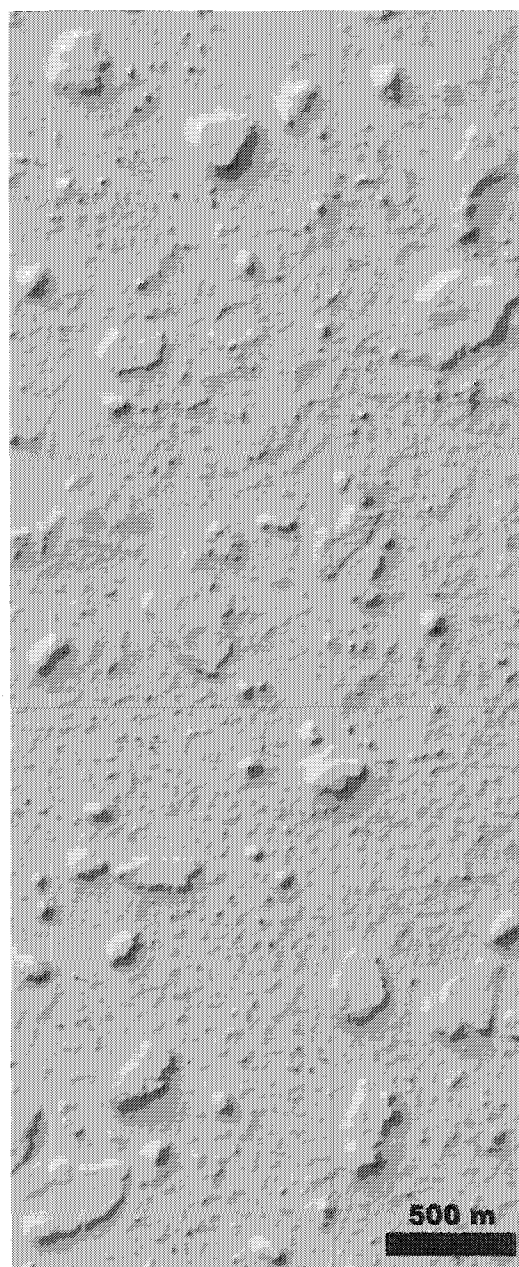


Figure 2.3: Portion of MOC image E02/00665 in Gusev Crater, referred to as image *Gusev 1e* by Kirk et al. (2003) and here.

of point photoclinometry to underestimate steeper slopes is well understood as discussed above, and this result is generally consistent with our fractal simulations shown in Table 2.1. Given the $\leq 5\%$ slope errors that may be introduced by our choice of photometric model, the agreement between results for Gusev is surprisingly good given the same haze estimate.

Point Photoclinometry Slopes vs. Area Photoclinometry for MOC Images						
MOC Image			Darkest	<i>Kirk et al.</i>	Point PC RMS Slope	
Region	Description	<i>Kirk et al.</i> Haze	Pixel Value	Area PC RMS Slope	<i>Kirk et al.</i> Haze	Darkest Pixel Haze
E02/00665						
Gusev 1d	Cratered plains, albedo variations minimal	0.087	0.120	4.20°	4.20°	7.59°
Gusev 1e	Knobby etched plains, albedo variations minimal	0.087	0.085	9.35°	8.87°	8.53°
E03/01763						
Hematite 2a	Smooth plains, albedo variations severe	0.086	0.157	3.10°	2.06°	6.56°
Hematite 2b	Smooth plains, albedo variations moderate	0.086	0.175	1.25°	1.04°	8.04°
Hematite 2c	Plains with rougher outcrops albedo variations moderate	0.086	0.178	2.21°	2.46°	16.80°

Table 2.3: This table shows the comparison between the down-Sun slopes of the Kirk et al. (2003) area photoclinometry, and the down-Sun slopes of this study's point photoclinometry on the same image regions. This table also shows the results of point photoclinometry using both the more precise haze estimates of Kirk et al. (2003), and the darkest pixel haze values that we use in this study. The region names that are used here are the same names as those used and defined by Kirk et al. (2003).

When we use the darkest or minimum pixel value in the scene as the haze estimate, our point photoclinometry method yields different results. Comparing these results for the Gusev image regions to those using the Kirk et al. (2003) haze estimate indicates how the bidirectional RMS slope values in this study for the landing ellipses are, in general, providing an upper limit to the slopes. In the case of *Gusev 1e*, the darkest pixel haze estimate and the Kirk et al. (2003) haze estimate are similar, yielding bidirectional RMS slopes that are similar. However, in *Gusev 1d*, the darkest pixel haze is much greater than the Kirk et al. (2003) haze, and the resultant bidirectional RMS slope is much greater as well. These portions of the E02/00665 image in Gusev Crater are representative of the best case for our technique. There appear to be no albedo variations complicating the surface, and so the major contribution to error is the haze. This image is also representative in that the haze estimate from the darkest pixel either does a good job of estimating the haze, or overestimates it, yielding upper limits to the bidirectional RMS slopes.

The difference in haze estimates and RMS slopes from photoclinometry illustrates the relationship between the slope error and the haze. The RMS slope is going to be inversely proportional to the difference between the average (flat) DN and the assumed haze DN (i.e., raising the haze estimate increases the apparent slope).

Also in Table 2.3 are measurements of E03/01763 in the Meridiani Planum landing site. These image portions (Figures 2.4a, 2.4b, and 2.4c) show how albedo variations will affect photoclinometric measurements. We know that the terrain in these images consists of relatively smooth plains, and so the shading contrasts are from albedo variations. Still, both the area photoclinometry of Kirk et al. (2003) and the point photoclinometry of this study yield similar results. This is with the resultant DEMs from area photoclinometry destriped to minimize albedo effects. Without these corrections, the bidirectional RMS slopes from area photoclinometry are greater.

However, when we use the darkest pixel haze estimate for point photoclinometry in these regions of E03/01763, we get a high value, and the bidirectional RMS slopes

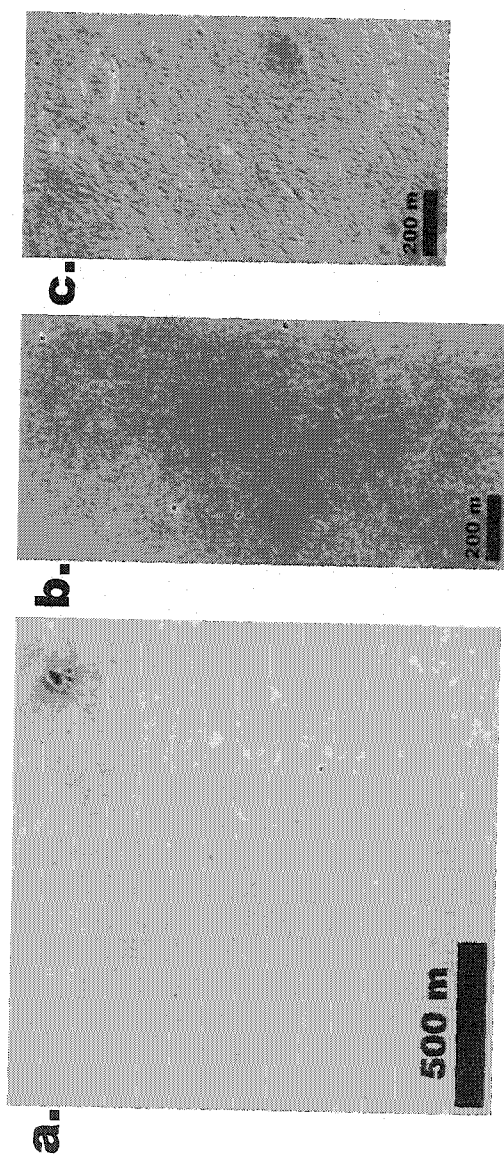


Figure 2.4: Portions of MOC image E03/01763 in Meridiani Planum. Figures *a*, *b*, and *c* are referred to as *Hematite 2a*, *Hematite 2b* and *Hematite 2c* by Kirk et al. (2003) and in Table 2.3.

reported are significantly greater than those reported when a more reasonable haze estimate is used. This again illustrates how haze is the biggest source of error, but that albedo variations can magnify that error.

The results of both area and point photoclinoetry when the Kirk et al. (2003) haze estimates are used compare reasonably well to Kirk et al. (2003) stereo estimates of slope in a few other areas of the ellipse. These were $\sim 1.5 - 2.5^\circ$ but contained estimated errors of $1 - 1.5^\circ$ indicating the slopes are very low and hard to measure in this region.

Thus, the slope estimates from photoclinoetry of either type are clearly heavily influenced by albedo variations and are likely to be severe overestimates. One can look at Figure 2.4a and 2.4b and see that Figure 2.4a is probably not any rougher in reality than Figure 2.4b, it merely has more albedo variation. Nevertheless, even these “contaminated” slope estimates are very smooth, so the conclusions about the safety of the Meridiani Planum site (that are discussed below in §2.5.7) are secure.

The advantage of our point photoclinoetry method over the area photoclinoetry method in this type of study is that it is easier and faster to apply to entire images, giving much better areal coverage.

2.4.3 Comparison to Previous Landing Sites

In order to gain another estimate for the precision of our technique, we decided to apply it to MOC images taken of the regions around the Viking 1, Viking 2, and Pathfinder landing sites. This allowed us to make good use of the only known areas of “ground truth” on Mars as benchmarks for our technique before we attempted to apply it to the landing ellipses for the MER 2003 mission.

Viking 1

Table 2.4 shows the MOC images that were near the location of the Viking 1 landing site (Morris and Jones, 1980; Zeitler and Oberst, 1999; Parker et al., 1999; Parker and Kirk, 1999). Based on the information from the Viking 1 lander’s leg stroke

Viking 1 Landing Site Images

MOC Image	Resolution (m/pixel)	Incidence Angle ($^{\circ}$)	Portion Measured
SP2/38303	4.97	66.74	all
M02/04443	1.497	39.63	all
M03/04873	1.492	43.16	all
M04/02209	1.496	46.93	all
M09/05589	1.497	54.87	all
M12/00448	1.608	49.52	all

Table 2.4: This table contains the MOC Image Numbers, their resolution in meters per pixel and their incidence angle in degrees, as well as an indication of how much of the image was measured.

gauges and camera measurements of the horizon, the local surface slope from one footpad to another (about 2.5 m) is about 1° (Shorthill et al., 1976a). Binder et al. (1977) indicate a more general slope to the area of 1.5° towards the northwest. The lander-stereo-derived topographic map of Binder et al. (1977, Figure 5), indicates that the steepest slopes that can be found are about 10° , with most slopes less than that.

Our measurements in Figures 2.5 and 2.6 show the relative smoothness of the Viking 1 landing site images. The maximum estimate of bidirectional RMS slopes in the images that we measured was $\sim 6^{\circ}$ on length scales of 1.5 m. Additionally, $\sim 90\%$ of the 6 m length scale slopes in these images are less than 10° .

Viking 2

Near the proposed location of the Viking 2 lander (Parker and Kirk, 1999; Oberst et al., 2000), we measured the images listed in Table 2.5. The Viking 2 landing site is very flat and has less than 1 m of relief to a radial distance of 100 m from the lander (Mutch et al., 1977). However, based on lander leg stroke, guidance system information, and horizon measurements the lander itself is at a 6° tilt (Shorthill et al., 1976b). It is thought that one of the footpads is either perched on a rock or in a depression.

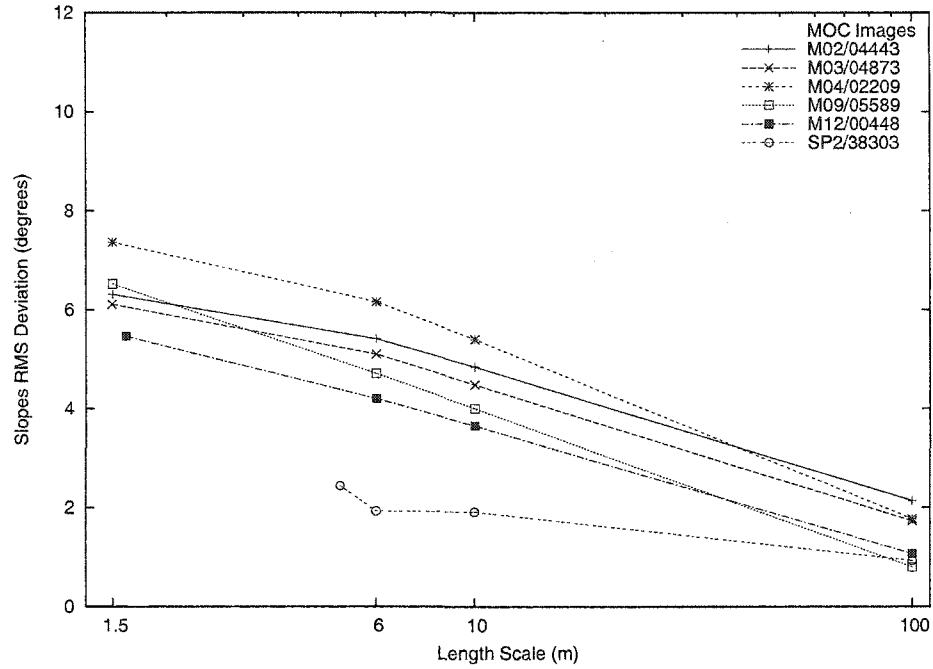


Figure 2.5: Viking 1 Landing Site RMS Roughness. This figure shows the RMS slope deviation in degrees calculated from the slopes in each of the images listed. Slopes statistics are obtained at longer length scales by reducing the resolution in the images, and performing the photoclinometry technique on those reduced resolution images.

Viking 2 Landing Site Images

MOC Image	Resolution (m/pixel)	Incidence Angle (°)	Portion Measured
M02/01764	1.569	47.81	all
M03/07241	1.565	58.93	all
M09/02236	3.136	75.13	all
M11/01288	4.7	75.10	all
M12/00485	1.569	72.04	all
M13/00163	6.265	67.80	all

Table 2.5: This table contains the MOC Image Numbers of all the images in the Viking 2 Landing site area for this study.

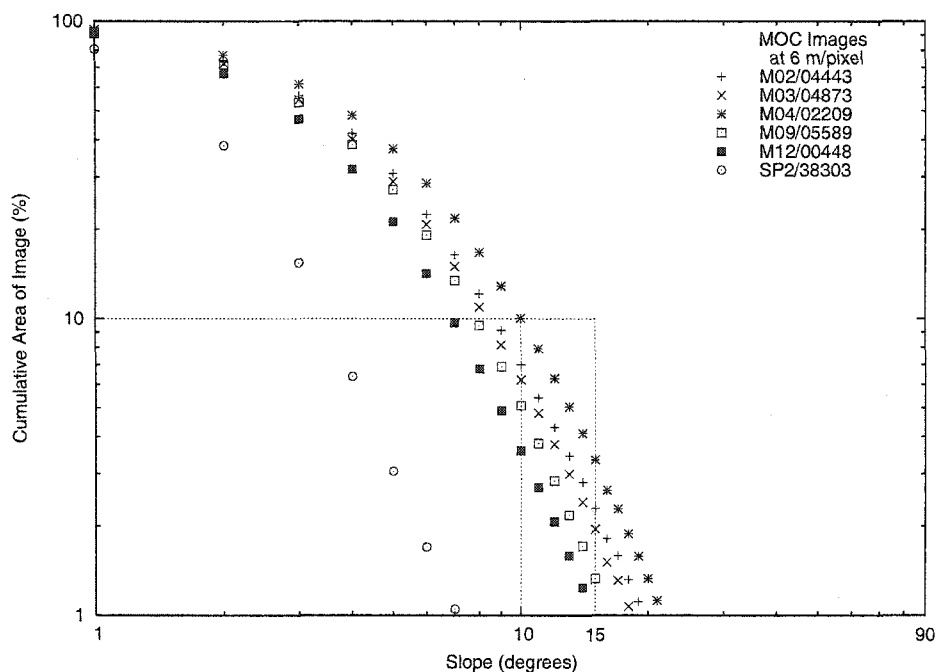


Figure 2.6: Viking 1 Landing Site Slope Distribution. This figure illustrates what percentage of an image has slopes steeper than some value. The dashed lines are guides to show where only ten percent of an image is steeper than 10° and 15° respectively. Since all the curves for images in the Viking 1 landing site pass within the box defined by the 15° guides, then in all the images less than 10% of their slopes are steeper than 15° . In addition to the plot of RMS roughness, this kind of plot gives an idea of the distribution of steep slopes in each image.

Pathfinder Landing Site Images			
MOC Image	Resolution (m/pixel)	Incidence Angle ($^{\circ}$)	Portion Measured
SP1/23703	2.549	48.83	all except for the 1.3 km diameter crater
M08/01772	1.488	50.62	all
M10/00740	1.489	52.05	all
M10/03058	1.567	51.56	all
M11/01311	1.497	49.27	all
M11/02414	1.575	47.92	all except for the 1.5 km diameter crater

Table 2.6: This table contains the MOC Image Numbers of all the images in the Pathfinder Landing site area for this study.

The statistics in Figures 2.7 and 2.8 show how our technique reports lower maximum bidirectional RMS slopes for the Viking 2 landing area than for the Viking 1 area. Our estimate of the maximum bidirectional RMS slopes at the shortest length scales is about 4° , and at length scales of 6 m, more than 90% of the slopes in these images are less than 10° .

Pathfinder

The images in Table 2.6 were close to or overlapping the Pathfinder landing site (Parker and Kirk, 1999). Stereo images from the Imager for Mars Pathfinder (IMP) were used to determine the topography in the inner area around the lander, and it was determined that the RMS slope value was $\sim 4^{\circ}$ (Kirk et al., 1999; Ward et al., 1999; Golombek et al., 1999; Smith et al., 1997, plate 4).

Our measurements of these MOC images are in Figures 2.9 and 2.10. Our estimation of the maximum bidirectional RMS slopes at the smallest length scales is $\sim 7^{\circ}$, and almost all of the slopes in these images are less than 15° and most are less than 10° .

Our results for the Viking 1, Viking 2, and Pathfinder landing sites show those

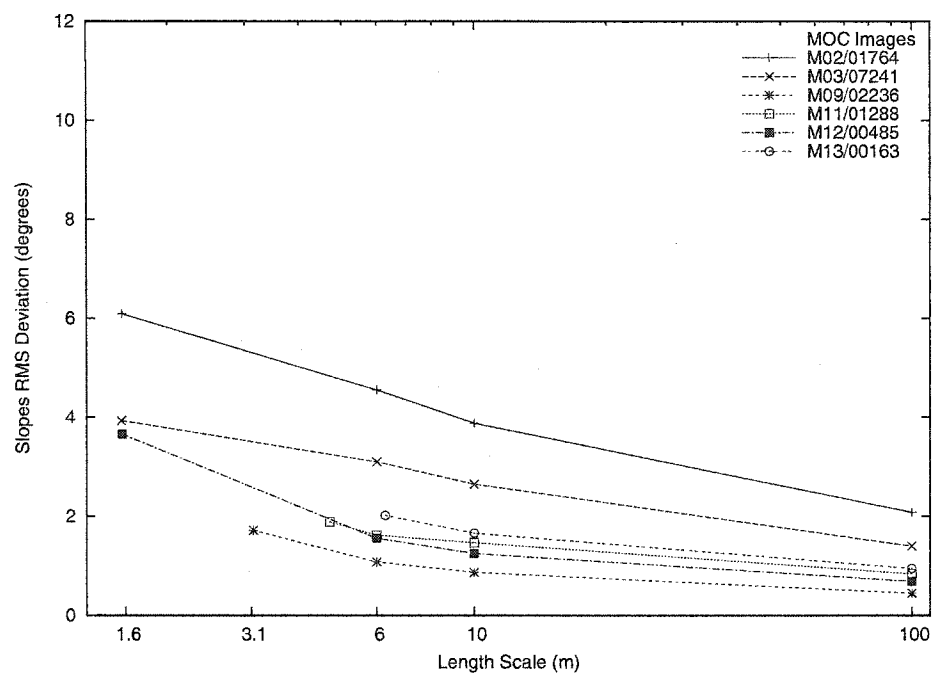


Figure 2.7: Viking 2 Landing Site RMS Roughness

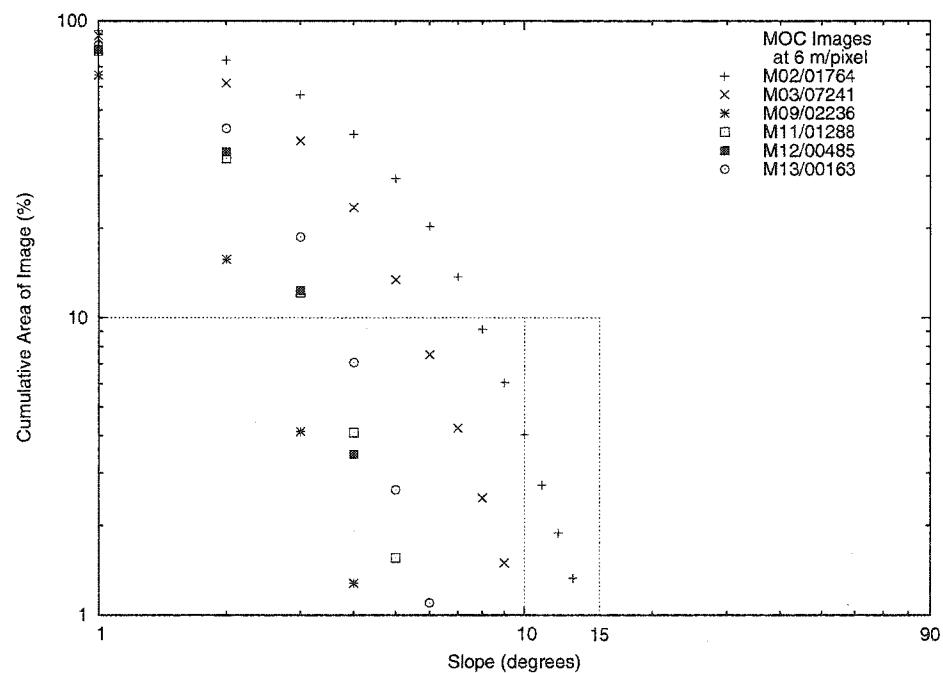


Figure 2.8: Viking 2 Landing Site Slope Distribution.

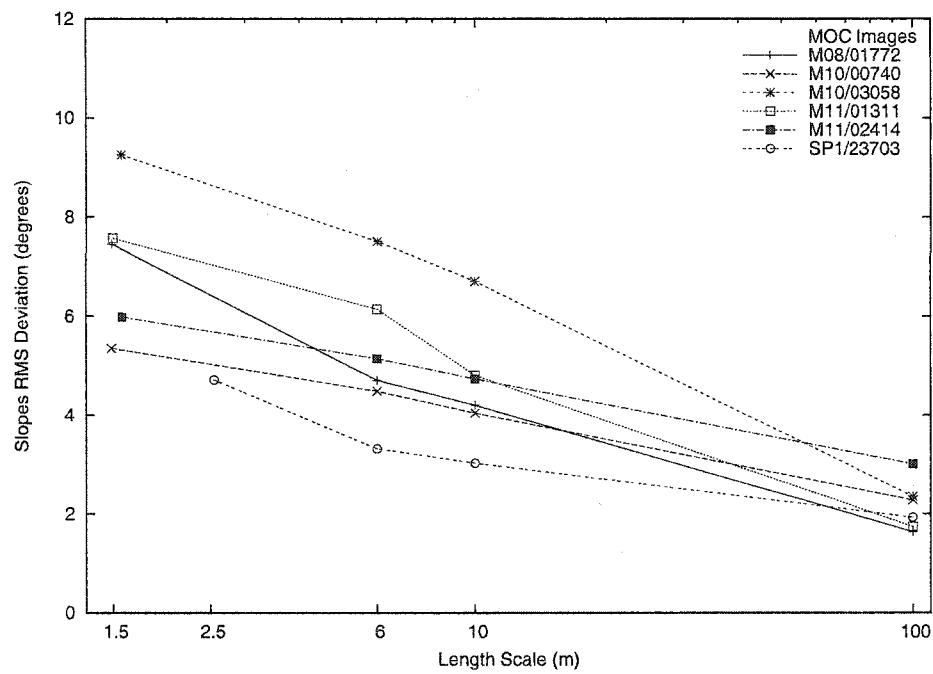


Figure 2.9: Pathfinder Landing Site RMS Roughness

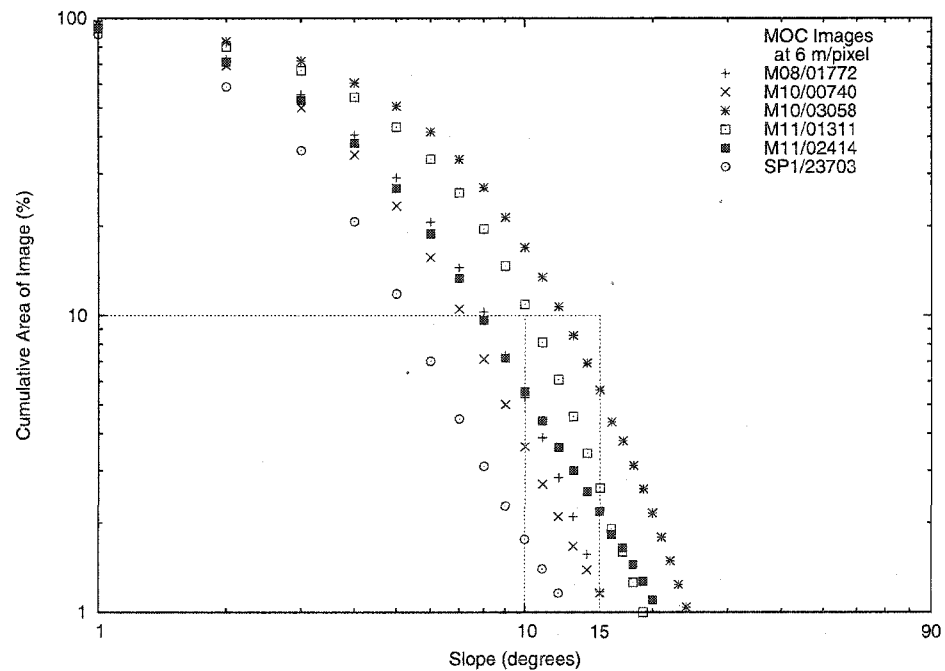


Figure 2.10: Pathfinder Landing Site Slope Distribution

regions to be smooth at the meter scale. This is reassuring due to the meter-scale smoothness observed by the landers themselves. For these three locales on the martian surface for which we have ground truth, our technique appeared to report accurate upper limits to the slopes observed by the landers.

2.5 Application to MER 2003 Landing Sites

The point photoclinometry technique that we used in this study is not yielding exact slope measurements, due to the albedo variations and coarse haze estimates that we employed. However, by conservatively measuring the images and using the automatic maximum haze estimation we were able to yield a solid upper bound to the down-Sun slopes in the images measured. The slope values reported by our photoclinometry measurement technique should not be considered in isolation, we strongly suggest that our slope measurements be used as an additional piece of information on which to judge the safety of any given landing ellipse, and that they not be considered without also looking at the images that were measured to create them.

2.5.1 Athabasca Valles

We found twenty-four images that overlapped the potential landing area in Athabasca Valles, listed in Table 2.7. The slope statistics for Athabasca can be found in Figures 2.11 and 2.12.

The Athabasca Valles site was eliminated from consideration for MER 2003 due to high radar backscatter values in the area, but continues to be an interesting area for study and a possible destination for future landers (e.g. Burr et al., 2002b).

The mosaic of RMS slope images in Figure 2.13 shows how these RMS slope images are useful indicators of morphologic change on the surface. The images in the western portion of the proposed landing ellipse show rather smooth terrain, with groupings of fresh looking craters adding some roughness. A small dune field is picked out in the RMS slope image of M04/02002. The high-slope area in the

Athabasca Valles Landing Site Images

MOC Image	Resolution (m/pixel)	Incidence Angle ($^{\circ}$)	Portion Measured
M02/00581	5.875	37.75	central
M04/02002	5.867	42.10	all
M07/00614	5.873	43.26	southern
M07/01888	5.874	43.80	central
M09/00662	2.934	45.52	all
M09/02518	5.864	45.30	northern
M11/00331	2.926	41.81	all
M12/01114	5.864	35.97	all
M12/02516	6.074	25.35	all
M18/01080	5.872	26.21	southern
E10/01384	3.1	43.67	southern
E10/02604	6.18	42.23	northern
E10/03841	3.09	41.56	northern
E11/00142	3.09	40.68	all
E11/02913	3.1	38.37	all
E11/03799	3.1	37.24	all
E12/00071	3.1	36.04	all
E12/01728	1.75	35.01	all
E12/01946	4.64	33.5	all
E12/02746	4.63	31.53	northern
E12/02967	4.16	29.53	all
E13/00030	3.09	30.73	all
E13/00697	3.09	29.5	all
E13/01475	1.65	26.73	all
E13/02142	4.65	27.15	all

Table 2.7: This table contains the MOC Image Numbers of all the images in the Athabasca Valles Landing site area for this study.

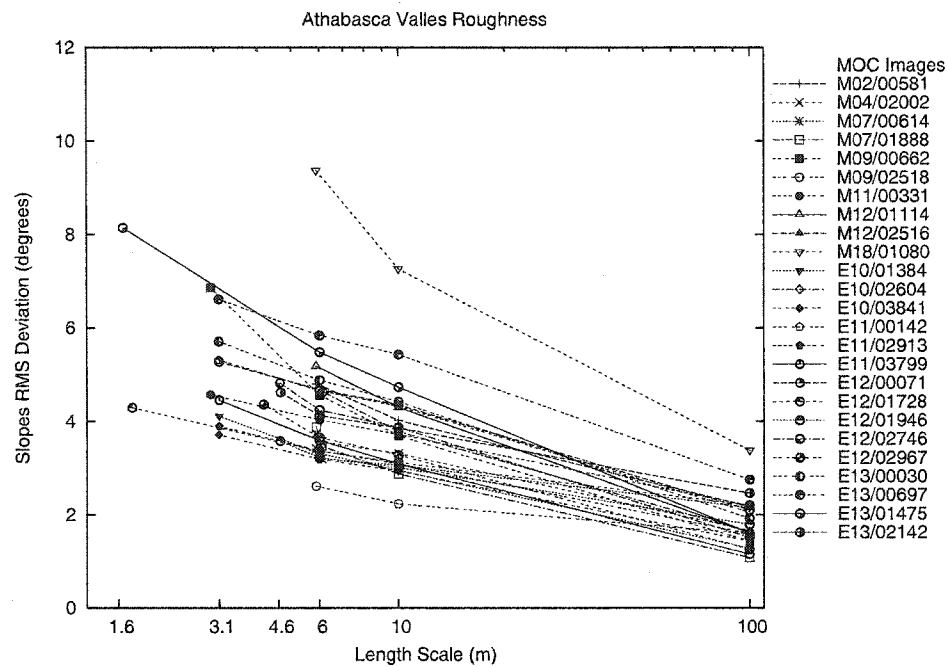


Figure 2.11: Athabasca Valles Site RMS Roughness

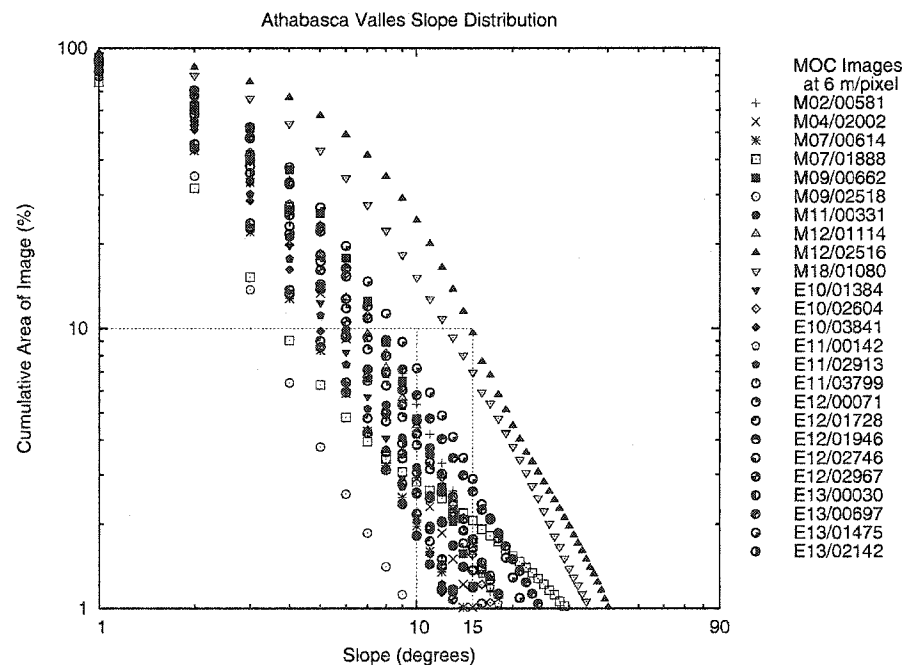


Figure 2.12: Athabasca Valles Site Slope Distribution

Elysium Planitia Landing Site Images

MOC Image	Resolution (m/pixel)	Incidence Angle (°)	Portion Measured
E17/01505	3.10	25.58	all
E18/00019	3.10	26.23	all
E18/00429	3.10	26.90	all
E18/00898	3.10	27.60	all
E18/01327	3.10	28.31	all
E18/01455	4.17	24.77	all

Table 2.8: This table contains the MOC Image Numbers of all the images in the Elysium Planitia Landing site area for this study.

southern portion of E13/00030 is a high-standing ridge. There is some rough terrain in the southern portions of E11/03799 and E13/01475 that is highlighted by the RMS slope images. The interior slope of the crater at the southern end of E12/01728 (Figure 2.14a) is easily seen in the RMS slope images as is the steeper slope of its eroded northern flank. The RMS slope images in the eastern portion of the ellipse (e.g. Figures 2.14b and 2.14c) display steep slopes associated with the sides of streamlined mesas, and scour marks on the floors of the channels (Burr et al., 2002b). Additionally, some of the roughness images clearly delineate the smoother channel floor from the slightly rougher banks (e.g. E12/02746 and E10/02604).

2.5.2 Elysium Planitia

The landing site in Elysium Planitia was added into the site selection process after the Athabasca Valles and Melas Chasma sites were eliminated, and so MOC coverage of this area was limited at the time of our study. The images we measured are listed in Table 2.8, and the measurements are in Figures 2.15 and 2.16.

The RMS slope images in this area (Figure 2.17a) mostly show the presence of craters. The roughness in the RMS slope image of E18/01327 (Figure 2.18a) is due to low albedo and a number of small, fresh craters. Other large craters are easy to observe in the various RMS slope images. A ridge running south from a large

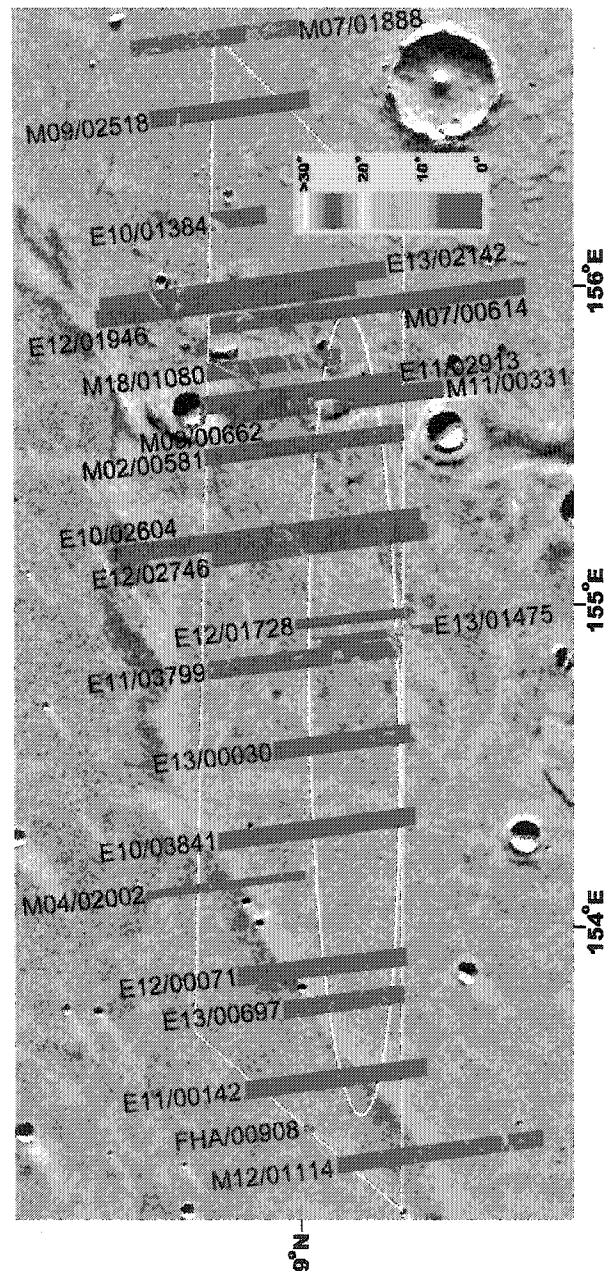


Figure 2.13: Athabasca Valles RMS Slope Image Mosaic. The colorized RMS slope images of the various portions of MOC images which were measured in this area are mosaicked onto a basemap of Viking Orbiter images (MDIM 2). The solid ellipse is the locations of the landing ellipse at the opening of the launch window, and the dotted ellipse is the location at the close of the launch window. In the case of Athabasca Valles, more than just the terrain of one possible landing ellipse was requested for more complete MOC coverage, and the rhombus indicates that high-coverage area.

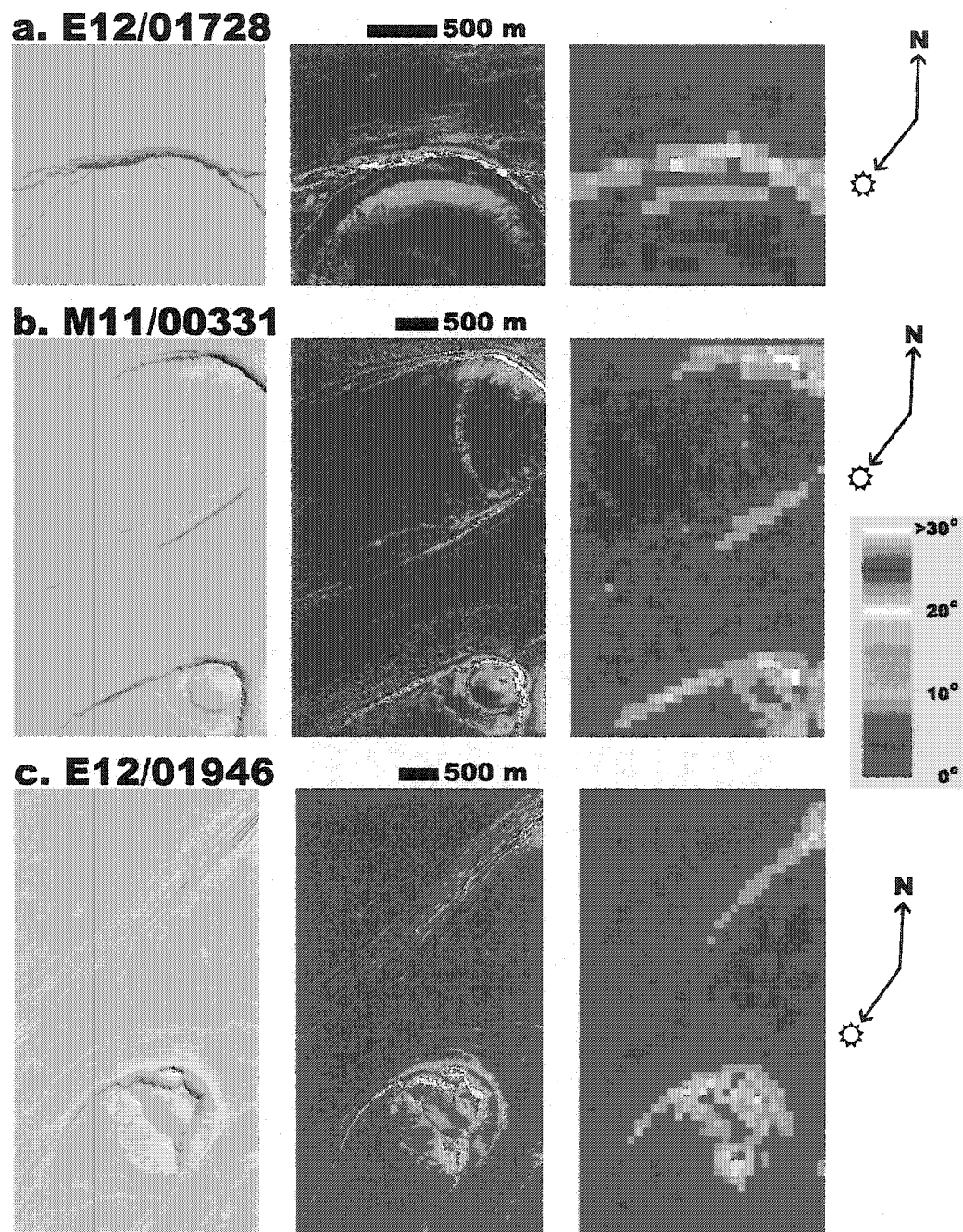


Figure 2.14: Each of these three figures contains (from left to right) a portion of a cleaned and calibrated MOC image in the Athabasca Valles study area, a slope image at the original resolution of the MOC image, and an RMS slope image. The large pixels in the RMS slope image are 100 m across. *a.* Portion of E12/01728. This image shows a crater whose northern flank has been eroded. *b.* Portion of M11/00331. This image shows some of the fluvially modified mesas in Athabasca Valles. *c.* Portion of E12/01946. This image also shows some of the fluvially modified forms in Athabasca Valles.

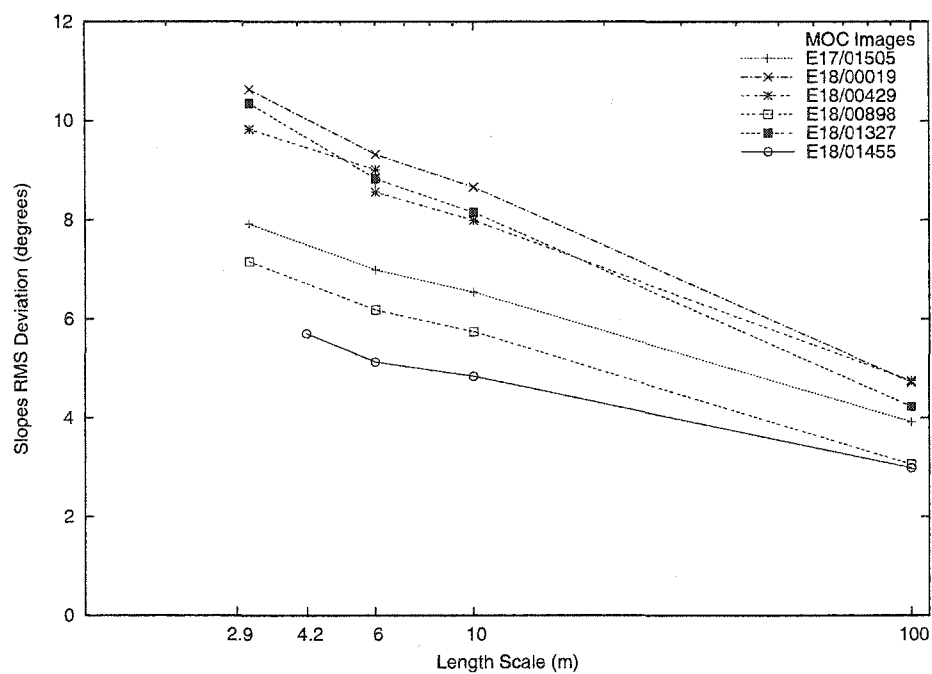


Figure 2.15: Elysium Planitia Site RMS Roughness

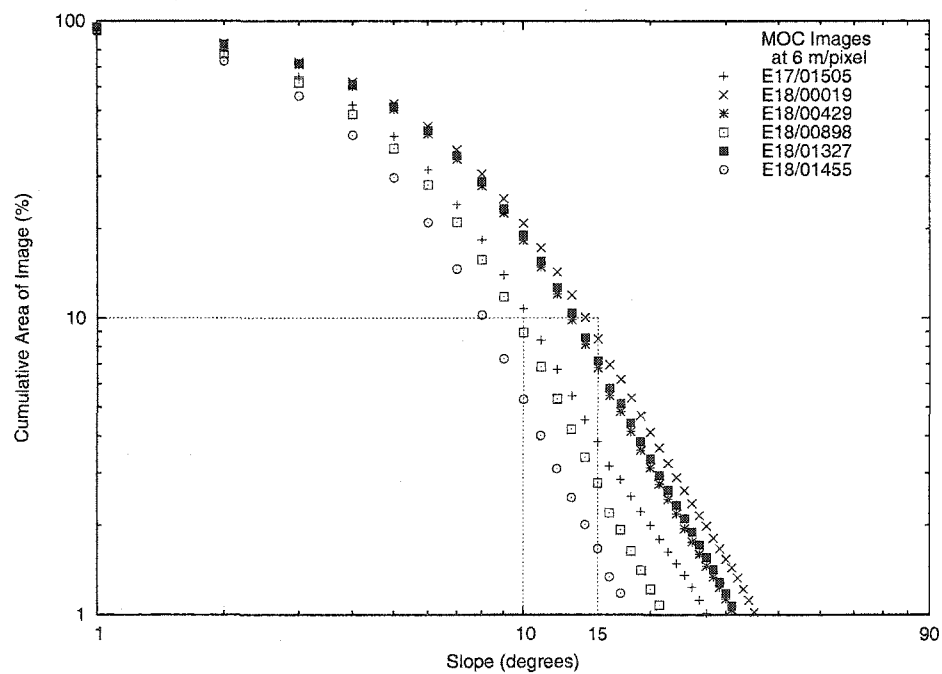


Figure 2.16: Elysium Planitia Site Slope Distribution

Eos Chasma Landing Site Images

MOC Image	Resolution (m/pixel)	Incidence Angle (°)	Portion Measured
M02/02072	5.676	45.96	northern
M03/00926	5.681	44.51	southern
M03/02292	5.68	43.97	northern
M08/01913	5.682	37.77	southern
M09/00925	2.841	35.19	southern
E01/00315	2.84	51.03	all
E01/00781	2.85	51.05	all
E02/00633	2.87	49.55	central
E02/02855	4.3	48.25	central
E03/00738	3.06	49.0	all
E03/01452	2.86	46.95	southern
E04/00506	2.85	45.53	all
E04/01275	3.3	47.04	northern
E04/02155	2.87	44.28	southern
E05/01125	2.87	43.13	all
E05/03243	2.85	41.99	southern
E06/00009	3.67	38.78	northern

Table 2.9: This table contains the MOC Image Numbers of all the images in the Eos Chasma Landing site area for this study.

crater in E18/00429 (Figure 2.18b) is highlighted by its steeper slopes. A crater rim and its rays are displayed in the RMS slope image of E18/00019 (Figure 2.18c), and the slope information also displays a low ridge running east-west along the northern border of the ellipse.

2.5.3 Eos Chasma

There were seventeen images that had sections within the Eos Chasma landing ellipse (see Table 2.9). Since most of the images contain terrain that climbs up the chasma walls to the north or south, we did not measure the ends of most of the images. The statistical information for the Eos Chasma images is in Figures 2.19 and 2.20.

Eos Chasma was eliminated from the site selection process due to high slope-

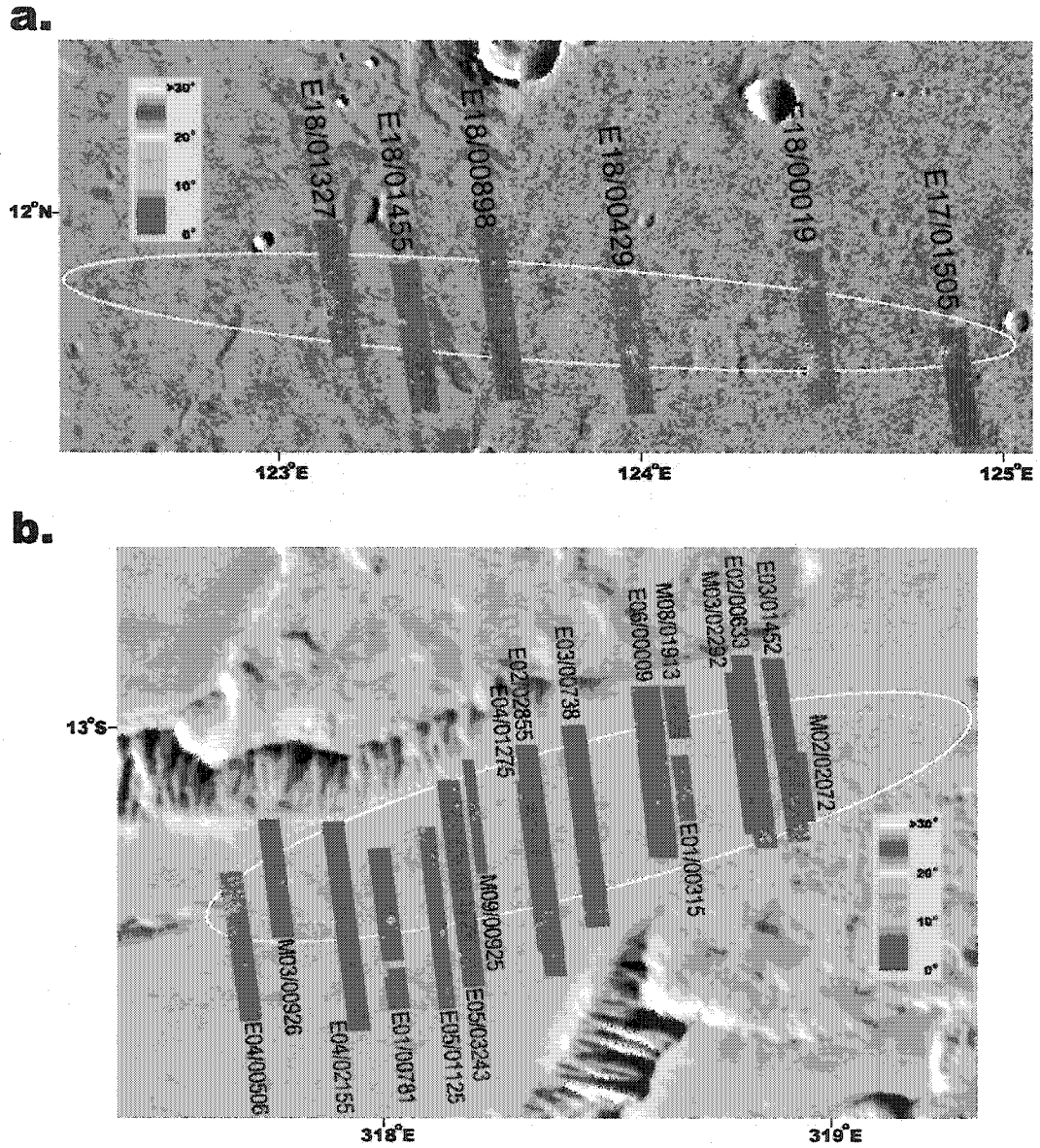


Figure 2.17: Elysium Planitia and Eos Chasma RMS Slope Image Mosaic. *a.* Elysium Planitia RMS Slope Image Mosaic. *b.* Eos Chasma RMS Slope Image Mosaic. The solid ellipse is the location of the landing ellipse at the opening of the launch window, and the dotted ellipse is the location at the close of the launch window. In both of these images the colorized RMS slope images of the various MOC images in this area are mosaicked onto a basemap of Viking Orbiter images (MDIM 2).

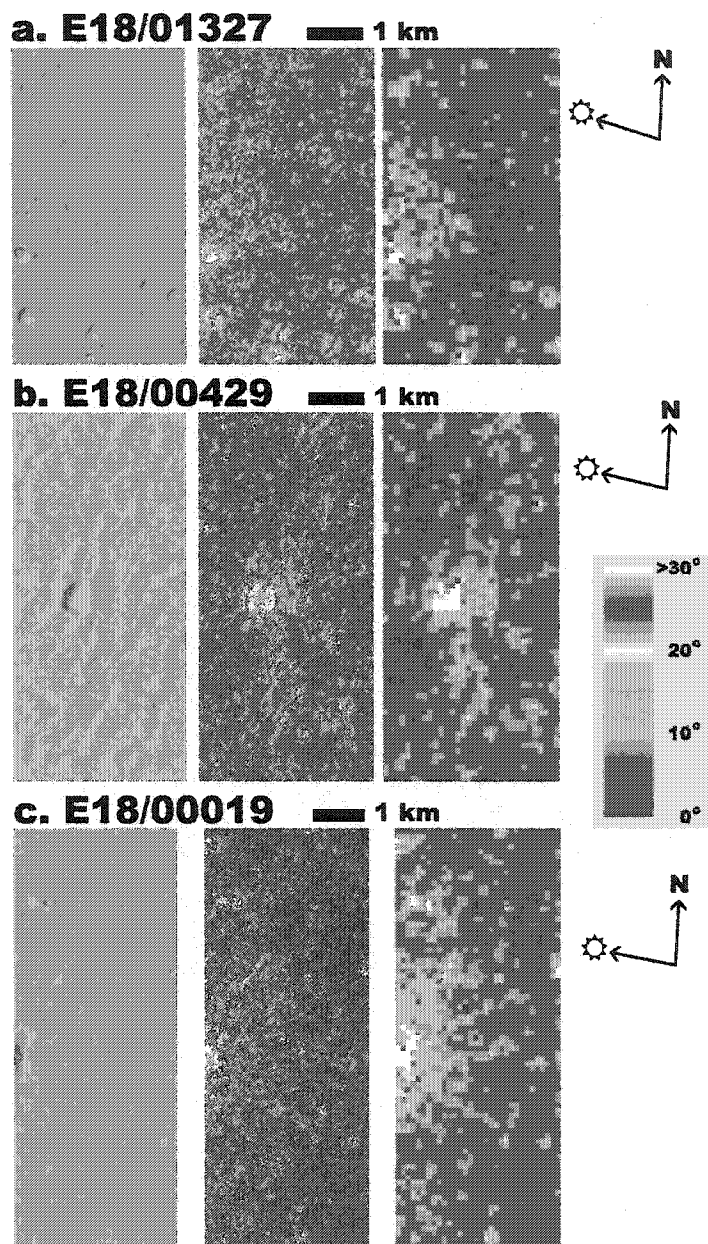


Figure 2.18: Each of these three figures contains (from left to right) a portion of a cleaned and calibrated MOC image in the Elysium Planitia study area, a slope image at the original resolution of the MOC image, and an RMS slope image. The large pixels in the RMS slope image are 100 m across. *a.* Portion of E18/01327. This image shows small fresh craters are easily seen in the slope images. *b.* Portion of E18/00429. This image displays the slopes on a ridge running south of a crater. *c.* Portion of E18/00019. The easternmost rim of a crater and the steeper slopes on its ejecta are picked out in the slope images here.

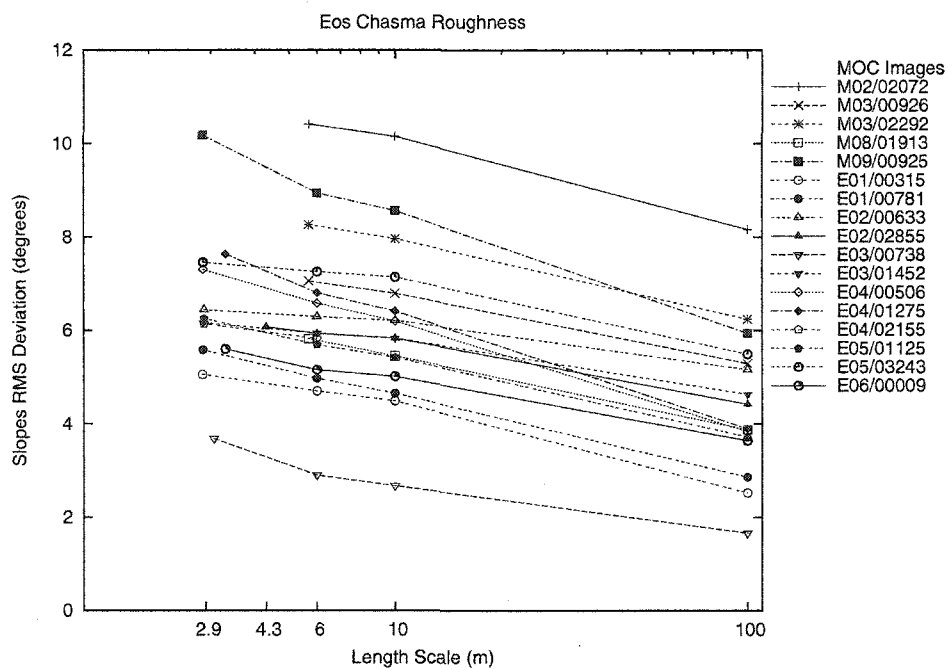


Figure 2.19: Eos Chasma Site RMS Roughness

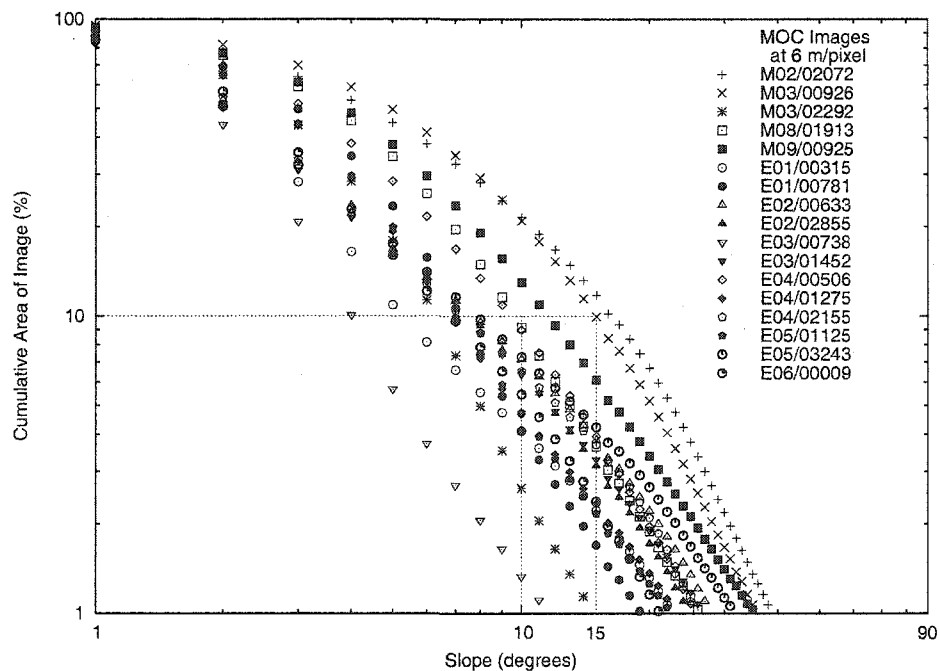


Figure 2.20: Eos Chasma Site Slope Distribution

generated winds that sweep up and down the walls of the Valles Marineris, making this area quite dangerous for the MER 2003 afternoon landing.

The mosaic of RMS slope images in Figure 2.17b shows how these RMS slope images are useful indicators of morphologic change. The slopes on the tail of the streamlined landform to the west of the ellipse can be seen in the RMS slope images of E04/00506 (Figure 2.21a) and M03/00926. Additionally, some of the hummocky terrain to the southeast of the ellipse can be seen in the RMS slope images of E03/01452 (Figure 2.21b), M02/02072, and E02/00633 (Figure 2.21c). Aside from crater forms within the proposed ellipse, there do not seem to be other distinctive morphologies within the ellipse.

2.5.4 Gusev Crater

The images in Table 2.10 are in or near the Gusev Crater landing ellipse (Cabrol et al., 2003). The floor of Gusev Crater presents some problems for our photo-clinometry technique in the form of large dark-toned areas made up of dust-devil tracks and wind streaks (Milam et al., 2003). The southern half of M07/00813 was not measured, because of these albedo problems. However, other images in this area were not as severely affected. Figures 2.22 and 2.23 show the slope statistics for these images in Gusev Crater.

The slope signature of large craters is evident in the RMS slope images of E10/02768, M03/01042 (Figure 2.24a), and M03/02330. The southern patch of the Etched unit (ET) identified by Milam et al. (2003) in the center of the ellipse is easily seen in the RMS slope image of M11/00476 (Figure 2.24b). Additionally, the rougher slopes of the larger ET unit can be seen in the RMS slope images of E10/01562 and E05/00471. The RMS slope image of E03/00012 (Figure 2.24c) distinctly shows a triangular patch of material with steeper slopes that corresponds to an island of Basin Floor unit 1 (AHbm1) identified by Kuzmin et al. (2000).

In the context of the RMS slope image mosaic (Figure 2.25), the rim of the Thira crater (the large crater the the eastern end of the ellipse is in) and the rougher terrain outside of it can be seen in the RMS slope images on the eastern end of the ellipse.

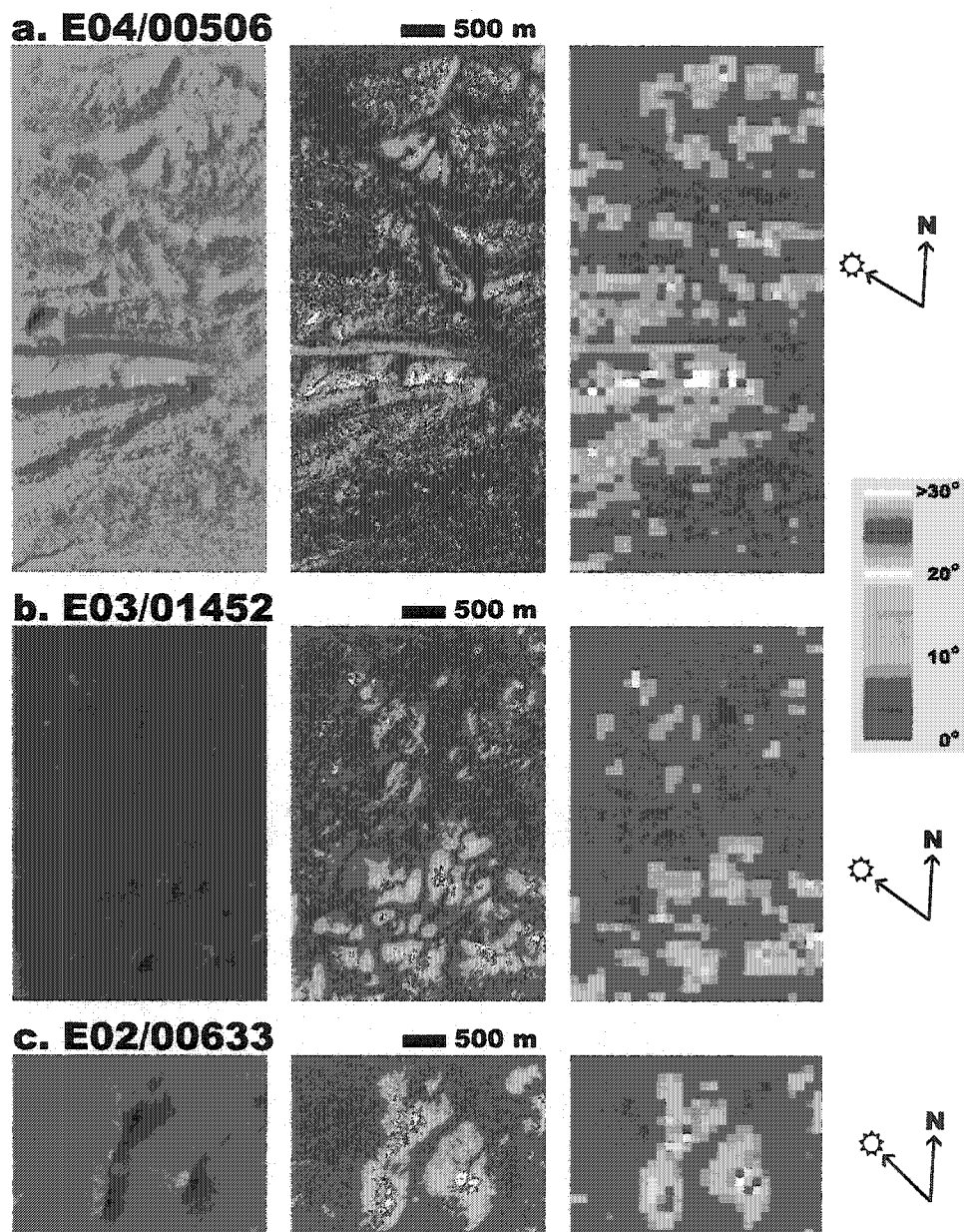


Figure 2.21: Each of these three figures contains (from left to right) a portion of a cleaned and calibrated MOC image in the Eos Chasma study area, a slope image at the original resolution of the MOC image, and an RMS slope image. The large pixels in the RMS slope image are 100 m across. *a.* Portion of E04/00506. This image shows the streamlined landform on the western edge of the ellipse. *b.* Portion of E03/01452. Hummocky terrain in the southeast portion of the ellipse can be seen. *c.* Portion of E02/00633. More of the hummocky terrain in the southeast portion of the ellipse can be seen in this image portion.

Gusev Crater Landing Site Images

MOC Image	Resolution (m/pixel)	Incidence Angle ($^{\circ}$)	Portion Measured
M02/02129	5.674	46.63	all
M03/02330	2.839	44.43	southern
M07/00813	4.259	40.38	northern
M08/01958	1.419	37.48	northern
M10/00855	5.683	30.55	northern
M11/00476	4.246	26.43	northern except NW corner
E02/00665	2.87	50.72	northern
E02/01453	3.32	48.33	northern
E03/00012	2.86	49.31	northern
E03/01511	2.86	47.97	central
E05/00471	2.96	43.25	northern
E05/01350	3.36	41.05	all
E05/03287	2.85	42.3	northern
E10/01562	2.98	28.42	all
E10/02768	2.98	27.40	all

Table 2.10: This table contains the MOC Image Numbers of all the images in the Gusev Crater Landing site area for this study.

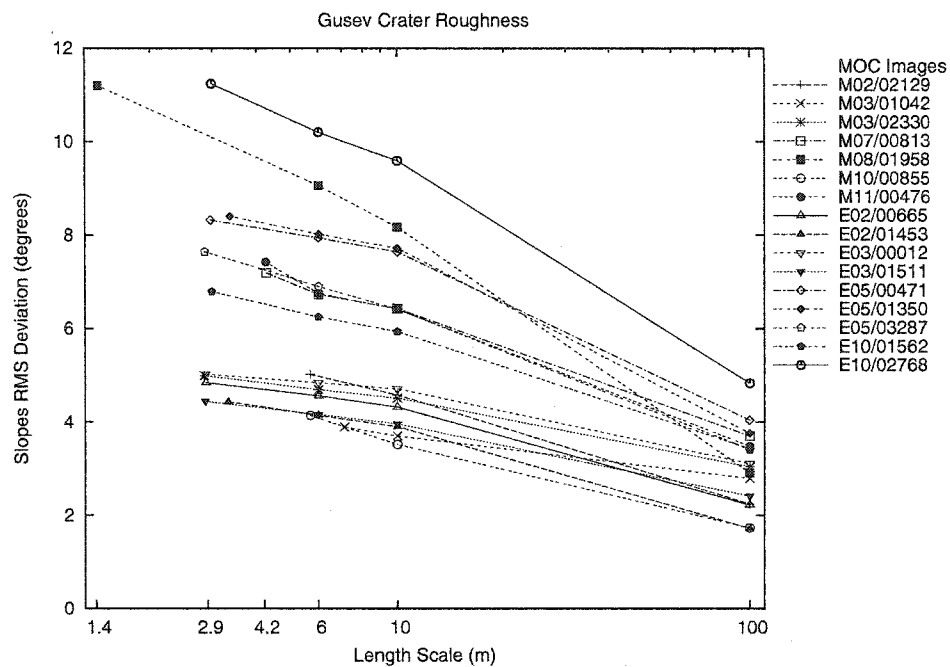


Figure 2.22: Gusev Crater Site RMS Roughness

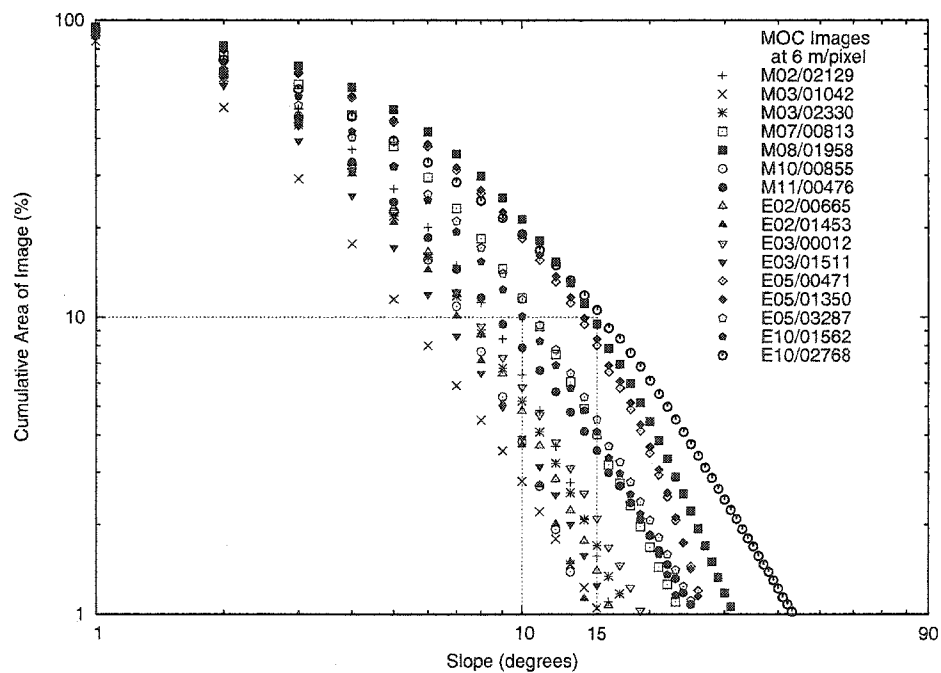


Figure 2.23: Gusev Crater Site Slope Distribution

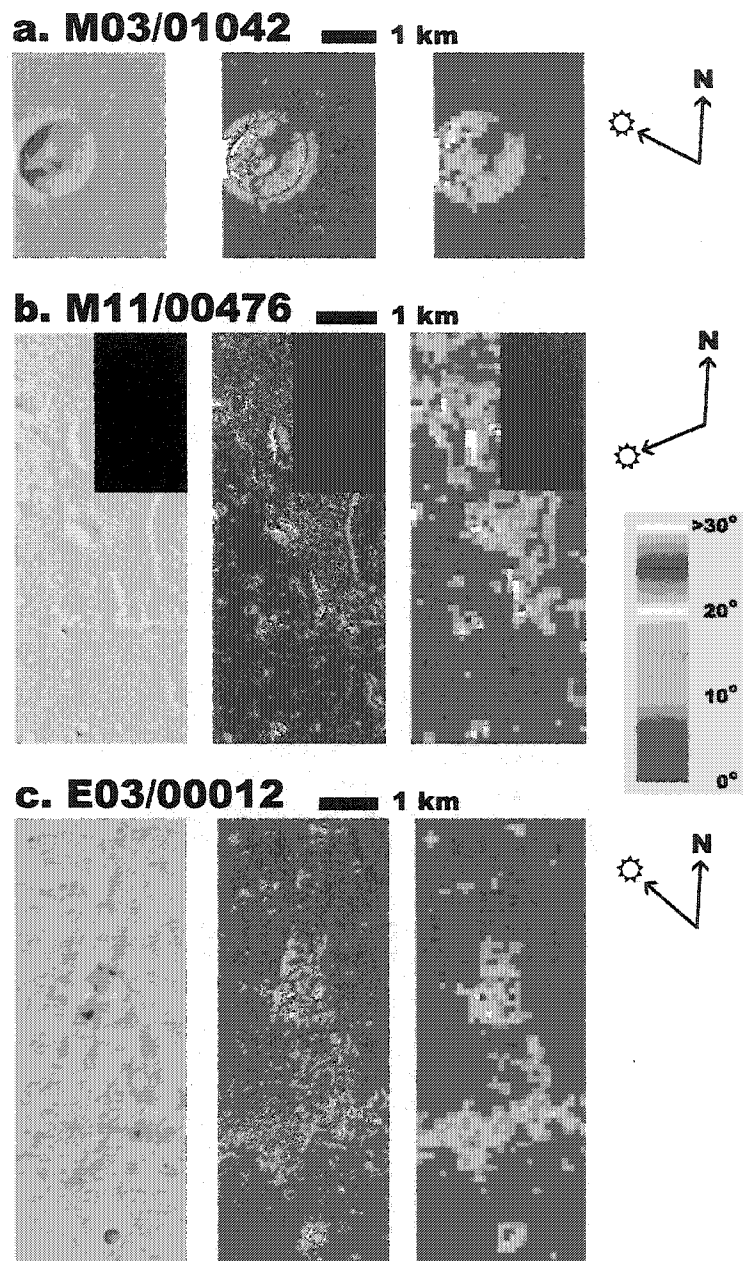


Figure 2.24: Each of these three figures contains (from left to right) a portion of a cleaned and calibrated MOC image in the Gusev Crater study area, a slope image at the original resolution of the MOC image, and an RMS slope image. The large pixels in the RMS slope image are 100 m across. *a.* Portion of M03/01042. This image shows the slopes on a large crater in the Gusev ellipse. *b.* Portion of M11/00476. This image shows the rougher slopes of an etched unit. *c.* Portion of E03/00012. This image shows the slopes of a triangular hill identified as a basin floor unit.

Additionally, many of the different units identified in the hazard map of Golombek et al. (2003) for Gusev crater can also be identified in this mosaic by changes in roughness for the different units.

2.5.5 Isidis Planitia

There were twenty-seven images (Table 2.11) in the Isidis Planitia landing ellipse (Crumpler and Tanaka, 2003). This site also had very low roughness, as the maximum slope measurements in Figures 2.26 and 2.27 show.

The distribution of slopes within the Isidis ellipse is shown in Figure 2.28. The RMS slope images here are mostly detecting large craters. There are a number of dark-floored craters in this region. Because of the low-albedo material on their floors, our photoclinometry technique indicates that their floors are very steep, making these craters very obvious on the RMS slope images (and potentially inflating the slope statistics). Good examples are in the southern tip of E13/00145, E18/00622, and within the ellipse on E18/00196 and E12/00438. However, the areas that have steep slopes in the mosaic are consistent with areas on the hazard maps of Golombek et al. (2003) that have fresh craters and heavily cratered terrain. The northern portions of the RMS slope images of E02/02211 (Figure 2.29a) and E04/01562 display a freckled pattern of high slopes, that correspond to some small hillocks north of the ellipse. There is a band of closely spaced craters with high-albedo dunes on their floors that show up nicely in the northern portions of the RMS slope images of E11/00717 and E05/00486. Terrain similar to this in appearance and slope characteristics appears in the northern tips of E05/02100 and E02/00049 (Figure 2.29b). The RMS slope image of E05/02100 (Figure 2.29c) nicely displays a shallow channel that runs north-south and bisects the southern portion of that image within the ellipse.

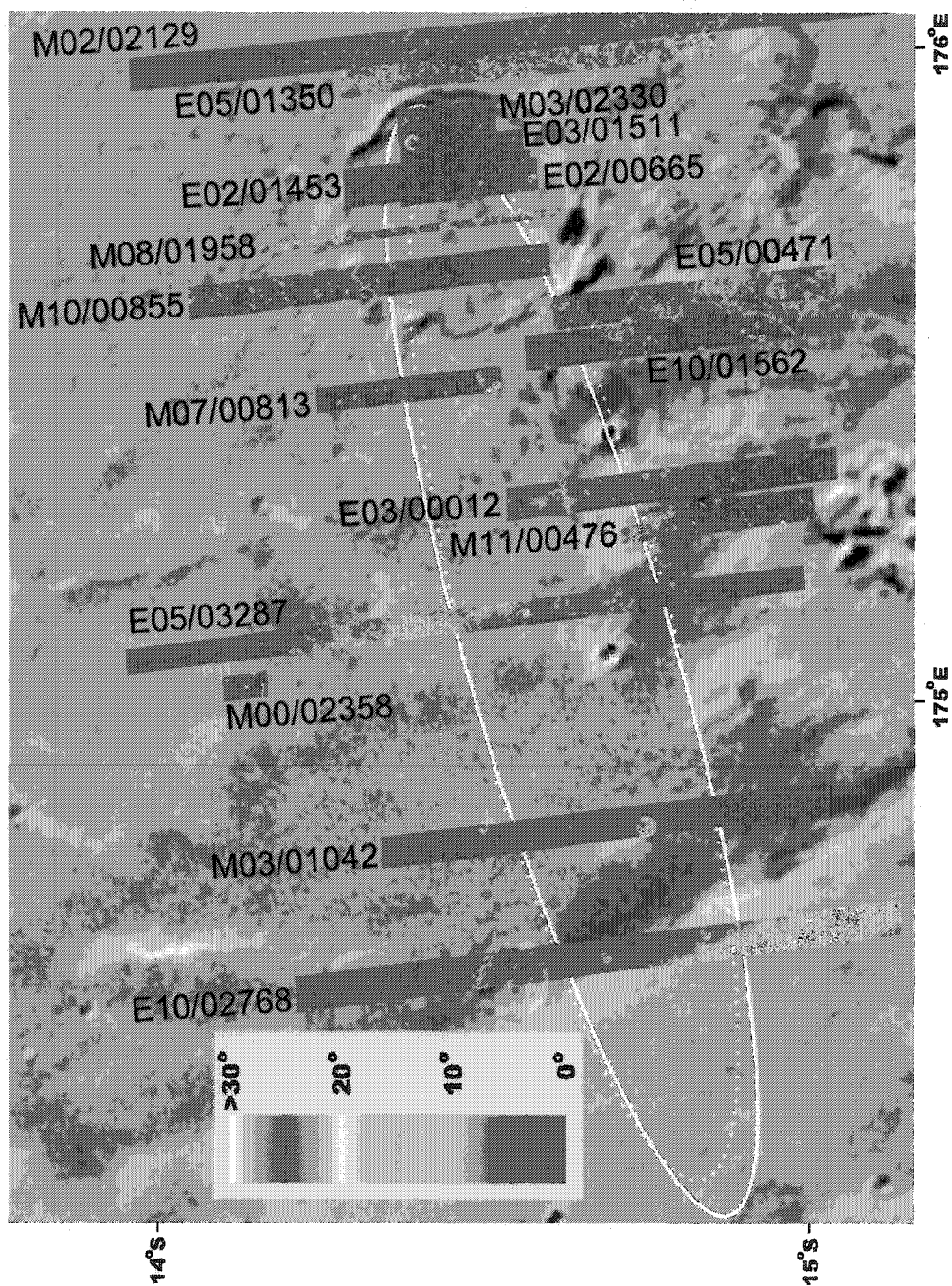


Figure 2.25: Gusev Crater RMS Slope Image Mosaic. The colorized RMS slope images of the various MOC images in this area are mosaicked onto a basemap of Viking Orbiter images (MDIM 2). The solid ellipse is the location of the landing ellipse at the opening of the launch window, and the dotted ellipse is the location at the close of the launch window.

Isidis Planitia Landing Site Images

MOC Image	Resolution (m/pixel)	Incidence Angle ($^{\circ}$)	Portion Measured
M10/01982	7.244	39.92	central
M21/00723	2.905	37.32	northern
E02/00049	5.85	39.13	all
E02/00681	2.94	38.86	southern
E02/02211	2.936	38.34	all
E03/00038	2.93	38.63	southern
E03/01529	2.92	38.69	southern
E04/01562	2.925	39.27	all
E05/00486	2.928	39.83	all
E05/02100	2.914	40.51	all
E09/00789	6.117	41.91	all
E11/00717	3.051	36.57	all
E11/02075	3.055	35.48	northern
E12/00438	3.059	31.75	all
E12/01266	3.055	30.53	all
E12/02073	1.482	29.89	all
E13/00145	3.243	28.38	all
E13/00788	3.317	27.45	all
E13/01415	1.959	27.47	all
E13/02262	3.056	23.58	all
E14/02034	1.525	21.09	all
E16/01402	3.046	23.30	all
E16/01980	3.052	24.12	all
E17/01666	3.047	28.04	all
E18/00196	3.05	28.98	all
E18/00622	3.053	29.94	all
E18/01521	1.463	32.11	all

Table 2.11: This table contains the MOC Image Numbers of all the images in the Isidis Planitia Landing site area for this study.

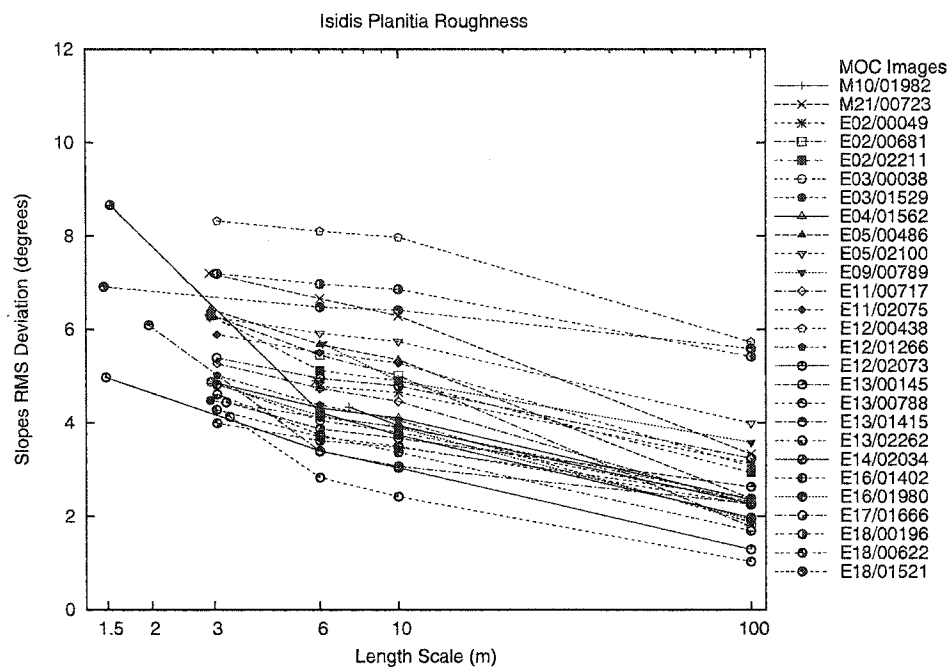


Figure 2.26: Isidis Planitia Site RMS Roughness

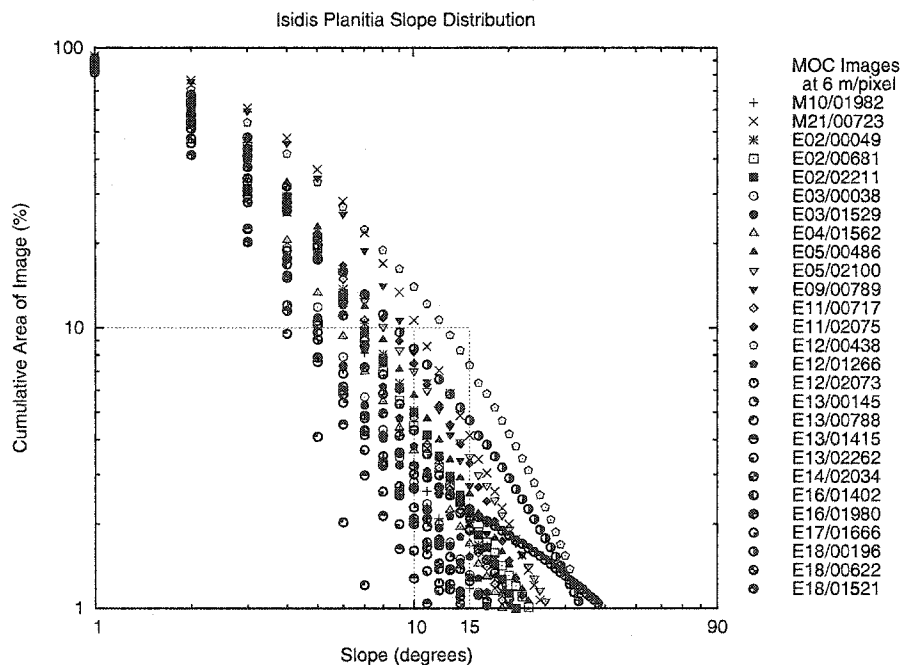


Figure 2.27: Isidis Planitia Site Slope Distribution

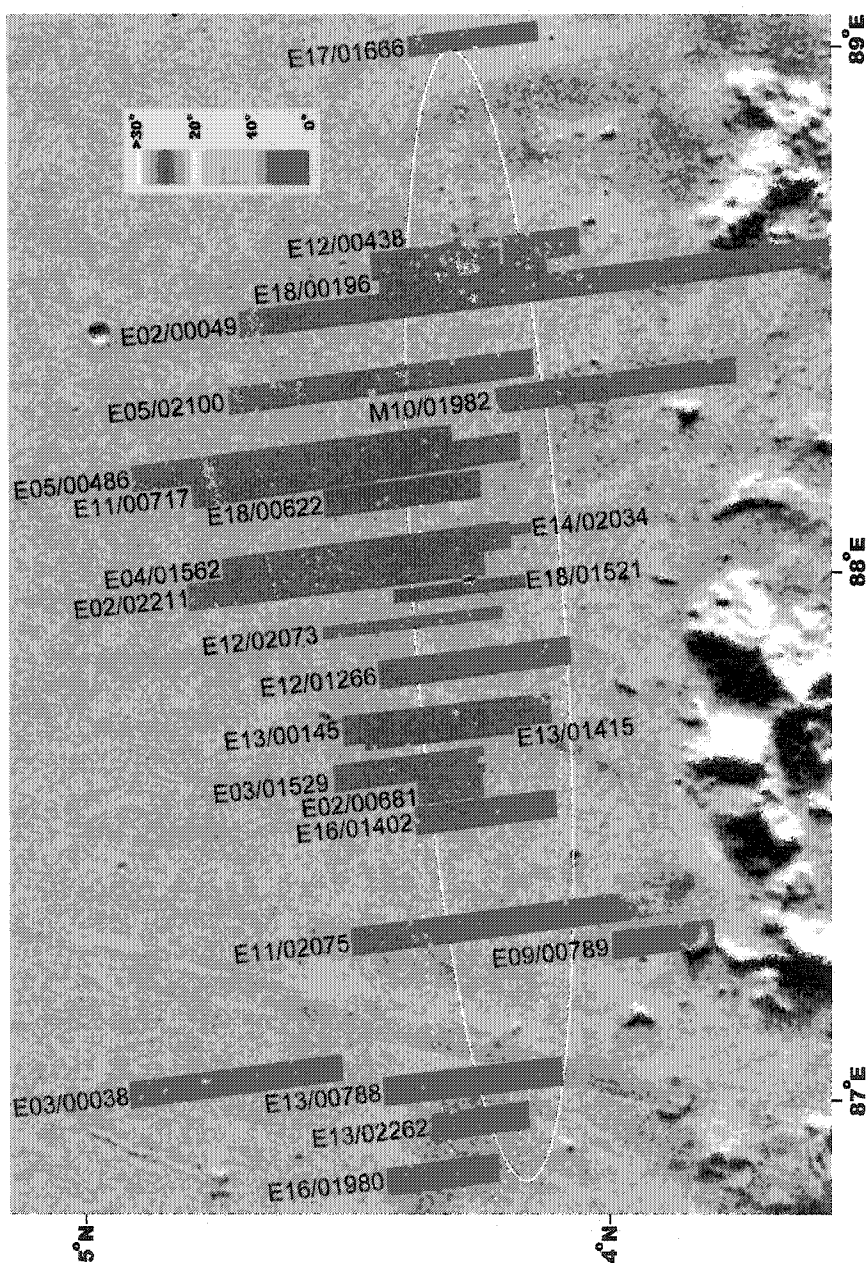


Figure 2.28: Isidis Planitia RMS Slope Image Mosaic. The colorized RMS slope images of the various MOC images in this area are mosaicked onto a basemap of Viking Orbiter images (MDIM 2). The solid ellipse is the location of the landing ellipse at the opening of the launch window, and the dotted ellipse is the location at the close of the launch window.

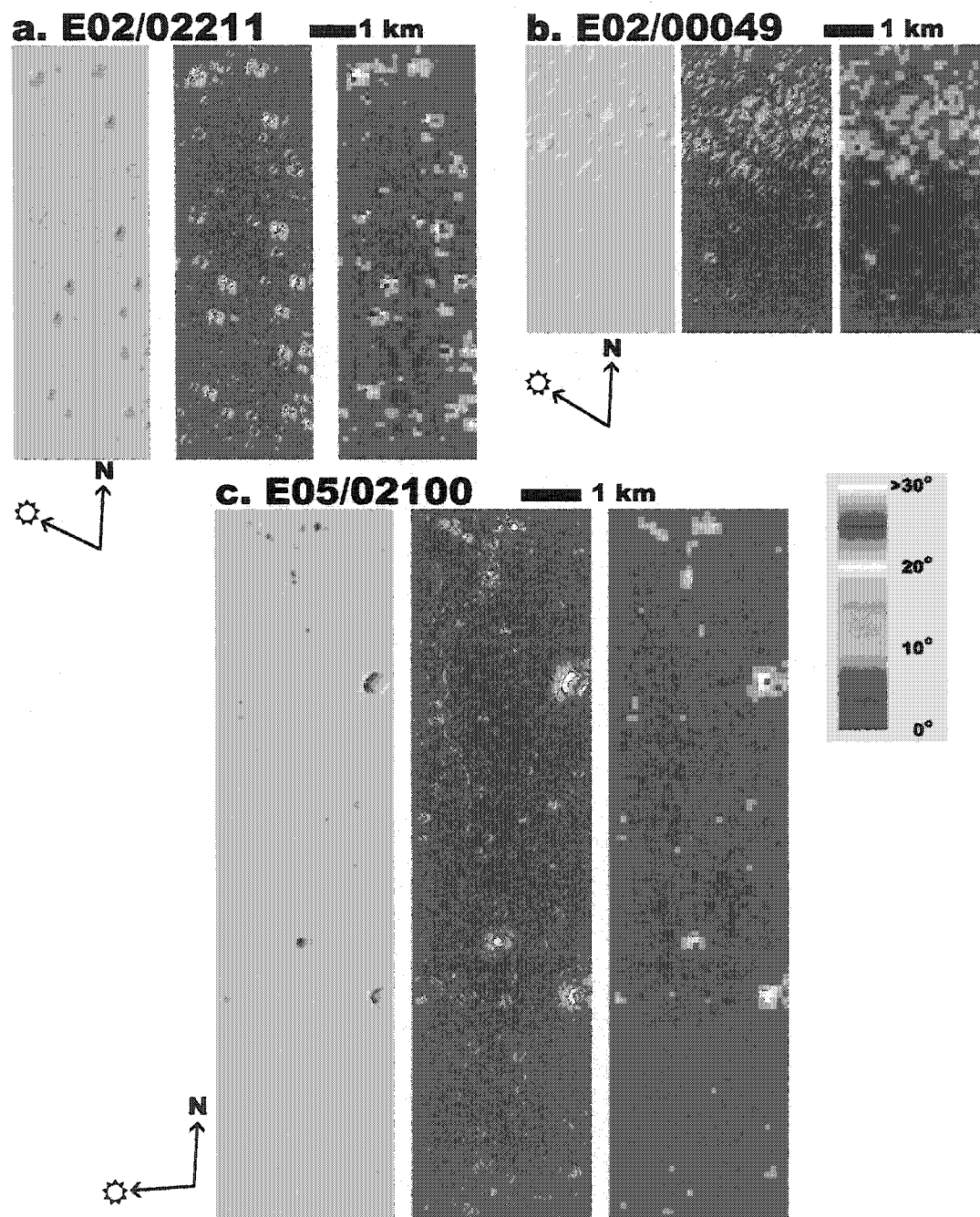


Figure 2.29: Each of these three figures contains (from left to right) a portion of a cleaned and calibrated MOC image in the Isidis Planitia study area, a slope image at the original resolution of the MOC image, and an RMS slope image. The large pixels in the RMS slope image are 100 m across. *a.* Portion of E02/02211. Outside of the ellipse the slopes of small, scattered hillocks can be seen in the slope images. *b.* Portion of E02/00049. This portion of the image outside of the ellipse shows a concentration of small, closely spaced craters. *c.* Portion of E05/02100. A small channel that runs north-south within the ellipse can be seen in the slope images.

2.5.6 Melas Chasma

The MOC images of the Melas Chasma landing site (Weitz et al., 2003) had too many albedo variations to make application of our photoclinometry technique practical. The images showed areas of high contrast albedo variation that did not appear slope-related. There were light-toned areas that probably are rough, but they effectively saturated the technique (reported slopes were around 90°), making accurate measurement impossible. There were albedo variations which were 0.5 to 1 km across that may or may not be topographic, some appeared to be mesas. There were also areas that seemed to have dark dust or sand that has filled in the lows of what appear to be indurated dunes or grooves. This area is of geologic interest, but we felt it constituted terrain that is dangerous to the MER landing system. Other researchers felt the same way, and the Melas Chasma site was eliminated for MER 2003, but remains an attractive target for future study.

2.5.7 Meridiani Planum

The ellipse in Meridiani Planum is situated such that it sits within the area identified as having Hematite spectral characteristics (Christensen et al., 2000). We measured thirteen MOC images that overlap the ellipse in Meridiani Planum (Table 2.12). The MOC images of this area show that it is dominated by two kinds of albedo variations. One is what appears to be a rocky or indurated surface that has been cleaned or scoured of dust. This leaves a light-toned surface of high contrast that is rough, but probably not as rough as our algorithm reports. The other albedo pattern is that of buried or exhumed craters (Arvidson et al., 2003).

Despite the complication of these persistent albedo variations, the RMS slope distributions and cumulative area measurements in Figures 2.30 and 2.31 show that this area is relatively smooth. When the albedo variations are considered, this area is probably smoother than these measurements suggest (as discussed above in §2.4.2).

In looking at the mosaic of RMS slope images (Figure 2.32) for this potential landing ellipse, most of the model slopes greater than 10° are the result of high-

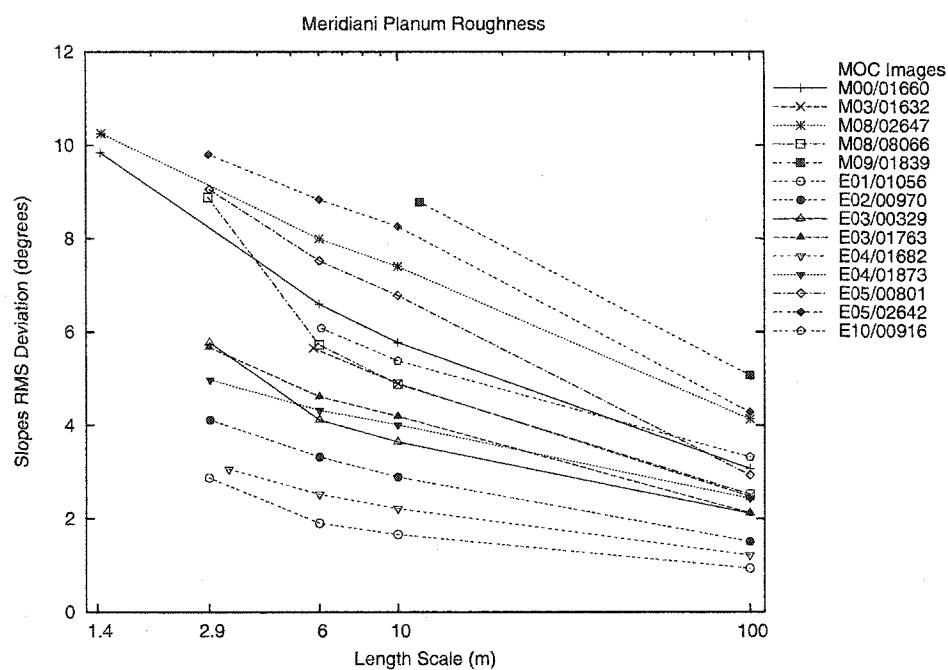


Figure 2.30: Meridiani Planum RMS Roughness

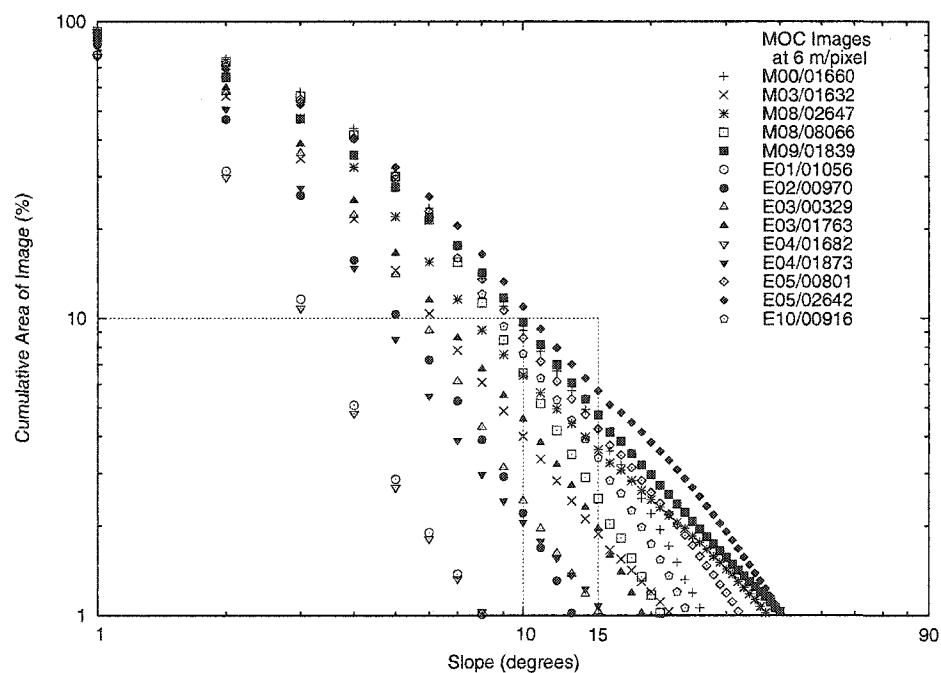


Figure 2.31: Meridiani Planum Slope Distribution

Meridiani Planum Landing Site Images

MOC Image	Resolution (m/pixel)	Incidence Angle (°)	Portion Measured
M00/01660	1.432	42.77	all
M03/01632	5.765	40.73	northern
M08/02647	1.442	40.19	all
M08/08066	2.886	39.55	all
E01/01056	2.9	43.0	northern
E02/00970	2.92	42.25	southern
E03/00329	2.91	41.56	central
E03/01763	2.9	41.15	central
E04/01682	3.3	42.74	central
E04/01873	2.92	40.55	central
E05/00801	2.91	40.50	all
E05/02642	2.90	40.51	all
E10/00916	6.08	36.90	all

Table 2.12: This table contains the MOC Image Numbers of all the images in the Meridiani Planum Landing site area for this study.

albedo rough areas and the characteristic albedo pattern of the exhumed craters. This pattern is a light-toned signature of the rim and a dark-toned patch at the center where dark material seems to have collected. Additionally, there are often light-toned, high-contrast dune fields in the centers of these craters. An example of this typical pattern can be found in the E05/00801 image (Figure 2.33a). The images in the mosaic also highlight fresh and degraded craters identified by Golombek et al. (2003) in their Meridiani Planum hazard map.

The RMS slope image of E02/00970 (Figure 2.33b) nicely identifies the rays and flank of a fresh-looking crater. The RMS slope images of M09/01839 (Figure 2.33c) and E04/01873 show some craters that have steeper model slopes than other exhumed craters in this area. There are two in M09/01839, one just north of the ellipse and another that is within the ellipse. They have rims that appear to stand above the terrain and have some actual topography to them, indicating that they are not as deeply buried as other exhumed craters in this area. The crater in E04/01873 south of the ellipse has a rim which can be seen much more clearly than

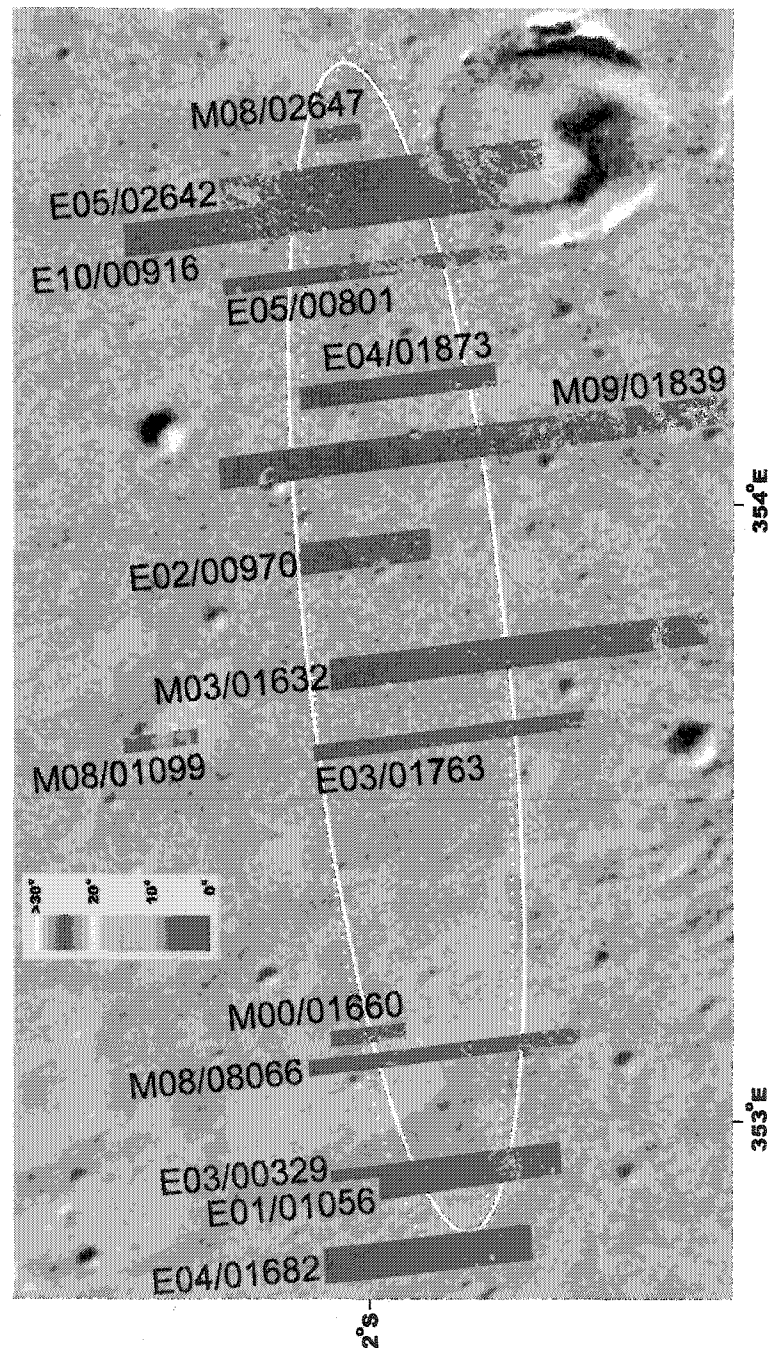


Figure 2.32: Meridiani Planum RMS Slope Image Mosaic. The colorized RMS slope images of the various MOC images in this area are mosaicked onto a basemap of Viking Orbiter images (MDIM 2). The solid ellipse is the location of the landing ellipse at the opening of the launch window, and the dotted ellipse is the location at the close of the launch window.

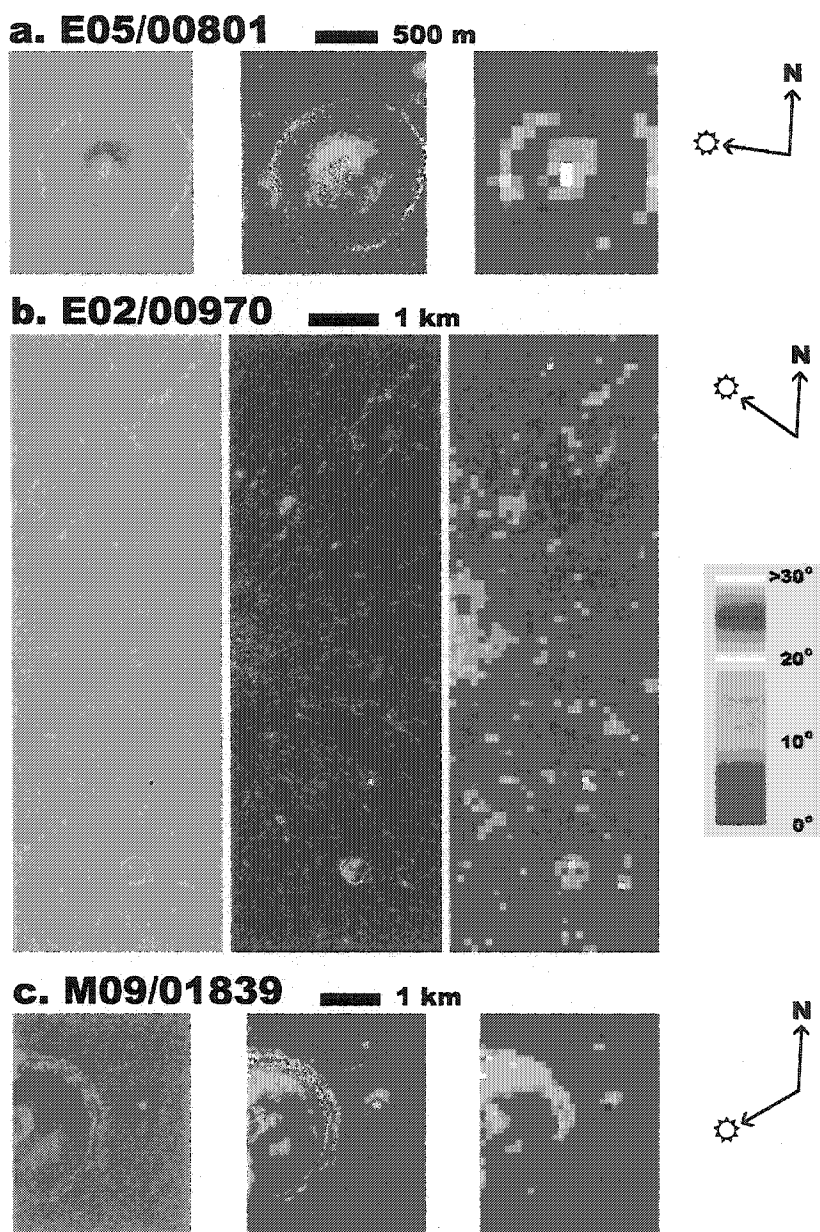


Figure 2.33: Each of these three figures contains (from left to right) a portion of a cleaned and calibrated MOC image in the Meridiani Planum study area, a slope image at the original resolution of the MOC image, and an RMS slope image. The large pixels in the RMS slope image are 100 m across. *a.* Portion of E05/00801. This image shows a typical exhumed crater in the Meridiani Planum area. *b.* Portion of E02/00970. This image picks out the rougher rays and flank of a crater. *c.* Portion of M09/01839. This image shows another exhumed crater, but this one's rim appears a little more raised than others, and the rim also appears a little differently eroded.

other buried craters in this area indicating that it may be at a different stage of burial or exhumation.

2.6 Conclusions

Our technique allowed us to measure slope characteristics at the meter scale for six of the candidate landing sites, and show that all had slope characteristics within the acceptable constraints for the MER 2003 landers. Our point photoclinometry method performed well on synthetic topography, and agreed well with results from area photoclinometry and stereogrammetry. It also passed the test of ground truth at the landing sites of Viking 1, Viking 2, and Pathfinder. By measuring several images in the same area, we were able to catch blatant outliers in the automatic estimation of haze. Due to the severe albedo variations in Melas Chasma, we were unable to obtain reliable slope measurements. However, the topography in the images near the Melas Chasma site appears to contain mesas and other obstacles that present an obvious hazard to the MER 2003 landers.

Our method in this study provides an upper bound to the down-Sun slope statistics of the images, not a true slope measurement. However, we have shown that when a more refined haze estimate for an image is available, our technique is able to provide more accurate slope statistics (e.g. when we compared area photoclinometry to our technique in §2.4.2). Additionally, our method is able to operate on and process a large number of images rather quickly, which allows us to complement and extend slope information from area photoclinometry and stereogrammetry.

The final slope criterion for site selection was based on an area-weighted failure rate of Monte Carlo entry, descent, and landing simulations based on the DEMs of Kirk et al. (2003). However, having extensive maps of roughness estimates that are internally consistent, even if they are produced differently from the DEMs, is the proper basis for assigning the area weights to the outcomes of the simulations based on the area-restricted DEMs. Additionally, these statistics can be produced to allow initial comparison of sites before the Monte Carlo results are complete.

This technique is ideal for landing site evaluation both in the early stages of site selection when there are large numbers of landing ellipses to chose from, and in the latter stages when slope information from as much terrain within a particular landing ellipse is needed and is not available from other methods.

CHAPTER 3

A profiling photoclinometry technique for determining meter-scale topography

3.1 Introduction

Topographic data for other planets is difficult to obtain, but crucial for answering various kinds of scientific questions. Orbital laser altimeters like the Mars Orbital Laser Altimeter (MOLA) (Zuber et al., 1992; Smith et al., 2001) are providing accurate global topographic data, but at a horizontal scale much coarser than imaging datasets. Shadow lengths (when present) can be measured in images, but provide a limited amount of topographic information. Stereo imaging is a way to obtain higher-resolution topographic data, but requires double the amount of imaging coverage, and produces lower resolution topographic data than the resolution of the input images.

Photoclinometry, or shape-from-shading, can derive topographic data at a resolution on the order of the image resolution from a single image. Area photoclinometry (e.g. Kirk et al., 2003) directly solves for the topography of the image scene. However, using an area photoclinometry technique is often computationally intensive, and limited to a small area.

The point photoclinometry method described in chapter 2 allows an estimate of the down-Sun slope of each pixel in an image. If a profile of such slope measurements is taken in the down-sun direction, a topographic profile can be constructed. This method of profiling photoclinometry can be used to obtain an estimate of the topography of the terrain.

In this chapter, I lay out the method for creating a profiling photoclinometry technique built from the point photoclinometry technique described in chapter 2. I also summarize a few of the ways in which I have applied this technique to various

scientific problems around the solar system.

3.2 Method

I seek to generate a topographic profile of elevation as a function of distance along the profile. This topography is derived from the surface slope of pixels in that profile and the projected size of those pixels on the surface.

Since the slopes that the point photoclinometry technique of chapter 2 returns are in the down-Sun direction, the topographic profile must also be in the down-Sun direction. This confining direction limits the application of this profiling photoclinometry technique to measuring topographic profiles in only one direction on any given image. If the landform of interest is not oriented appropriately with respect to the Sun in the scene, then measuring its topography will be difficult. Axisymmetric features, like craters or circular hills, are the most robust to this constraint. Features with a linear orientation, like transverse dunes, can be more difficult, but a correction can be made for this difference in slope azimuth.

If a set of transverse dunes has the strike of their crests perpendicular to the down-Sun direction, then a profile can be obtained, as the slopes measured will be the true slopes of the windward and slip faces of those dunes. If such a set of dunes has the strike of their crests parallel to the down-sun direction, i.e. the Sun is shining down the troughs, then a topographic profile of the dunes can not be obtained. However, a linear feature at some angle to the down-sun direction can still be measured, but a cosine correction to the slopes would need to be made to obtain the true slope of the surface, and the confidence of doing so decreases as the strike of the linear features approaches the down-sun direction.

The Sun rarely shines directly along the line or sample axis of an image, so a way must be found to gather pixels in a line in the down-sun direction. Some techniques perform a rotation of the image to put the down-sun direction along one of the axes of the image. The disadvantage with this approach is that it smears pixel brightness information in the rotated image. Despite this disadvantage, it makes

proceeding very easy, as all that needs to be done is to collect a range of pixels from a single line in the image. Instead of performing a rotation on the image, I used Bresenham's Algorithm (Bresenham, 1965; Freeman, 1980; Wolfe, 1998) to make an approximation of a straight line with square pixels in the down-Sun direction on the image.

Depending on the feature, it may be desirable to perform some averaging of brightnesses from surfaces of the same approximate surface slope in order to reduce noise. This averaging is most useful on features with a linear strike. Instead of creating a profile of one pixel in width, a profile with some averaging width can be created. The profile is established, and then Bresenham's Algorithm is used to draw lines perpendicular to that profile, at each pixel of the original profile. The width of these perpendiculars can be selected depending on the feature that is being measured. The brightnesses of all the pixels along one of those perpendiculars are averaged together to get an averaged brightness value for each pixel in the profile. These averaged brightnesses are then input into the point photoclinometry algorithm to yield a slope. I have found that most of the images that I have worked with have sufficiently high signal to noise ratios and have not needed this width averaging method, but the algorithm I developed does possess this functionality.

The point photoclinometry method returns a slope for each pixel, and to convert that into a change in elevation across that pixel, the width of the pixel in distance units must be known, as well as the down-Sun direction. Since the image is not rotated, if the Sun is not shining down an image axis, the distance across a pixel in the down-Sun direction is slightly greater than the length of a pixel side, up to $\sqrt{2}$ times that width. Although Bresenham's Algorithm forms a slightly crooked path of pixels, I make the simplifying assumption that the distance, d , across each pixel in the profile is identical, calculated as follows:

$$t = \begin{cases} \sin \alpha & : \quad \frac{\pi}{4} < \alpha < \frac{3\pi}{4} \quad \text{or} \quad \frac{5\pi}{4} < \alpha < \frac{7\pi}{4} \\ \cos \alpha & : \quad \alpha < \frac{\pi}{4} \quad \text{or} \quad \frac{3\pi}{4} < \alpha < \frac{5\pi}{4} \quad \text{or} \quad \alpha > \frac{7\pi}{4} \end{cases} \quad (3.1)$$

$$d = \frac{r}{|t|} \quad (3.2)$$

Where r is the image resolution, or length of a pixel side, and α is the solar azimuth (relative to the horizontal axis of the image), between 0 and 2π .

Once the distance across each pixel, d , is obtained from the above equation, the elevation difference, Δz , can be determined across each pixel. If a given pixel has a slope, θ , then

$$\Delta z = d \tan \theta \quad (3.3)$$

The distance across each pixel and the elevation difference across each pixel can be put together to make a topographic profile of elevation as a function of distance along that profile.

The creation of a topographic profile in this manner is a cumulative one. Unfortunately, so are the errors. The error in the elevation across the first pixel depends on the error in the distance across that first pixel, d , and the error in the slope, θ , for that pixel. However, the error in the elevation after the second pixel is dependent on the errors in d and θ for the second pixel as well as those in the first, and so on. So in addition to the difficulties of haze compensation, albedo variation, and slope azimuth which contribute to the errors of the point photoclinometry technique, there is the added contribution of this cumulative error for the profiling photoclinometry technique.

As a result, the absolute elevation difference between the beginning and end of a profile is not very reliable, and so, such photoclinometric profiles should not be terribly long. However, relative elevation differences are reasonably reliable if they are separated by only a few tens of pixel distances. This method can be made more reliable if some other source of topographic data can be used to normalize the profile (for example using MOLA shots where they intersect a profile on Mars).

A priori knowledge of the surface being measured can be useful. Features of interest often lie on flat plains. If those surfaces can be determined by other means

to be flat or assumed to be flat, and that surface can be included in the profile, it can be used to normalize the profile.

3.3 Applications

This profiling photoclinometry technique has been successfully used in a number of investigations to determine the pixel-scale topography of features on Mars and Jupiter's moon Europa. This work has been carried out in collaboration with other researchers. As a result, the sections below are not complete descriptions of research programs, but only examples of how my profiling photoclinometry technique has played a crucial role in these investigations.

3.3.1 Flood-formed Dunes in Athabasca Valles

The amount of discharge that occurred in martian outflow channels is difficult to estimate. Carling (1996a) has developed a method of estimating discharge based on the morphology and granulometry of flood-formed bedforms on the Earth. We have sought to apply this technique to transverse periodic dune-forms in Athabasca Valles (Burr et al., 2002a, 2004a), the site of a massive flood (Burr et al., 2002b) on Mars.

Profiling photoclinometry is ideal for determining the meter-scale topography of the dune forms in Athabasca Valles, which are thought to be flood-formed (Burr et al., 2004b). This study measured the dune morphologies at 72 locations in MOC image E10/01384 (Figures 3.1, 3.2) in order to gain a robust measure of the dune shape for input into the flood model. The dunes were determined to be flattened, similar to Siberian dunes (Carling, 1996b), this flattening is most likely a result of a transitional stage during the receding flow.

The modeling indicated that the flood discharge that formed these dunes was about $2 \times 10^6 \text{ m}^3\text{s}^{-1}$ (Burr et al., 2004b). This value is similar to previous estimates from other methods, $1\text{-}2 \times 10^6 \text{ m}^3\text{s}^{-1}$ (Burr et al., 2002c; Burr, 2003), which are difficult to match with subsurface flow through a porous medium at the flood source.

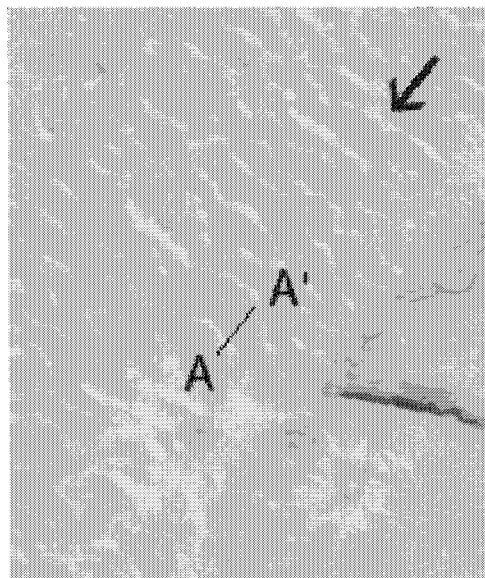


Figure 3.1: This image is a portion of the MOC image E10/01384 showing a dune-field in Athabasca Valles. The A-A' line is the profile that was taken to generate the topography seen in figure 3.2. The arrow indicates the direction of fluid flow.

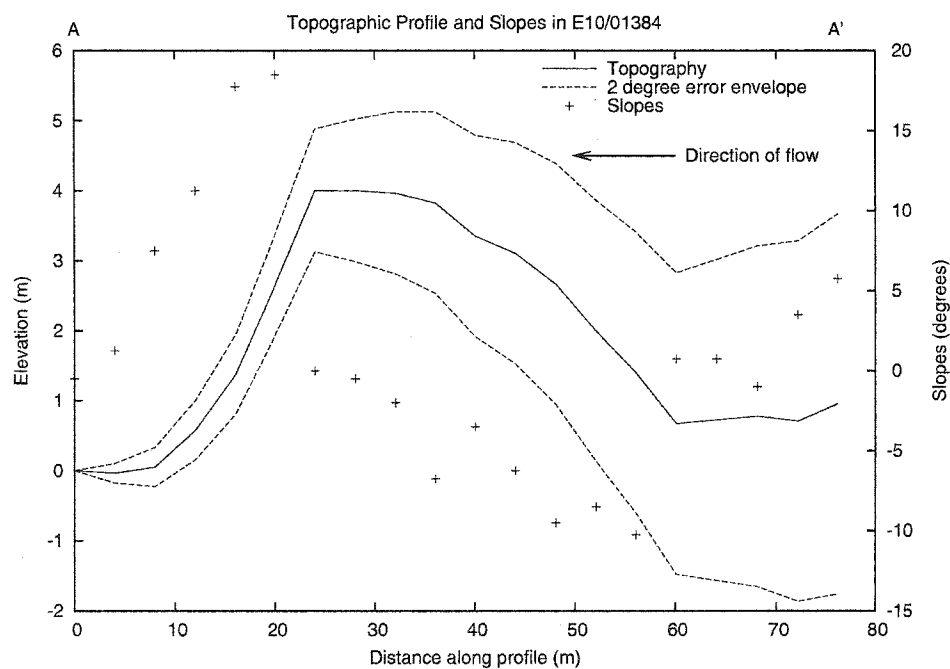


Figure 3.2: This image is the topographic profile generated from the brightness values under the profile in figure 3.1. The shape of the dune is evident, so is its flattened top.

This inconsistency may indicate that periodically or locally the martian subsurface is more permeable than terrestrial aquifers. Alternately, the flood may have eroded the aquifer host rock, such that aquifer permeability was not a constraint on the flow (Carr, 1996, p. 58).

Since there is no adequate MOC stereo coverage in this area, the only way to obtain the shape of these dune-forms was from profiling photoclinometry. This shape is a necessary input into the flow modeling technique which estimates flood discharge independent of channel shape and floodwater height.

3.3.2 Surface Texture on Surfaces with Dark Slope Streaks

Dark slope streaks are an enigmatic surface feature on the martian surface (Morris, 1982; Williams, 1991; Sullivan et al., 2001; Schorghofer et al., 2002; Aharonson et al., 2003). Some of these features have flow-like morphologic characteristics, which include branching and anastomosing patterns influenced by small topographic barriers. In order to test whether these streaks were formed by a flowing liquid (or liquid mixture) or a completely dry mechanism, using a hydrodynamic model to test the parameters is needed. In order to model these features with a Bingham viscoplastic numerical model, the meter-scale topography of the surfaces upon which these features are seen must be obtained.

Previously I have discussed obtaining slopes and topography from meter-scale features on an otherwise flat surface (§2.3.1, §3.2). For this study we were interested in meter-scale features on sloping surfaces. Fortunately, the boxcar filtering technique described in section 2.3.1 eliminates the long wavelength topography, effectively flattening out the slope of the surface, leaving only the small-scale features. If we restrict our measurements to only the sloping surface upon which streaks are observed, we can easily apply the profiling photoclinometry technique to these surfaces.

Furthermore, for this study we are not attempting to accurately model a particular surface, but to gain an understanding of the meter-scale textures that are present where slope streaks are observed. Several surfaces upon which slope streaks

are seen were measured (Figures 3.3, 3.4, 3.5, and 3.6). In general, the relief on these surfaces is two meters or less as derived from profiling photogrammetry. The features that make up this relief are roughly equidimensional or oblong in plan form as measured from MOC images. Their widths ranged from 5 to 30 m, and the more oblong forms were 30 to 300 m in length. The spacing between these landforms was often uniform on a particular slope surface and ranged from 20 to 60 m.

Based on these measurements, we decided to use oblong mounds 10 m by 30 m in plan form, and whose heights at their centers ranged from 1 to 2 m. In addition, the cross-sectional shapes of the mounds we used were sinusoidal, not ellipsoidal, to better approximate aeolian features. These mounds were then randomly distributed over a surface that is tilted at 10° (based on long wavelength topography from MOLA). Upon this surface a viscoplastic numerical model was used to simulate flow with different rheological properties (Miyamoto et al., 2003, 2004b).

This work (Miyamoto et al., 2004a) indicates that for those slope streaks which show a branching and anastomosing pattern, the viscosity is 10 Pa s, and the yield strength 10 Pa. Such flows would form within several thousand seconds (a few hours), and the density of such flows would be at least several tens of kilograms per cubic meter. Furthermore, these flows are not easily explained by a dry dust avalanche, but instead may be some kind of water-dust mixture with dust concentrations no more than 20% (Miyamoto et al., 2004a). Without the meter-scale topography of the surfaces upon which these streaks are observed, attempting to accurately model the slope streaks as fluid flow upon those surfaces would have been difficult.

3.3.3 Flexure of Europa's Elastic Lithosphere due to Ridge-loading

The icy surface of Jupiter's moon Europa may overlie a liquid water ocean at some depth (Anderson et al., 1997; Cassen et al., 1979). The total thickness of this shell is in great dispute, and a related issue is the thickness of the elastic lithosphere. One way to estimate the thickness of an elastic layer is to understand how it responds to an imposed load. Images from the Galileo spacecraft showed several instances of

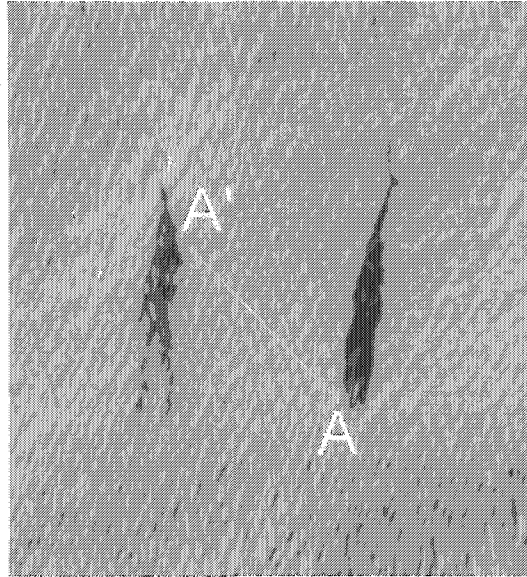


Figure 3.3: This image is a portion of MOC image M20/00014, which shows a slope upon which a pair of dark slope streaks are present. Uphill is towards the top of the frame. The A-A' line is the profile in the down-Sun direction that was taken to generate the topography seen in figure 3.4.

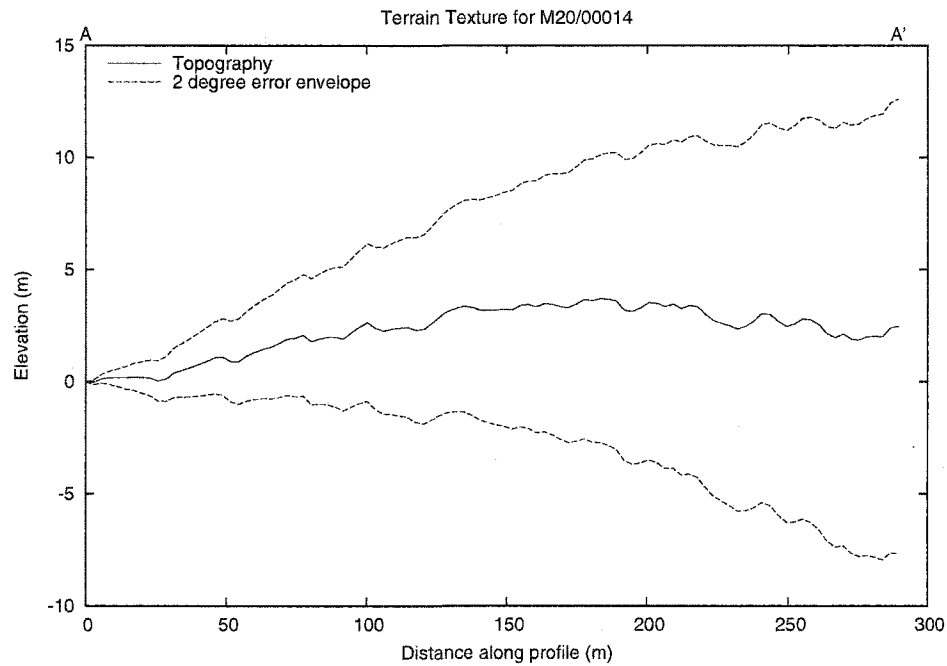


Figure 3.4: This graph is the topographic profile generated from the brightness values under the profile in figure 3.3.

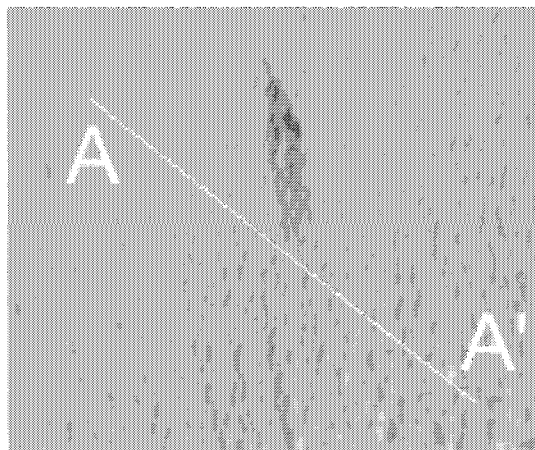


Figure 3.5: This image is a portion of MOC image M20/00897. It shows a slope upon which a dark slope streak is present, uphill is towards the top of the frame. The A-A' line is the profile that was taken to generate the topography seen in figure 3.6.

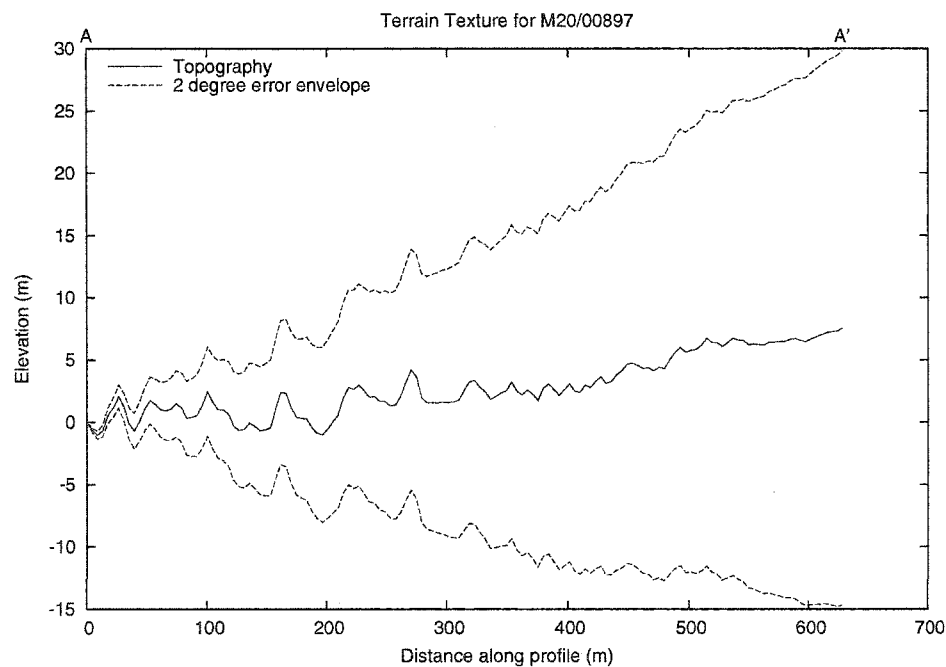


Figure 3.6: This graph is the topographic profile generated from the brightness values under the profile in figure 3.5.

crustal downwarping near the long linear ridges on Europa, and secondary uplifts (e.g. Tufts et al., 1997). Due to their favorable illumination conditions, estimates of the thickness of the elastic lithosphere could be made, giving about 200 m (Tufts, 1998). Observations of flexure near chaos regions were used to infer a similar thickness for the elastic lithosphere, between 100 and 500 m (Williams and Greeley, 1998).

Tufts et al. (1997) were able to use shading and secondary fractures in the images to determine the distance, d , to the secondary crest (Figure 3.7). This technique allowed them to determine the thickness, h , of the elastic lithosphere with the following equation, derived from Turcotte and Schubert (2002):

$$h^3 = \frac{3\rho g(1 - \nu^2)}{E} \left(\frac{4d}{3\pi} \right)^4 \quad (3.4)$$

where d is the distance to the secondary crest, ρ is the density of the elastic lithosphere, g is the surface gravity, ν is the Poisson's ratio and E is the Young's modulus of ice.

We extended this investigation by applying the profiling photoclino-metry technique to Europa and using the resulting topographic profiles to measure the distance to the secondary uplift crest (Figures 3.8, 3.9).

This application of profiling photoclino-metry allowed us to determine the thickness of the elastic lithosphere at a number of different places on the surface of Europa (Hurford et al., 2003, 2004), and the thicknesses we derive are similar to previous estimates. However, our ability to make measurements all over the surface of Europa allows us to begin to look at differences with terrain type and latitude. Additionally, our measurements indicate that the elastic lithosphere of Astypalaea Linea is thicker than the surrounding terrain. This result is consistent with the Tufts et al. (2000) model in which dilational bands thicken if they are worked by diurnal tides.

This work will allow us to place constraints on the structure and origin of terrains on Europa. Until more detailed topographic data can be obtained via stereogram-metry or laser altimetry, profiling photoclino-metry is the only way to obtain the

distance to the secondary uplift crests that result from loads on the elastic lithosphere.

3.3.4 Comparison of Methods Used to Constrain Aeolian Bedform Morphometry

In order to obtain a better understanding of the morphometric parameters (like height, width, length, surface area, volume, longitudinal and cross profiles) of aeolian dunes on Mars, various techniques for estimating small scale topographic parameters have been applied to the same dune-forms (Bourke et al., 2004). Ripples and barchanoid dunes in several locations were analyzed with a slip face measurement method, stereogrammetry, and my profiling photoclinometry technique.

This work is ongoing, but initial measurements by the various methods agree reasonably well (Bourke et al., 2004), giving improved confidence in the results returned by my profiling photoclinometry technique. While profiling photoclinometry is not the only method being used in this study, it is an integral part of a collaborative effort to constrain the morphometry of aeolian bedforms on Mars.

3.4 Conclusion

These applications show that the profiling photoclinometry technique I developed from the point photoclinometry technique described in chapter 2 can be used to provide a reasonably accurate topographic profile with a horizontal resolution on the order of the image resolution from which it was derived. This technique allows investigation of various scientific questions that have been difficult or impossible to address due to lack of high-resolution topographic data.

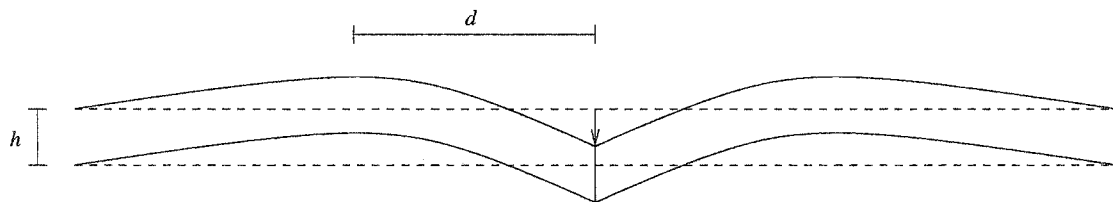


Figure 3.7: This figure is adapted from Turcotte and Schubert (2002) figure 3-31, and shows the way that a fractured layer reacts to an applied line load. The thickness of this elastic layer is h , and the horizontal distance from the load to the secondary uplift crest is d . Ridges on the surface of Europa may act as linear loads and the European lithosphere is expected to behave in this manner.

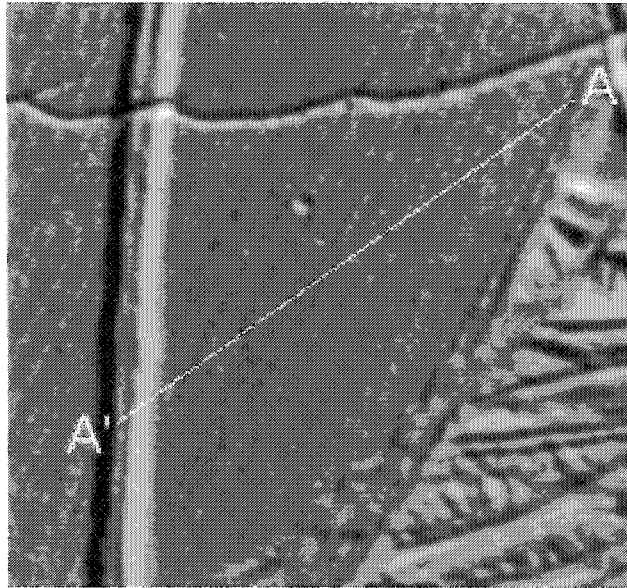


Figure 3.8: This image is Galileo image S0466670126 from orbit E17, which shows an example profile (constrained to be in the direction of the Sun) across a ridge within the Astypalaea Linea structure.

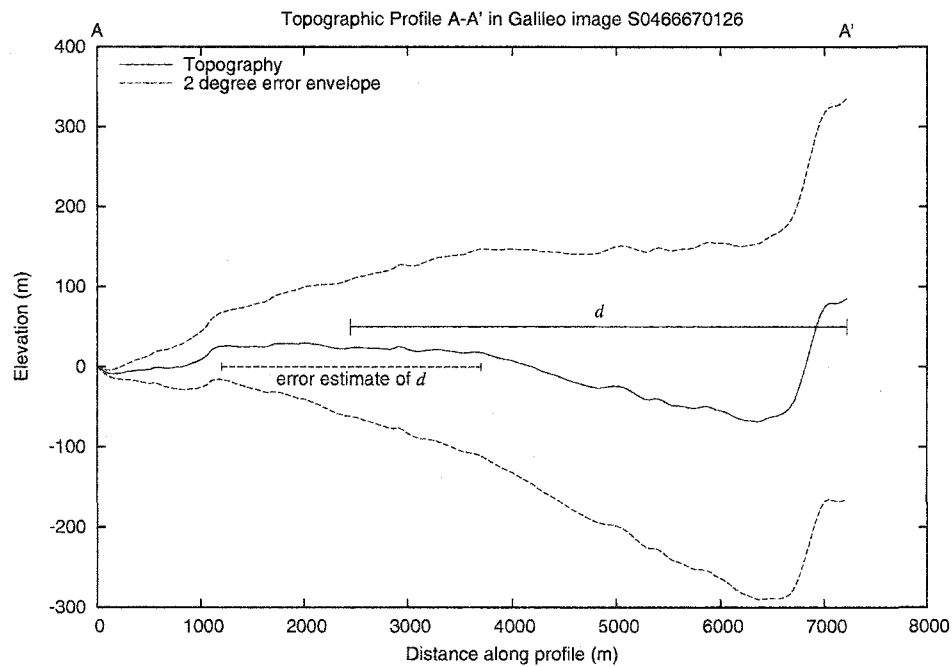


Figure 3.9: This graph is the topographic profile resulting from Figure 3.8. The secondary uplift crest can be identified here. The figure shows how the value of d is measured, as well as the error estimate of that value.

CHAPTER 4

Stratigraphy of Eastern Coprates Chasma, Mars

4.1 Overview

This chapter is being prepared for submission to the journal *Icarus*, by Ross A. Beyer and Alfred S. McEwen. Alfred McEwen aided in focusing certain elements of the analysis and discussion and contributed to the overall style and presentation of the manuscript.

Distinct competent layers are observed in the slopes of eastern Coprates Chasma, part of the Valles Marineris system on Mars. These layers are visible in both Mars Orbital Camera (MOC) and Thermal Emission Imaging System (THEMIS) images. Our observations indicate that the stratigraphy of Coprates Chasma consists of alternating thin strong layers and thicker sequences of relatively weak layers. The strong, competent layers act to maintain steeper slopes and play a major role in controlling the overall slope and geomorphology of the chasma walls. The topmost competent layer in this area is well preserved and easy to identify in outcrops on the northern rim of the chasma less than one hundred meters below the southern Ophir Planum surface. Also in the eastern portion of Coprates Chasma there is a massif that consists of chasma wall rock material. It is characterized by flat-topped areas at its crest. They are a significant characteristic in the Valles Marineris because it preserves the surface of pre-existing plains on a free-standing massif. The flat-topped areas and the massif itself owe their continued existence to the presence of the topmost strong layer, which crops out less than one hundred meters below the level of the flat-topped surfaces and supports the massif against mass wasting. The volume of the topmost emplaced layer is at least 70 cubic kilometers and may be up to 2100 cubic kilometers if the unit underlies most of Ophir Planum. Elevation measurements from the Mars Orbital Laser Altimeter (MOLA) show a difference in

elevation of 150 m to 350 m between the north rim outcrops and the massif outcrops. A promontory on the north rim to the west of the massif shows evidence of similar subsidence, and the massif itself also displays a down-dropped block in one of the flat-topped areas. These observations are evidence of significant subsidence of the massif and surrounding material.

4.2 Introduction

The Mars Orbital Camera (MOC) (Malin et al., 1992; Malin and Edgett, 2001) on-board the Mars Global Surveyor (MGS) spacecraft has observed extensive layering near the martian surface and in the Valles Marineris system (e.g. McEwen et al., 1999; Malin and Edgett, 2001). Layering exposed in the walls of terrestrial canyons is often sedimentary in nature, with new layers having been deposited from rivers, lakes, or oceans. Alternately, volcanic processes with multiple episodes or pulses of activity can deposit many layers of volcanic rocks and/or tephra, and intrusive magmatism can also create layered sequences at depth that are later revealed by erosion and uplift. The Valles Marineris is the only feature that cuts down over 9 km into the martian crust. The origin of the layers is unknown, but there are hypotheses for both fluvial sedimentary (e.g. Malin and Edgett, 2000) and volcanic origins (e.g. McEwen et al., 1999; Williams et al., 2003). Also relevant to the exposures that we see today are the formation processes of the giant chasma system itself (e.g. Sharp, 1973; Tanaka and Golombek, 1989; Schultz, 1991; Lucchitta et al., 1992, 1994; Peulvast et al., 2001; Mège et al., 2003) and what geologic changes the region has gone through since these chasmata opened.

In order to gain more insight into these questions, we have analyzed data from the MOC, the Mars Orbital Laser Altimeter (MOLA) (Zuber et al., 1992; Smith et al., 2001), and the Thermal Emission Imaging System (THEMIS) (Christensen et al., 1999, 2003a). Layering can be seen in the high-resolution MOC images, and correlated with particular heights from individual MOLA tracks. In addition to the tracks that were acquired simultaneously with many MOC images, there are a

larger number of MOLA tracks that criss-cross an area not tied to any particular image. The THEMIS infrared multi-band images at 100 m/pixel and visible wavelength images at 18 m/pixel are useful for tracing layers, and for constraining their thermo-physical properties (emissivity and thermal inertia). Combining the visible and thermal imaging datasets with a topographic dataset has allowed us to better understand the three-dimensional relationships of the observed ground forms in a way that each dataset individually would not be able to do.

We examined layering seen in the eastern portion of Coprates Chasma (Figures 4.1, 4.2). We estimated layer thickness and measured the horizontal extent and elevations of layer outcrops. Layers are traced across several images to determine how far they extend along the chasma. This mapping allows us to determine if the layers are flat-lying or if they dip down in a particular direction over large distances. Lacustrine or deep oceanic deposits should be horizontal unless they have been tectonically tilted, in which case the tilted layers should have a systematic relationship to regional tectonics. Air-fall ash or dust will drape over preexisting topography. Sand will pile up against topographic obstacles. Lava flows will be largely but not entirely horizontal. Horizontal layers may also be interbedded lavas and sediments.

Our observations indicate that the stratigraphy of Coprates Chasma consists of alternating thin (tens of meters) sequences of strong layers and thicker (hundreds of meters) sequences of relatively weak layers. The competent layers act to maintain steeper slopes and play a major role in determining the overall slope and geomorphology of the chasma walls. The strong layers occur singly, or in thin sequences compared to the more massive sequences of intervening relatively weak layers. The competent layers are the source of boulders and blocks that can be seen just downslope of some outcrops.

Our ability to confidently trace layers in the chasma decreases with decreasing elevation and slope. Layers near the top of the stack are easy to identify because they are not covered by talus. Similarly, mantling deposits can easily cloak outcrops of a strong unit on a relatively smooth slope, whereas just around a spur that same unit can be easily identified as a cliff former. The topmost competent layer in this

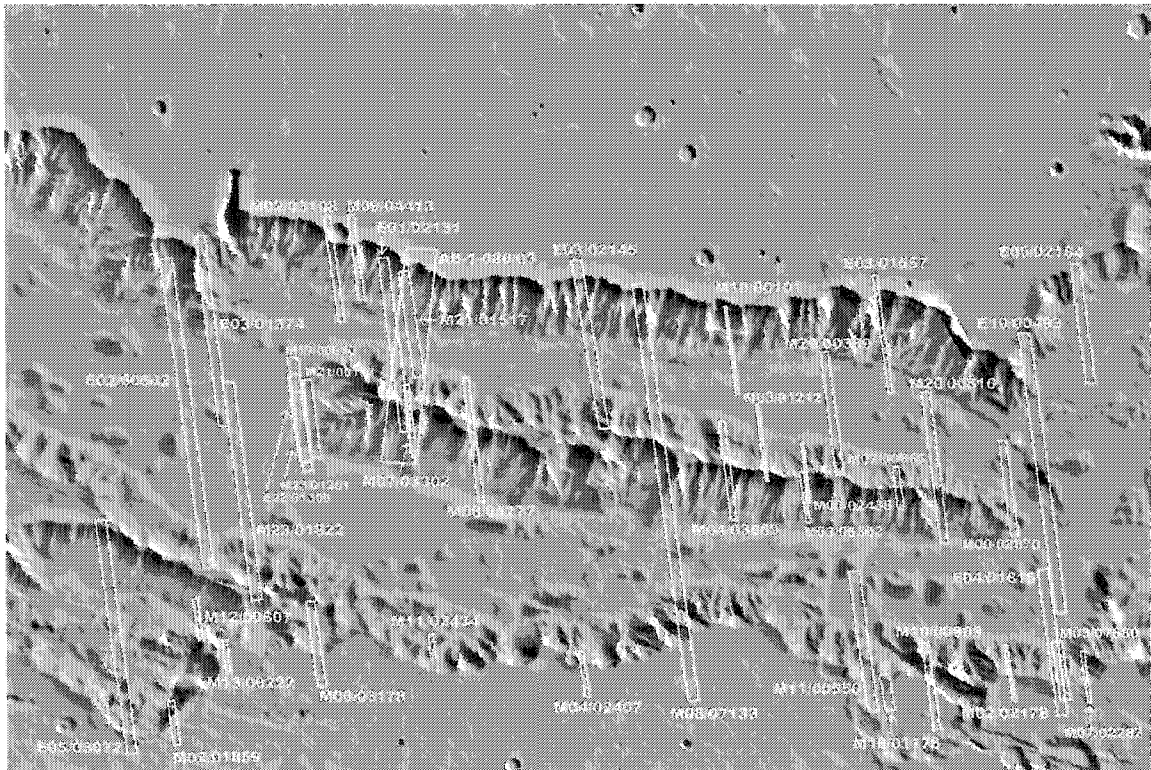


Figure 4.1: This Viking mosaic (MDIM2), shows the primary study area of eastern Coprates Chasma. The locations of MOC narrow-angle images are indicated by their outlines in yellow. Not all of the images are specifically referenced in this study because either they do not cover regions of interest or they are similar to images that we present.

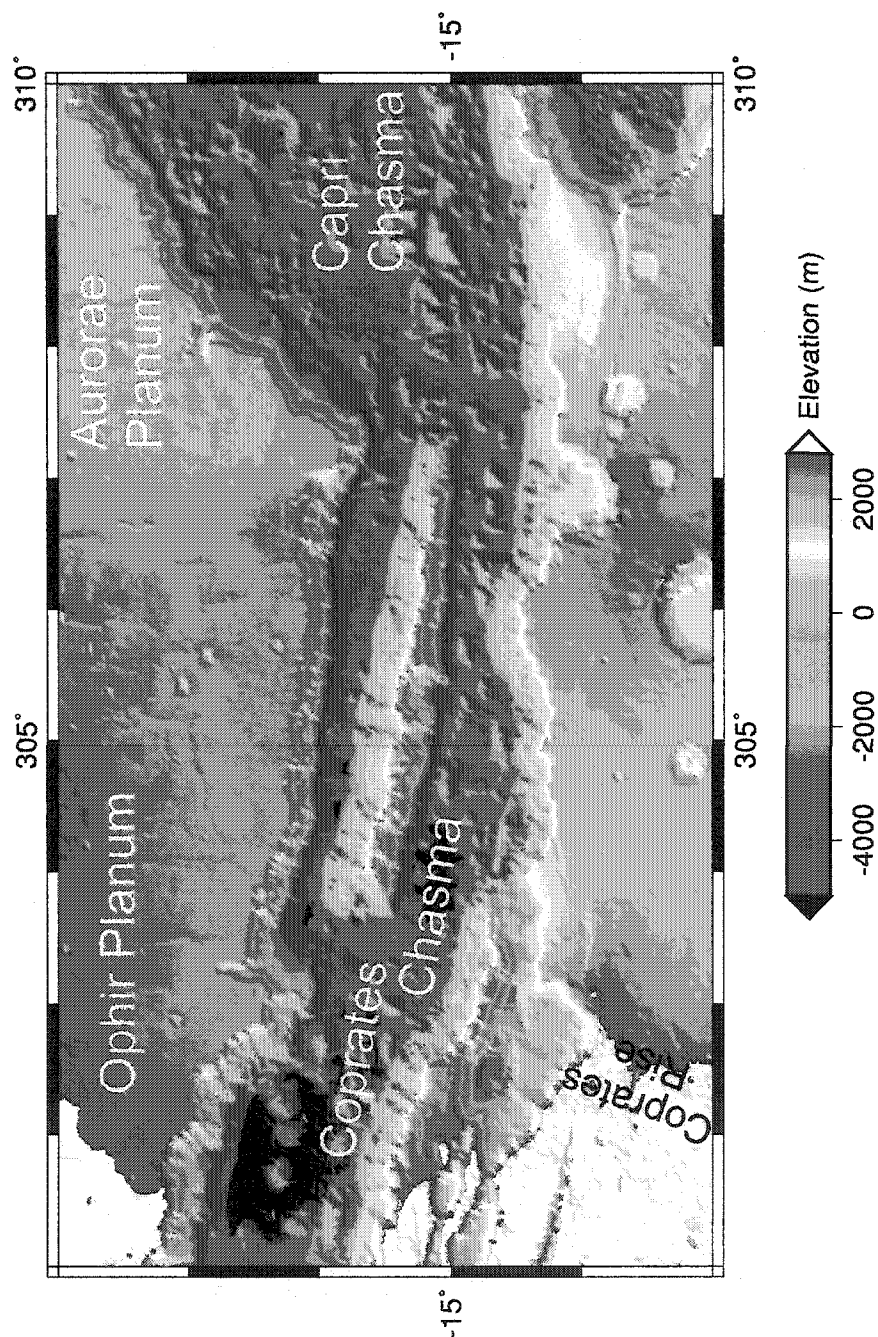


Figure 4.2: This elevation map of eastern Coprates Chasma was created from the 1/128th degree MOLA gridded data.

area is well preserved and easy to identify in outcrops in the northern slope of the chasma less than a hundred meters below the plateau surface.

Our observations and measurements of these distinct competent layers are consistent with dense basaltic lava flows. Therefore, by contrast the intervening layers must not be dense basalts. Our measurements of the strike and dip of the topmost competent layer in this area indicate that this portion of the Valles Marineris was subjected to north-south extensional tectonism, and subsidence.

We begin with a brief description of the method we used to obtain the layer elevations (§4.3). We then state the observations that we made of the massif, the chasma rims, and chasma slopes in the eastern Coprates Chasma region (§4.4). We have tried to not discuss the implications of our observations in that section, but instead discuss our interpretations of them in a separate section that follows (§4.5).

4.3 Layer Elevation Measurement Method

Obtaining an accurate measurement for the elevation of an outcrop of thin (~ 10 m thick) layers with MOLA data cannot be done by simply reading off the elevation of individual MOLA shots. MOLA footprints are 168 m in diameter (Smith et al., 1999a) and have center-to-center spacings of about 300 m. This footprint size and spacing means that a MOLA shot, even if it happens to fall directly on a thin layer is also sampling the elevations above and below that layer. More often than not, the layer outcrop is between MOLA shots. However, these layers often sit above constant slopes, which can be exploited to gain a measure of the elevation of the layer.

The slope below the layer often has many MOLA shots on it (Figure 4.3), and a measurement of that slope, θ , can be made. Using correlations between MOC and MOLA data, the plan form distance, s , between the center of the MOLA shot just below the layer and the layer itself can be measured. We can then find the difference in elevation, h , between the elevation of the layer and the elevation of the center of the MOLA shot just below the layer with the equation $h = s \tan \theta$. From this,

we can get a measurement of the absolute elevation of the thin layer. This method works even if the orientation of the MOLA track is not perpendicular to the strike of the layer outcrop as long as s is measured along the direction of the MOLA track.

When we quote an elevation measurement in this study, that elevation measurement is based on the topography value reported by MOLA. This is the planetary radius (the distance from the center of Mars to the point on the surface) minus the areoid radius (the radius of the reference areoid with a 3396 km mean equatorial radius). It is the equipotential topography at the shot location (Smith et al., 1999a).

THEMIS data are useful for providing continuity between MOC images and regional context. The THEMIS visible imager data have a resolution of about 18 m/pixel, which cannot truly resolve the thin dark layers that we investigate in this study. However, one can often trace linear features whose width is less than the size of the resolution element, and THEMIS VIS images are helpful for tracing these thin layers between or beyond better resolution MOC images. THEMIS IR data have a resolution of 100 m/pixel, which is far too coarse for the thin layers in this study, but is helpful for regional context information.

4.4 Observations

4.4.1 Massif in Eastern Coprates Chasma

There is a large massif in eastern Coprates Chasma, situated closer to the north wall of Coprates Chasma than the southern wall, right before the Valles Marineris widens into Capri Chasma (Figures 4.1 and 4.2). It is located near 15° S, between 304° and 307° E. MOC images display spur-and-gully morphology and layers on the massif that are very similar to the chasma wall rock. The massif appears to be compositionally and structurally similar to the chasma wall rock as well (Frey, 1979; Schultz, 1991). This massif has a few flat-topped areas along its roughly 230 km length. Figure 4.4 shows MOC and THEMIS context images over the largest flat-topped area of the massif, near its western end. These images show the smooth texture of the flat surface and its comparatively low temperature at night indicating

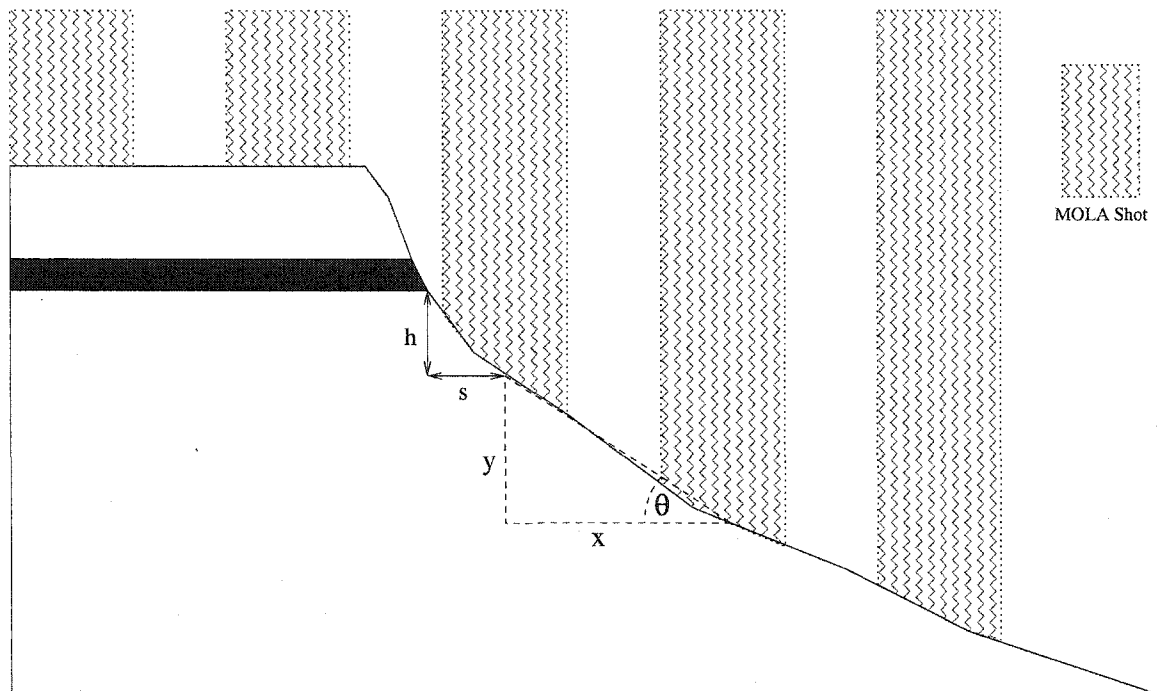


Figure 4.3: This cartoon shows an example cross-section at the top of Eastern Coprates Chasma and the way that MOLA measurements intersect with the surface. It illustrates how we obtain an accurate elevation measurement for the outcrop of the thin dark layer. See §4.3 for an explanation of the symbols.

that the top surface has a lower thermal inertia than the bedrock exposed along the eroded slopes of the massif, and a lower thermal inertia than the materials on the floor of Coprates Chasma around it. The flat-topped areas along the spine of the massif are most likely the remnants of the plains surface that covered this area prior to the opening of Coprates Chasma.

Just below the level of those flat-topped areas on the massif and in other places along the crest of the massif, a distinct, dark-toned layer can be seen (Figure 4.4a), even in sunward facing slopes (Figure 4.5). Figure 4.6 shows higher resolution images highlighting this resistant cliff-forming unit which outcrops below the flat-topped surfaces. Since this layer can be seen everywhere along the edge in Figure 4.5, and a layer with a similar expression and morphology is observed 22 km further east (Figure 4.6), we think that this may be a very extensive layer. In fact, there are several MOC images along the massif where a layer with very similar characteristics is exposed, and they are listed in Table 4.1.

The elevation measurements of this topmost strong layer (Table 4.1) allow us to estimate the dip of this layer. At this point we will assume that the layer was originally horizontal (see §4.5.1 for why we think that is a reasonable assumption). We can measure dips in two general directions. The massif is oriented roughly east-west, with its general strike about 10° north of west, and we have several outcrop measurements along it. There are also a few places where the layer is exposed on both the north face and the south face of the massif, allowing us to measure a few dips in a more north-south direction.

The easternmost outcrop shows two measurements in Table 4.1, because we can see the layer outcrop on both the north and south faces of the massif in this MOC image (Figure 4.7). These elevations reveal that the layer dips down to the south within the massif itself at 3.65° over a 610 m distance (this is the most extreme dip observed). The layer also outcrops on both the north and south faces of the massif in MOC image AB-1-080/03 over the largest flat-topped area of the massif (Figure 4.4a), but the difference in elevation is only a few meters over a much greater distance.

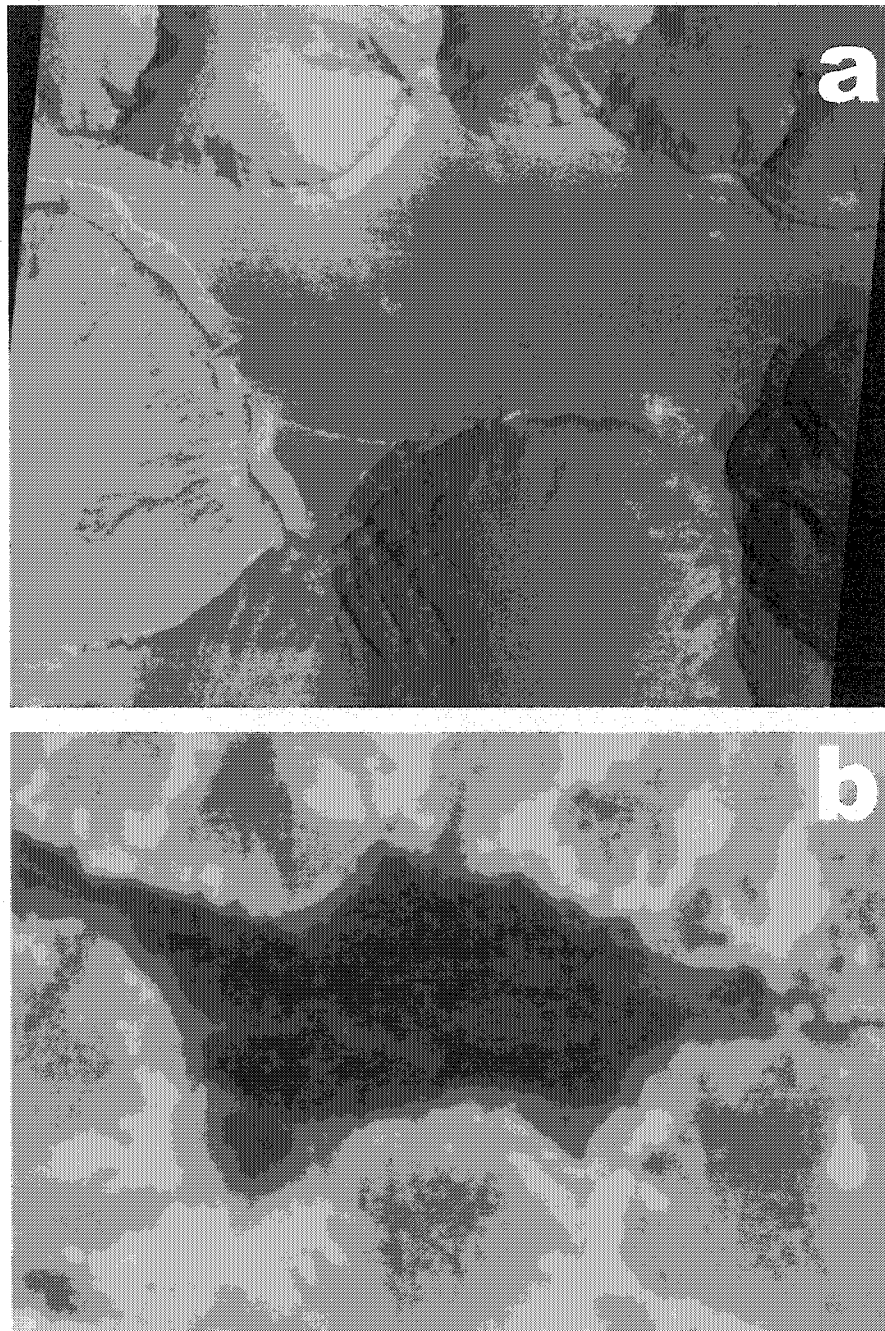


Figure 4.4: These images show context for the westernmost flat-topped area on the massif in eastern Coprates Chasma. *a.* MOC image AB-1-080/03, 4.7 m/pixel. *b.* THEMIS nighttime IR brightness temperature image I00820002, 100 m/pixel. All images in this study are displayed with north to the top.

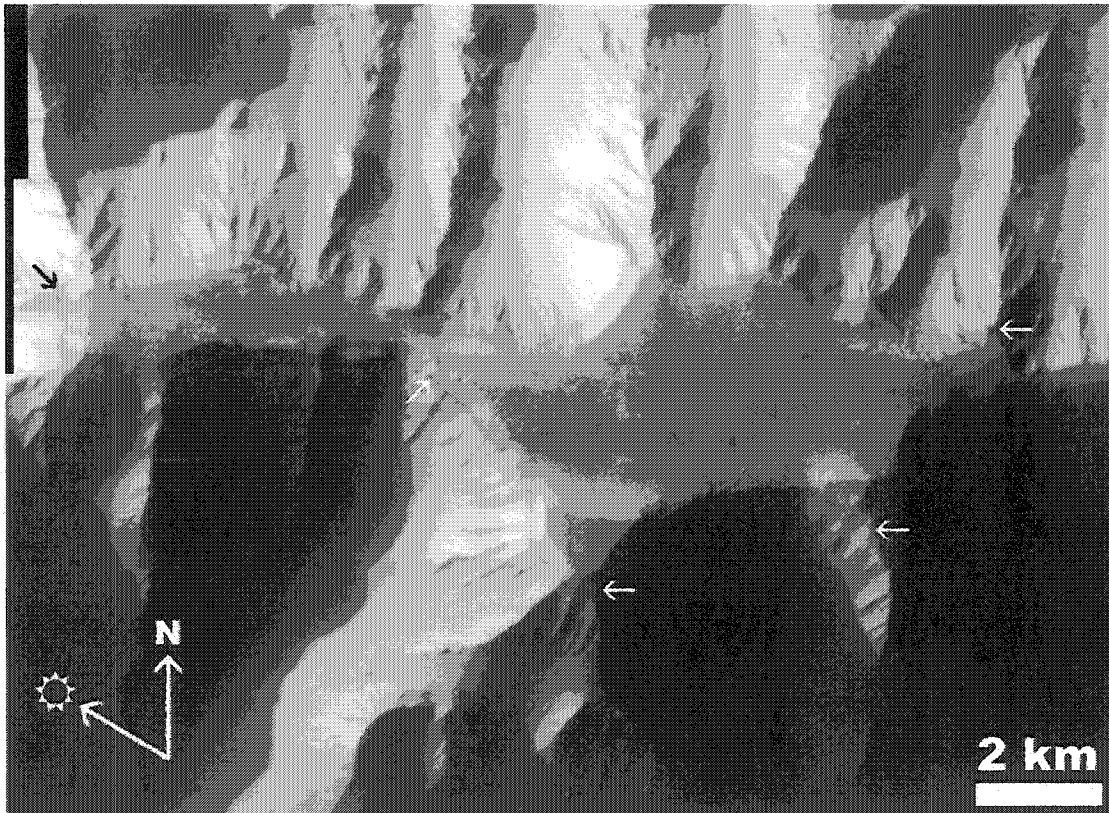


Figure 4.5: This is THEMIS VIS image V03810003. It shows the westernmost flat-topped area of the massif in Coprates Chasma and a dark, competent layer below the level of the flat top. This layer can clearly be seen, even on sunward-facing slopes, demonstrating that it has a lower albedo. This dark layer is indicated by arrows.

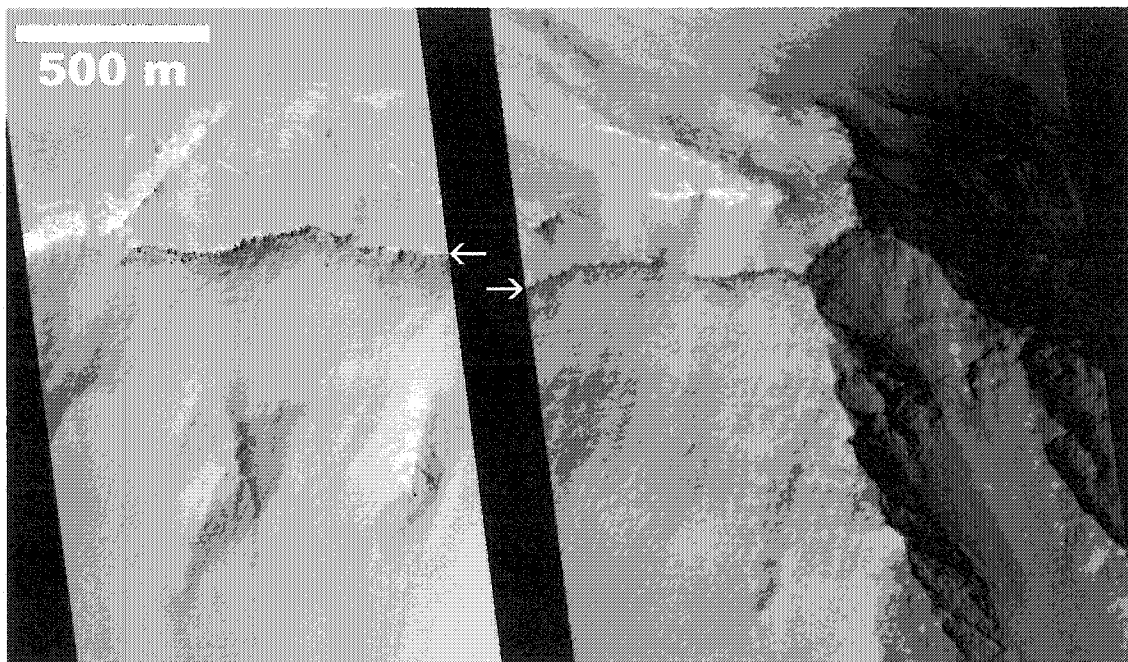


Figure 4.6: These MOC images show the cliff-forming layer near the top of the flat-topped areas on the massif. In both images, the south face of the massif slopes down towards the bottom of the image. The image on the left is M07/03302 and the image on the right is M08/05277 they are separated by about 22 km. M08/05277 has been enlarged so that both images are at the same scale.

Competent Layer Outcrop Elevations					
MOC Image		MOLA Orbit	Elevation (m)	E Longitude	Latitude
Massif Outcrops					
AB1/08003	12359	1895 (N)	304.16		-14.40
		1905 (S)	304.17		-14.46
M08/05277	12774	2034	304.50		-14.56
M04/03869	12120	2160	305.86		-14.74
M03/06302	11793	2180 (N)	306.25		-14.78
		2130 (S)	306.25		-14.79
M00/02438	10460	2130	306.27		-14.79
North Rim Outcrops					
M09/04413	13101	2273	303.88		-13.61
E03/02145	19526	2300*	305.12		-13.77
M08/07133	12862	2330	305.36		-13.83
E03/01557	19438	2409*	306.76		-13.87

Table 4.1: These measurements are in order from west to east. They show the MOC image with which the MOLA track that gave the elevation measurement was matched. M03/06302 and M00/02438 are very near one another.

* These measurements have an error on the order of 100 m because these MOLA tracks have pointing uncertainties that make precise alignment with their MOC images difficult.

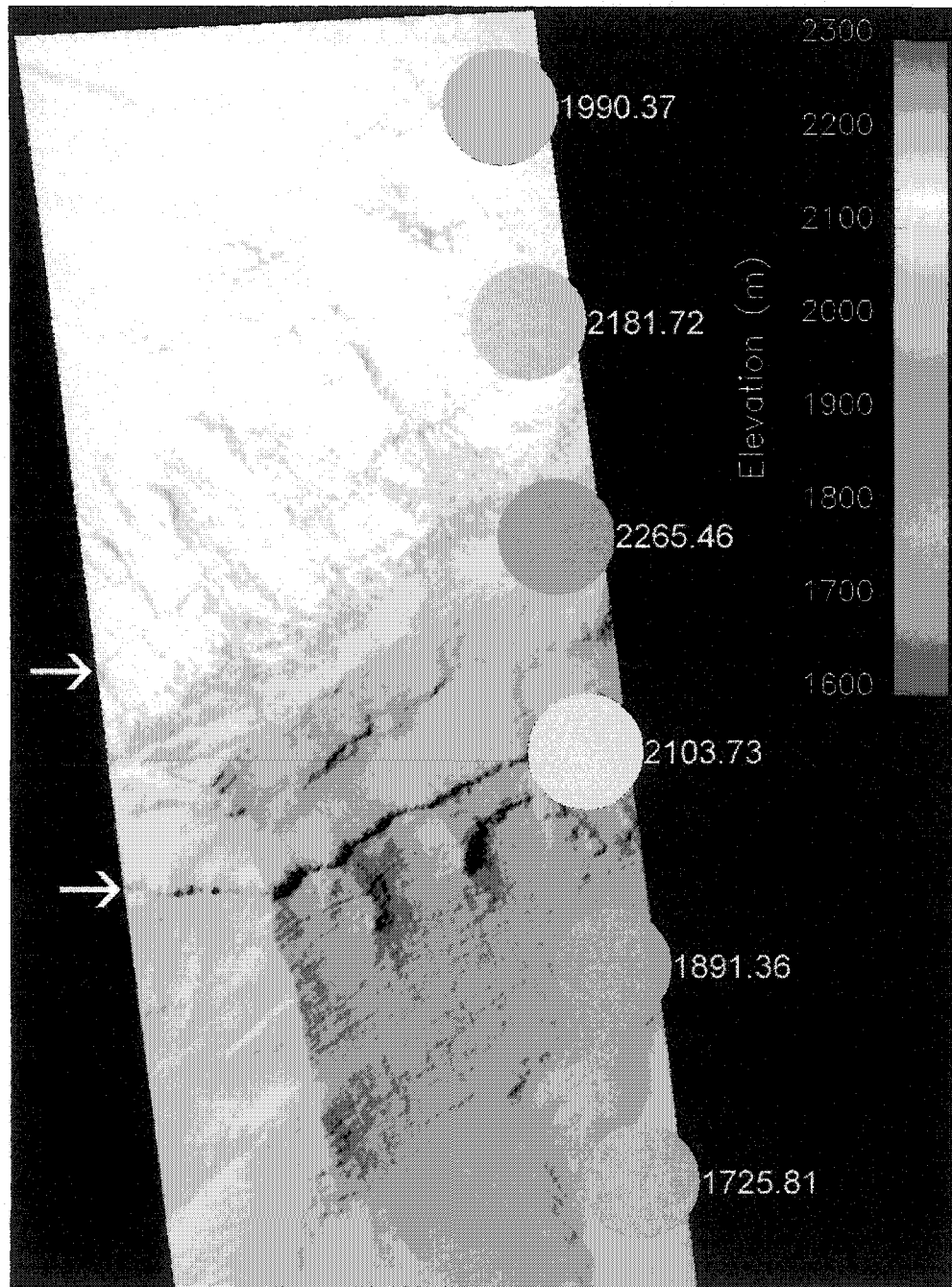


Figure 4.7: This is a portion of MOC image M03/06302, with the MOLA data from the track that was acquired simultaneously with the image plotted on top. The size of the spheres is the approximate size of the MOLA footprint (168 m diameter). This image covers the crest of the massif, and the white arrows point to the outcrops of the competent layer.

The layer in the massif essentially has three segments from east to west as shown in Figure 4.8. The westernmost segment has a dip of 0.39° down to the west over a 20 km distance, the next segment has a dip of 0.09° down to the west over a 78 km distance. The easternmost segment has a dip of $\pm 0.05^\circ$ over 23 km. The $+0.05^\circ$ (which would dip down to the west) is for the outcrop on the northern face of the massif in Figure 4.7, and the -0.05° (which would dip down to the east) is for the outcrop on the southern face. The total dip from the easternmost outcrop to the westernmost outcrop is 0.13° down to the west over the entire 122 km.

The topmost strong layer also highlights an excellent example of north-south extension on the largest flat-topped area of the massif. The MOC image E01/02131 (Figure 4.9) shows the strong layer about a hundred meters below the flat-topped level of the massif, and a 420 m length that discontinuously appears much lower below the massif top. It highlights a block which has dropped about 70 m relative to the elevation of the rest of the strong layer, based on extrapolations of the elevations of the topmost strong layer here. Additionally, we can estimate the dip angle of these normal faults and find them to be at the expected value of 60° . The topography of this flat-topped area also indicates a small depression that overlies this down-dropped block at the top of the massif. MOLA measurements indicate that this depression is about 60 m deep at its western end just above where the down-dropped block is observed in the massif slope. Not much is visible downslope of the down-dropped layer, because talus covers the slope. Similarly it is difficult to ascertain where the normal faults that bound the block may outcrop to the east. There are no high-resolution images that would allow us to find the layer, and additionally the eastern side of this flat-topped area is in shadow as seen by spacecraft in afternoon orbits. The depression that is identifiable in the MOLA data directly over the down-dropped block on the western side seems to reach about half-way across the flat-topped area (from west to east), but the normal faults may well be discontinuous, and may be present across this whole flat-topped area. There is a small, higher-standing area in the southeast portion of this flat-topped area (bottom right portion of flat-topped area in Figure 4.4 and above bottom right arrow in Figure 4.5), which

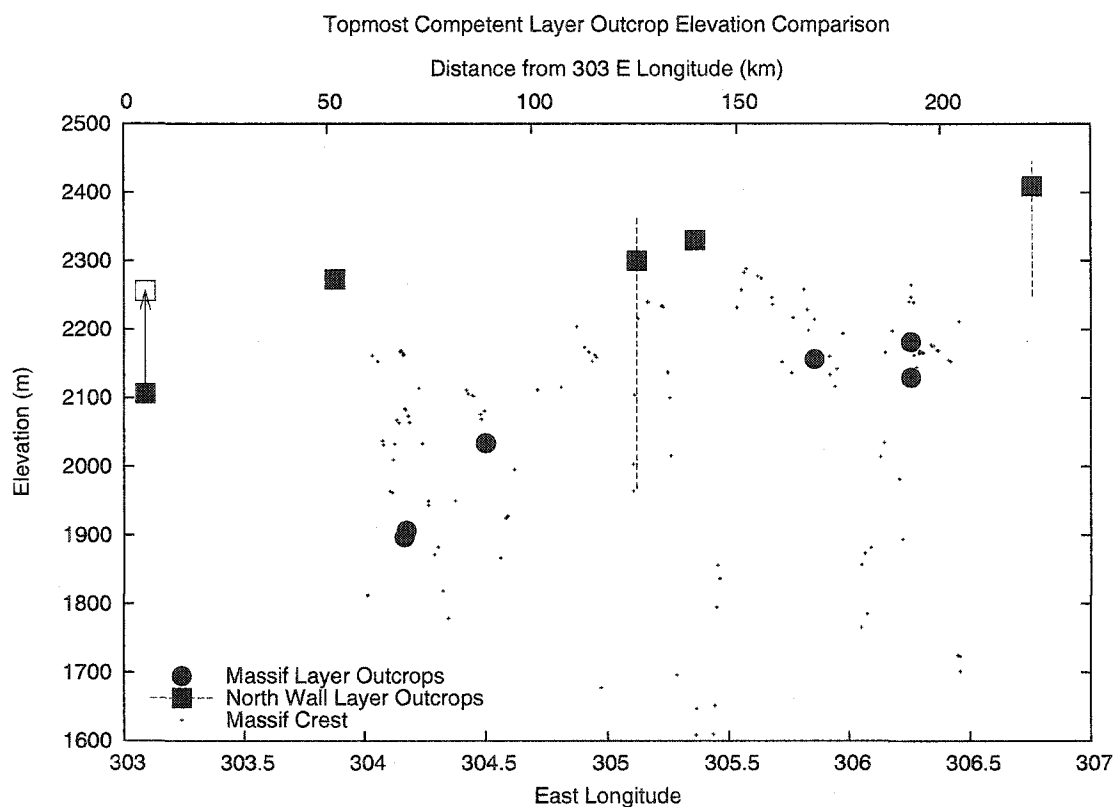


Figure 4.8: This shows the east longitude of the topmost strong layer outcrop locations and their elevations both in the massif and in the north rim of eastern Coprates Chasma. The elevations of the crest of the massif are also plotted to show the variability of the massif crest in relation to the layer outcrops. The westernmost north rim data point has an arrow which points to the estimated elevation of the layer in this location prior to the 150 m down-dropping of this portion of the plateau. The error bars on the other two data points result from imperfect pointing information which prevents accurate MOC/MOLA alignment for these outcrops.

might be bounded on the north by a normal fault, but there is no evidence to directly support this.

The topmost strong layer is the most easily identifiable layer in the stack due to its visual contrast and high apparent strength. However, other resistant layers can be identified below it. The next exposure of competent layers is part of a sequence at least 200 m thick. It is difficult to tell if this sequence is varying in thickness from place to place or if the talus buries it to different levels at its base. This sequence also contributes to the steep slopes near the crest of the massif and supports a topographic bench in MOC image M08/05277 (Figure 4.10) stratigraphically below the topmost strong layer. Unlike the distinct topmost layer, this unit appears to be a sequence of more resistant layers, and while not as dark as the topmost competent layer, it does have a slightly darker tone than surrounding weak layers.

The western exposures of this topmost layer and next most competent unit appear to have a 100 m thick sequence of slightly lighter-toned thinly bedded materials between them. However, M03/06302 and M00/02438 (in the eastern part of the massif) do not show such a gap between these two units. The gap or lack thereof between these units is identified based on slope morphology and a slight change in tone between the intervening weak layer and the next competent unit. To determine whether these strata represent a true unconformity or if we are not correctly interpreting these exposures will require higher resolution coverage.

Other competent layers are seen further down the stratigraphic stack but are more difficult to discern due to the amounts of talus that mantle the slopes. These lower competent units are evident by occasional spurs or ridges that crop out from the talus mantle on the slopes. However, it is difficult to correlate these layers along the chasma slopes because they are not evident everywhere at a particular elevation due to the spur-and-gully morphology of the slopes, and the differential accumulation of talus at different locales.

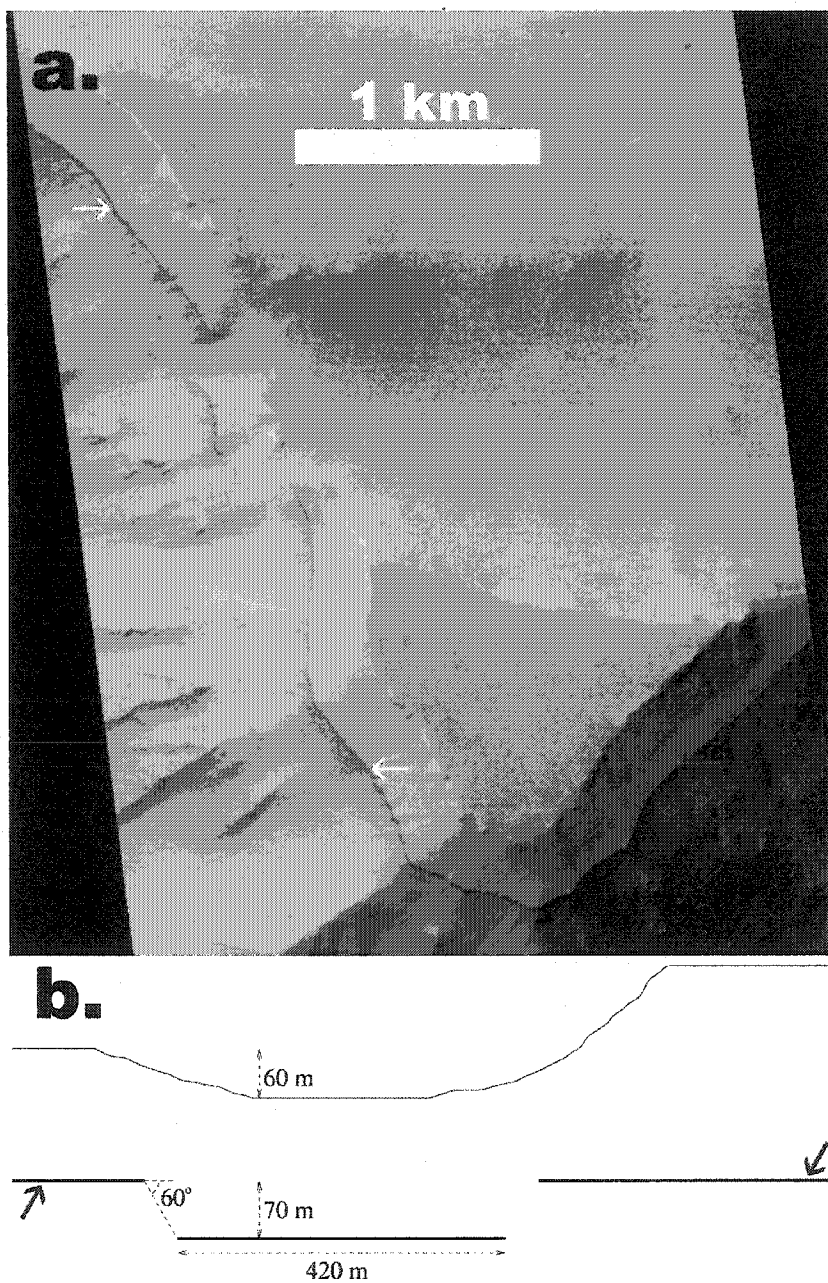


Figure 4.9: *a.* This portion of MOC image E01/02131 shows a closeup of the westernmost flat-topped area shown in Figure 4.4a. The white arrows correspond to the locations of the black arrows in the schematic. *b.* This cartoon schematic illustrates the down-dropped block as seen from the west. It shows that the dark layer exposed on the western facing slope has a 420 m long segment that is about 70 m in elevation below the level of the majority of the dark layer. These distances and elevations were derived from MOC and MOLA data.

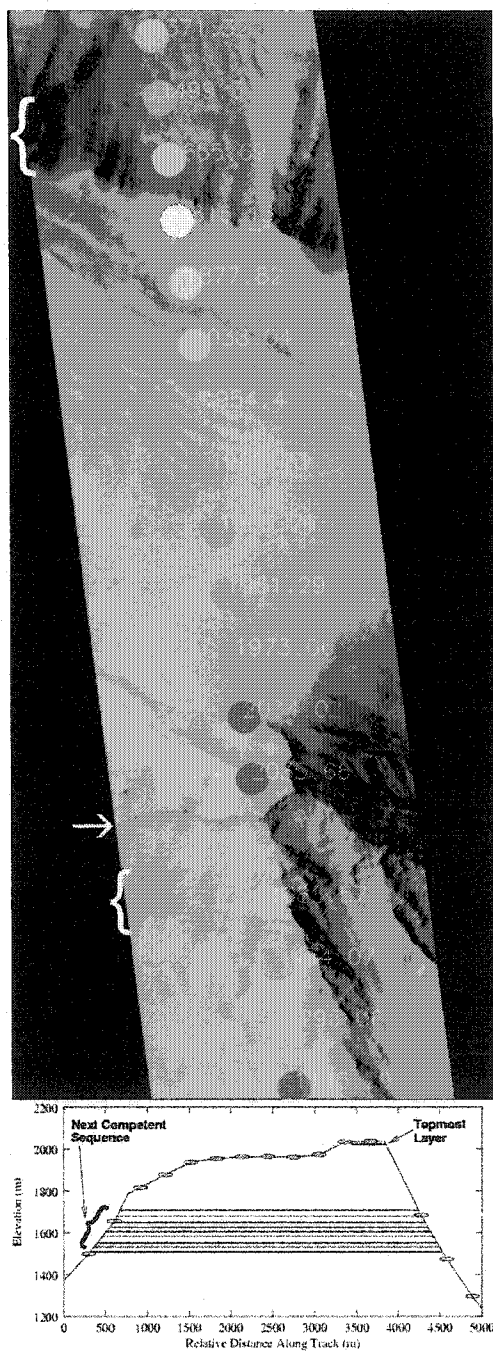


Figure 4.10: This portion of MOC image M08/05277 is overlaid with MOLA track 12774, north is to the top. It shows that slopes are locally steepened by the presence of the topmost dark layer (indicated by an arrow on this image). However, stratigraphically below that there is a topographic bench. This bench appears to be supported by the next most competent sequence of layers (which is visible on both the north and south sides of the massif as indicated by the brackets). The schematic at the bottom gives a view from the west, north is to the left, and the vertical exaggeration is 2.5.

4.4.2 Coprates Chasma, north of massif

The topmost strong layer observed in the massif is also evident directly north of the massif near the top of the north slope of Coprates Chasma. The high-resolution MOC coverage is sparse, but we can find several outcrops of this layer in the slope directly to the north of the Coprates massif (see Table 4.1). Unfortunately, due to small pointing errors in the MOLA dataset, only two of these four MOC images can be precisely aligned with their MOLA tracks. These two outcrops are separated by 86 km and the elevation difference is only 60 m, yielding a 0.04° slope. Our estimates for the elevations of the other outcrops are consistent with this slope as well. These measurements indicate that the topmost strong layer in the north slope of Coprates Chasma is flat-lying relative to the layer in the massif. The relative elevations of the outcrops in the north rim of Coprates Chasma are higher than in the massif (Figure 4.8). If we assume that the layer in the north slope and the layer in the massif were once a relatively flat-lying horizontal layer, then relative motions since deposition have altered it.

The next unit of strong layers seen to crop out below the topmost strong layer in the massif is also evident here on the north slope of Coprates Chasma, where it is not obscured by talus on the slope (Figure 4.11). Again, it appears to be 100 to 200 m thick, but seems to be about 200 m stratigraphically below the topmost strong layer.

On the chasma slope north of the west end of the massif, there is a 7.5 km diameter crater perched near the edge of the plateau and it is sectioned by the chasma (Figure 4.12). MOC image M02/03108, transects this crater (Figure 4.12c). Given the elevation of the topmost dark layer observed just to the east in M09/04413 (Figure 4.12d), we expect it to be in the bowl of the crater. Unfortunately, the lighting geometry of this image has part of that wall of the crater in a diffuse shadow, and careful searching does not obviously reveal the topmost layer in the crater wall (and yet it is seen to the east and west in images). The THEMIS visible image V06831002 (Figure 4.12b) also covers this area, and the topmost strong dark

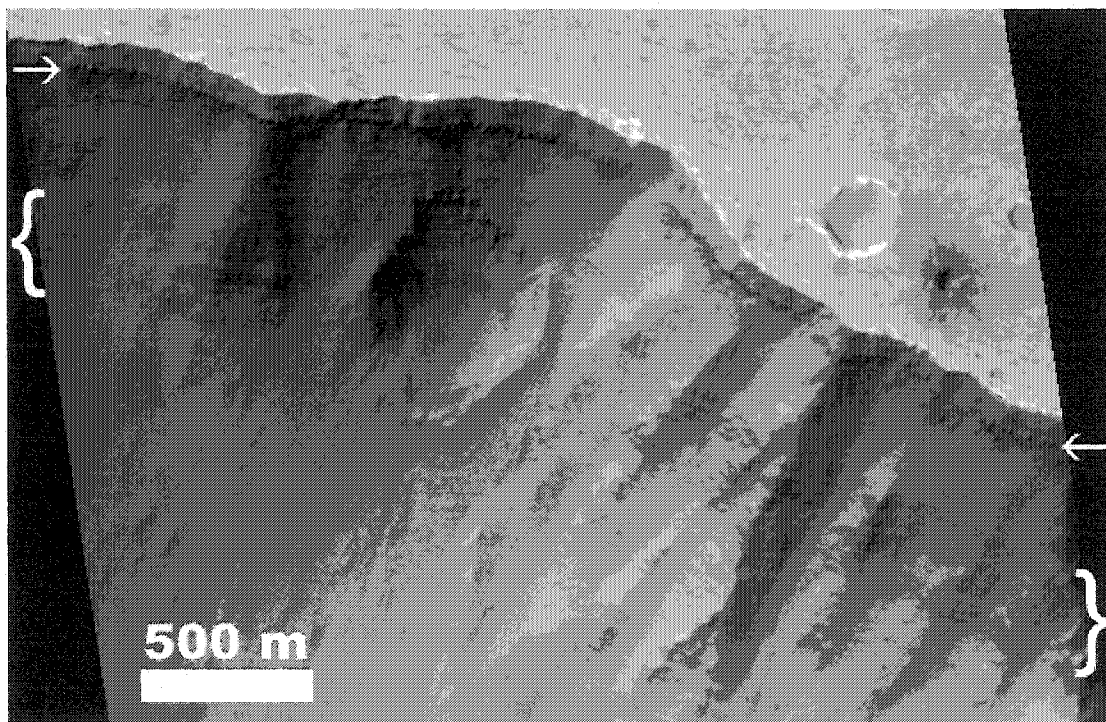


Figure 4.11: This is a portion of the MOC image E03/02145. The arrows indicate the location of the topmost strong layer which is just below the plateau surface. The brackets indicate a competent sequence of darker-toned layers.

layer can be made out below the chasma rim, but is difficult to trace within the bowl of this crater. It may be difficult to discern because the crater form is relatively stable against erosion. Therefore, the break in slope associated with the strong layer on more eroded slopes does not distinguish it here. Additionally, its albedo contrast may be obscured by dust that has built up within the bowl of the crater. However, a thin, bright layer can be seen in the nighttime THEMIS data (Figure 4.12a) in approximately the expected location.

In addition to the bright feature in the nighttime THEMIS image, there is also an interesting break in slope on the crater wall (arrows in Figure 4.12c). This break in slope is 75 m in elevation below the rim of the crater, but it is 130 m above the elevation of the topmost competent layer as observed in M09/04413 (Figure 4.12d). The rim of the crater is about 100 m above the surrounding plateau, if that is how much the stratigraphy here has been uplifted because of the impact, then this break in slope may indeed be the topmost competent layer uplifted by the impact.

4.4.3 Coprates Chasma, south of massif

The rim of Coprates Chasma directly south of the massif has a very different character from that directly to the north of the massif and the slopes of the massif itself. Schultz (1991) noted a structural difference between the north and south slopes of Coprates Chasma in general. However, the southern rim and slope of this easternmost section of Coprates Chasma may be different from the rest of Coprates Chasma for a number of reasons. The plateau beyond the south rim is just east of the Coprates Rise into which are carved the Nectaris Fossae further south. This broad anticline separates the higher Thaumasia Planum to the west from the lower-lying Noachis Terra to the south and east of Valles Marineris. Therefore the character of the greater plateau geography south of the rim here is fundamentally different than that further west towards Tharsis.

The differences between these slopes are highlighted by high-resolution images and topography. MOLA data indicate that the range of surface slopes is similar on the slopes of Coprates Chasma both north and south of the massif, as well as

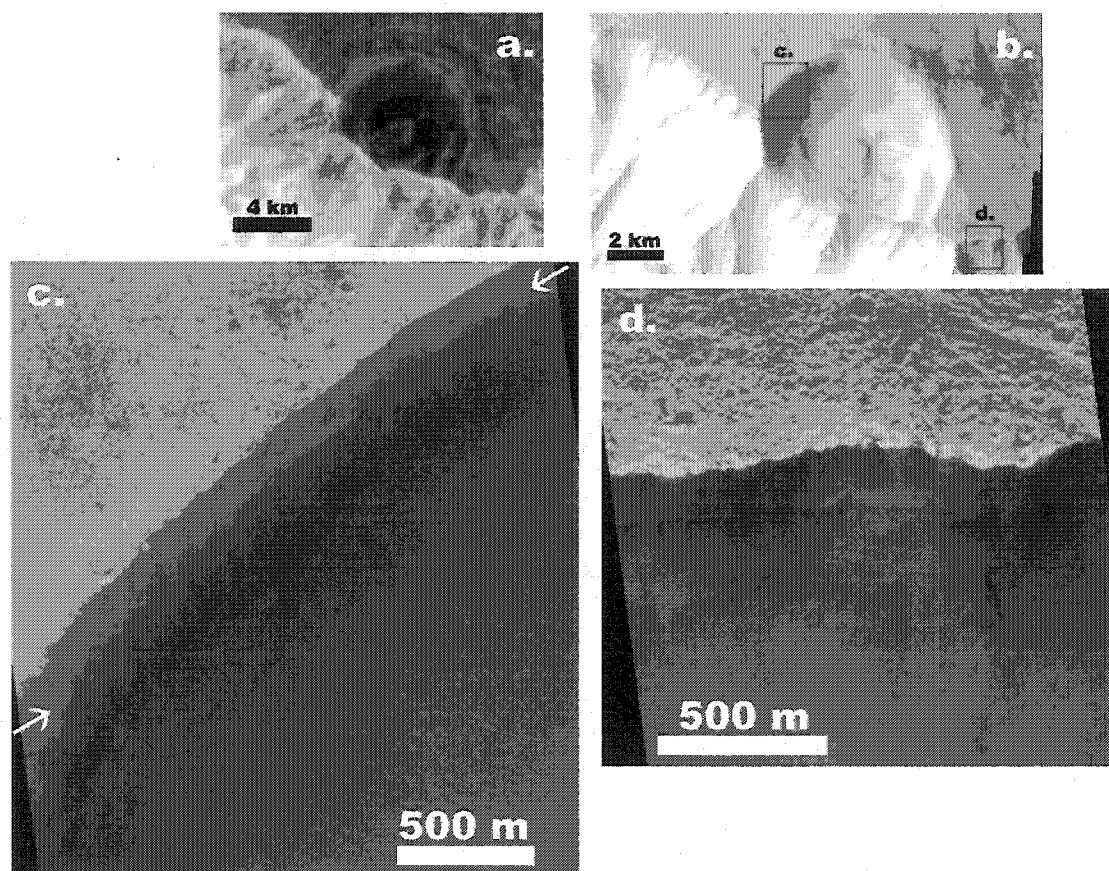


Figure 4.12: These images show how the topmost strong layer is interrupted by this crater, but is seen on either side of it on the chasma slope, and may be present within the bowl of the crater itself. *a.* Portion of THEMIS nighttime IR image I07486008. It shows that the bowl of the crater is dark and therefore has a lower temperature relative to the surrounding terrain. These temperatures may mean that there is more lower-thermal-inertia dust within the crater than outside. However, a bright layer can be seen within the bowl of the crater that could correspond to the topmost strong layer. *b.* Portion of THEMIS VIS image V06831002, the black boxes show the locations of *c* and *d*. *c.* Portion of MOC image M02/03108. Strong evidence of the topmost strong layer can not be seen within the bowl of this simple crater. However, there is a faint hint of a break in the slope of the crater 75 m in elevation below the rim height, the arrows indicate this slope break. This slope break may be the expression of the topmost layer in the crater. *d.* Portion of MOC image M09/04413. The topmost strong layer is evident here below a 100 m thickness of weaker materials.

on the massif itself (Figure 4.13). The strike of the chasma's rim to the south is more irregular and scalloped by large landslide alcoves than on the north side of the chasma in this region. Along the northern slope, the ridges in the spur-and-gully morphology have a roughly regular wavelength from 1.5 to 5 km. The south slope displays two characters: to the west, it is dominated by larger landslide alcoves, whose bounding spurs have a wavelength from 5.5 to 6.5 km; to the east, the slopes are not dominated by landslide alcoves, and show a more regular spur-and-gully morphology with a spur wavelength similar to that of the north slope. The eastern morphological pattern is either interrupted by the presence of the large, 40 km diameter crater that is partially eroded by the chasma, or this morphological pattern is only present to the east and west of this crater.

These gross differences in slope morphology are not the only differences between the east and west portions of the slope of Coprates Chasma south of the massif. The elevation of the plateau along the north rim of Coprates Chasma maintains a relatively constant elevation along the 230 km length of the massif. However, the plateau along the south rim varies from 600 m below the elevation of the north rim in the west to nearly the same elevation as the north rim in the east (Figure 4.2).

Although portions of the southern plateau edge have higher elevations than the summit of the massif, no evidence of the topmost dark competent layer can be seen along its length in high-resolution images. Here, the rim does not show cliff-forming layers although such sequences are observed further down-section (Figure 4.14).

M08/07133 (Figure 4.14b) is on the south rim above a slope section that displays spur wavelengths similar to the north rim, and it displays fine layering that does not form steep slopes, but is notable because there seems to be a 30 to 40 m thick layer of less resistant material which has retreated back 80 to 120 m from the edge. This kind of morphology is not seen in M04/02407 (Figure 4.14a) which is atop one of the larger landslide alcoves.

This morphology of a 10 to 50 m thick layer with an indurated top surface which has retreated from the plateau edge by 50 to 120 m is evident in MOC images of the south rim eastward of M08/07133, even on the floor of the 40 km eroded crater,

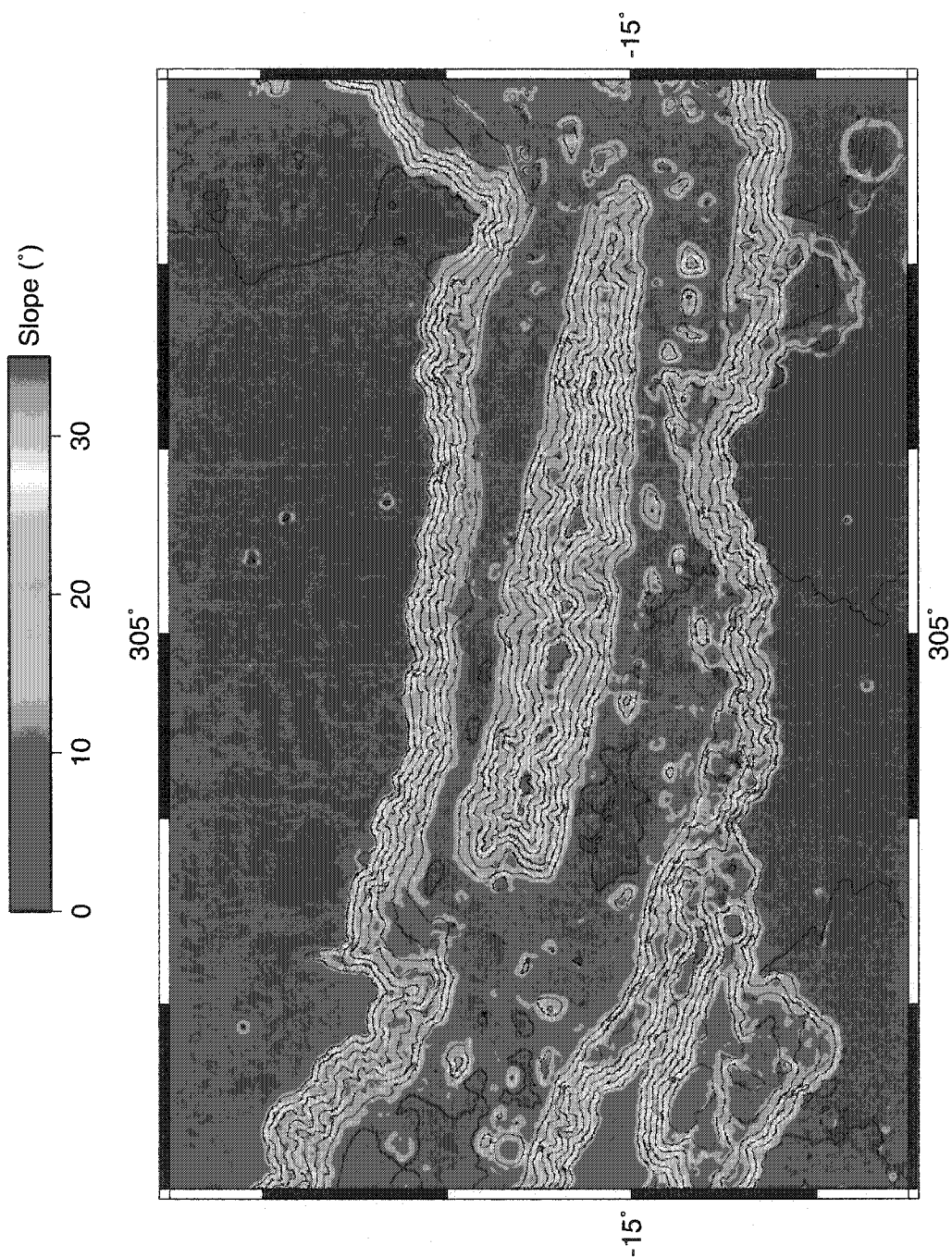


Figure 4.13: Slope map created from 1/128th degree gridded MOLA data. Slopes greater than 35° are white, 1000 m elevation contours.

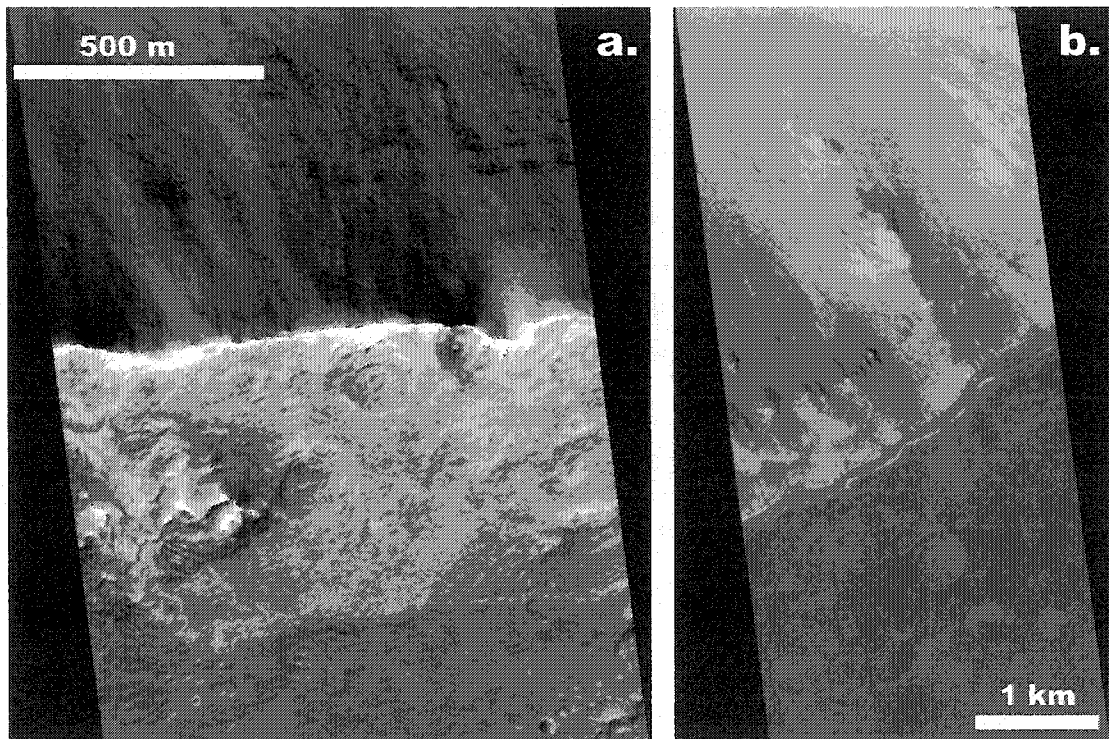


Figure 4.14: These image portions cover the the south rim of Coprates Chasma south of the massif. *a.* M04/02407. No topmost dark, strong layer evident, but the plateau surface seems indurated. *b.* M08/07133. This image shows that there is a layer that has has retreated back 80 to 120 m from the plateau edge. Based on MOLA elevation data, this layer is 30 to 40 m thick.

indicating that this material was put down after crater formation. There is also evidence that this material has been eroded away not only at slope edges but also from the relatively flat plateau in places.

The MOC coverage along the south rim is quite sparse, and so there may be an observational bias here, but there are only occasional outcrops of competent units below the plateau surface along the slopes, and we cannot correlate them to other outcrops along the south slope, or to those within the massif or north slope.

4.4.4 Coprates Chasma, west of massif

On the north rim, west of the area where the crater is sectioned by the chasma slope, there is a re-entrant that cuts northwards into Ophir Planum that is captured in the THEMIS image V03835003 (Figure 4.15). The afternoon sunlight illuminates the west-facing slope, and the dark layer is visible just below the cliff edge. West of that there is a promontory near 303° E, 13.5° S that juts south into the chasma (Figure 4.16). The top surface of this promontory shows east-west linear depressions, and a slight drop in elevation, leading Witbeck et al. (1991) to mark a normal fault in this area. MOC image E03/01374 (Figure 4.16c) shows a strong, competent layer that is probably the topmost layer. However, in this image instead of there being an even stack of material burying the strong layer, the material above the strong layer shows hills or hummocks from 500 m to 1 km in size. The elevation measurement of the topmost strong layer here is 2106 m, 167 m lower than the previous elevation measurement 45 km to the east. The MOLA elevations of the plateau surface show that the plateau surface out at the south edge of the promontory is about 150 m lower than the plateau surface north of the fault zone here. If the layer here was down-dropped that much, then that puts the pre-fault elevation of the layer back in line with the elevation that the topmost strong layer shows below the plateau edge north of the massif. Along the west side of that promontory, THEMIS image V06856002 (Figure 4.16a) shows that there is a dark linear feature on the sunlit facing slope that is just below the plateau's edge which is likely to be the continuation of the dark topmost layer.

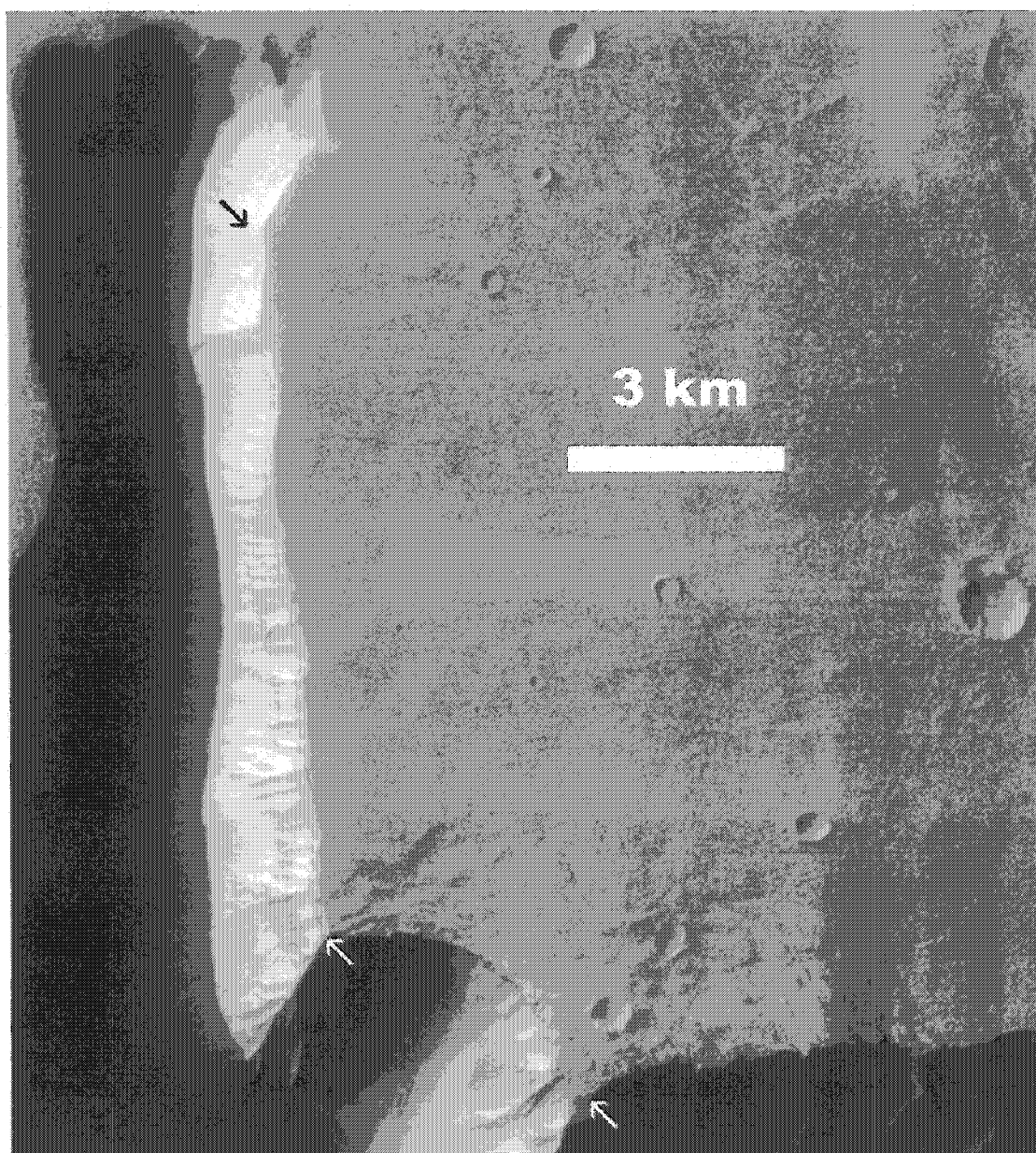


Figure 4.15: This is a portion of THEMIS VIS image V03835003. The context for this image is in Figure 4.16d. A small chasm that cuts north into the southern Ophir Planum surface to the northwest of the massif in Coprates Chasma can be seen. Although difficult to pick out, a dark layer can be seen in the sunlit eastern slope just below the cliff edge (indicated by arrows).

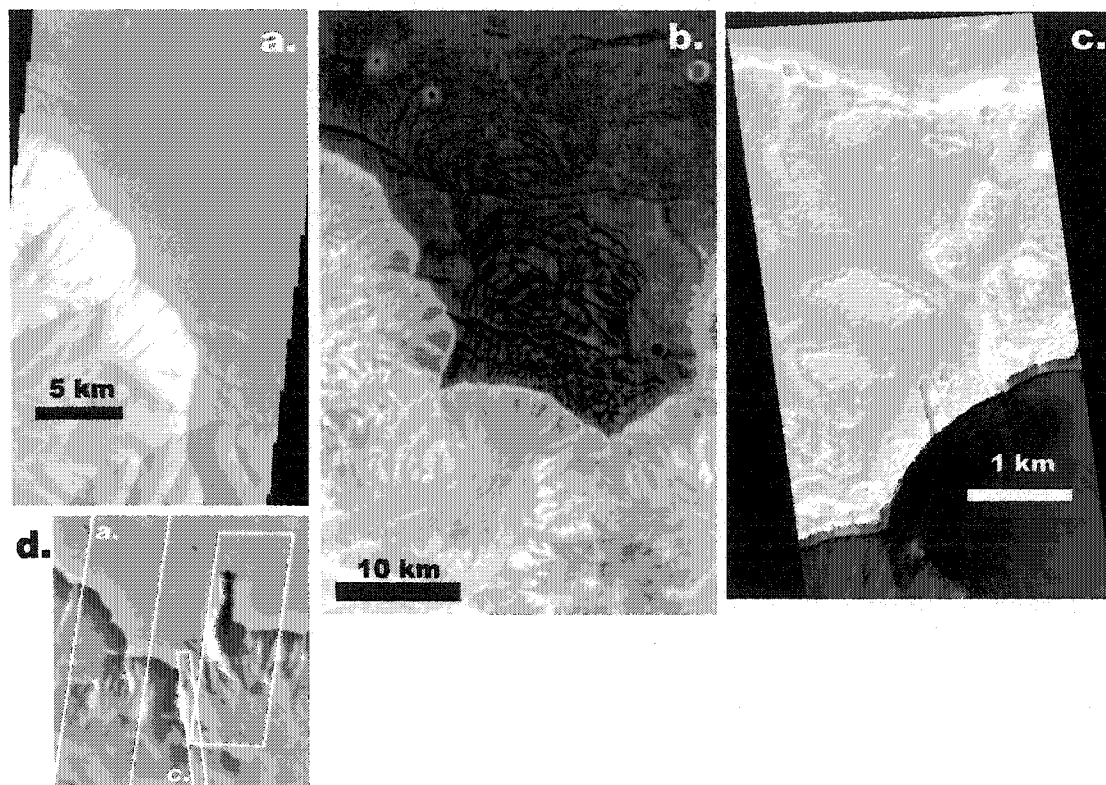


Figure 4.16: These images cover various parts of a promontory that juts out into Coprates Chasma just west of the massif. *a.* Portion of THEMIS VIS image V06856002. The topmost dark layer can be seen just below the plateau surface along the slopes to the west and along the south of this promontory. Additionally, the hummocky surface texture of the promontory can be seen here. *b.* Portion of THEMIS nighttime IR image I08235013. This image highlights the relative temperature differences at night between the hummocks and the lanes between them. *c.* Portion of MOC image E03/01374. This image shows the topmost strong layer that underlies the hummocky surface here. *d.* This MDIM2 context image shows the outlines of the whole images for *a.* and *c.*. The unlabeled outline is that of THEMIS VIS image V03835003 (Figure 4.15).

Outcrop Elevations West of Massif

MOC Image	MOLA Orbit	Elevation (m)	E Longitude	Latitude
E02/02151	19137	4075	291.02	-9.76
M12/02722	14359	4950	293.79	-10.95
M08/06016	12812	5140	296.32	-11.52
M10/03722	13642	5050	297.32	-11.75
E02/01171	19011	2787	301.60	-12.84

Table 4.2: These measurements are in order from west to east. They show the MOC image that the MOLA track was matched with to yield the elevation measurement of the competent layer that is present on the rim.

The next MOC image to the west is E02/01171 (Figure 4.17), and it also displays a resistant layer, but the material above it has retreated back from the edge by 100 to 200 m, and the MOLA data indicate that the thickness of that retreating layer is about 10 m. The elevation of the resistant layer is 2787 m, roughly 500 m above the elevations of the topmost resistant layer north of the massif. MOC images of the Coprates Chasma north rim further west continue to show what appears to be a resistant layer just below the plateau surface. If it is all the same layer, the elevation of that layer mimics the elevation of the plateau surface (as the layer is observed either at the elevation of the plateau surface or tens of meters below it) as it rises up above 5000 m elevation and then descends back down as Coprates Chasma meets Melas Chasma to the west (Figure 4.18, Table 4.2).

It is difficult to tell if these outcrops of resistant rocks that form a distinct break in slope between the plateau surfaces and the slopes are all part of the same topmost resistant strong layer observed north of the massif in eastern Coprates Chasma. The high-resolution coverage is sparse, which makes lateral continuity of the layers difficult to establish.

The south rim of Coprates Chasma west of the massif does not show evidence for the topmost strong layer. There are definite expressions of layering in the slopes, and the rim does appear to be a relatively sharp edge. However, the morphologic indicators of the topmost strong layer are not present.



Figure 4.17: This portion of the MOC image E02/01171 shows how the material that overlies the resistant layer (indicated by the arrow) has retreated back from that edge. The material has retreated 100 to 200 m from the edge, and MOLA data indicate it is ~ 10 m thick.

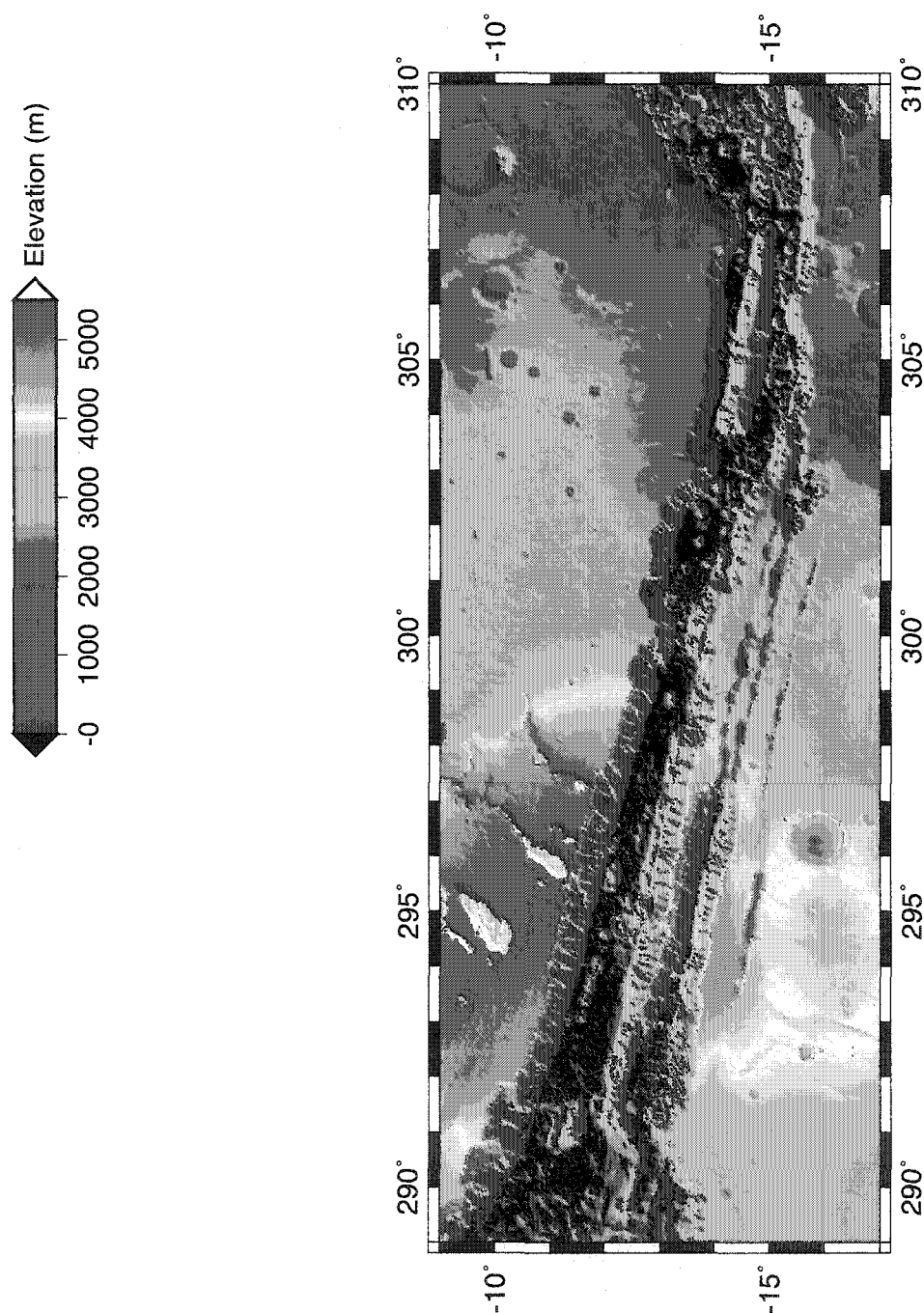


Figure 4.18: The 1/128th degree MOLA gridded data has been stretched to show a restricted elevation range to highlight the variability in the elevation of the plateau surface beyond the north rim of Coprates Chasma. Specifically, it shows that westward from the region where the massif is, the elevation rises to over 5000 m and then decreases again as it connects with Melas Chasma at the extreme western edge of this map.

Figure 4.19 shows the locations of outcrops of the topmost competent layer where we were able to positively identify it in MOC and THEMIS VIS images in eastern Coprates Chasma. These observations show that the terrain that forms the flat-topped areas along the spine of the massif is underlain by the same sequence of layers as the plateau at the north rim. Based on limited Viking data, Witbeck et al. (1991) mapped those areas as younger fractured material, when in fact it is the same ridged plains unit that makes up Ophir Planum (Figure 4.20).

4.4.5 Capri Chasma

Roughly where Witbeck et al. (1991) note the boundary between Ophir Planum and Aurorae Planum (Figure 4.20), there is a minor, but distinct drop in elevation between the two surfaces (Figure 4.2). There is also a change in morphology in the chasma rim along the Coprates and Capri edges. North of the massif in Coprates Chasma, that rim is marked by the presence of the topmost competent layer supporting a stack of presumably weaker overburden materials that form the edge of the plateau. East of this Ophir/Aurorae boundary, where the MOC images show a sharp edge, that rim appears to consist of a stack of resistant layers, rather than a distinct, single layer. The elevations of the top of this stack are consistently two to three hundred meters below the elevation of the topmost competent layer north of the massif in Coprates Chasma. The first example of this is in E05/02164 (Figure 4.21), which is on the slope just as Capri Chasma widens out from Coprates Chasma, east of the end of the massif.

There is a small chasma (Figure 4.22) that cuts into the side of Capri Chasma (Figure 4.23) near 308° E, 13° S. Image M02/03555 (Figure 4.24) shows the northern edge of this chasma cutting into the plateau surface which is lower here, about 1820 m. A unit of cliff-forming layers can be seen on the north side of the main chasma, and the corner where a short, shallow north-going depression intersects the main chasma. However, the expression of this unit disappears northward along the eastern side of that shallow depression, and the MOLA data coincident with this image do not afford us a good elevation estimate. Just slightly further east,



Figure 4.19: This figure shows the locations where the topmost strong layer outcrop can be seen in MOC and THEMIS VIS images. The dots indicate identification in MOC images, and the two lines indicate where the layer can be seen in THEMIS VIS images. Every MOC image that crosses the north rim of Coprates Chasma or the spine of the massif shows the topmost competent layer. No images that cross the south rim reveal any such layer. Note that all locations where the strong layer is observed along the north rim correspond to the ridged plains unit (Hr) identified by Witbeck et al. (1991) and in Figure 4.20. We argue that the outcrops on the massif indicate that the flat topped areas there should also be classified as the same ridged plains unit.

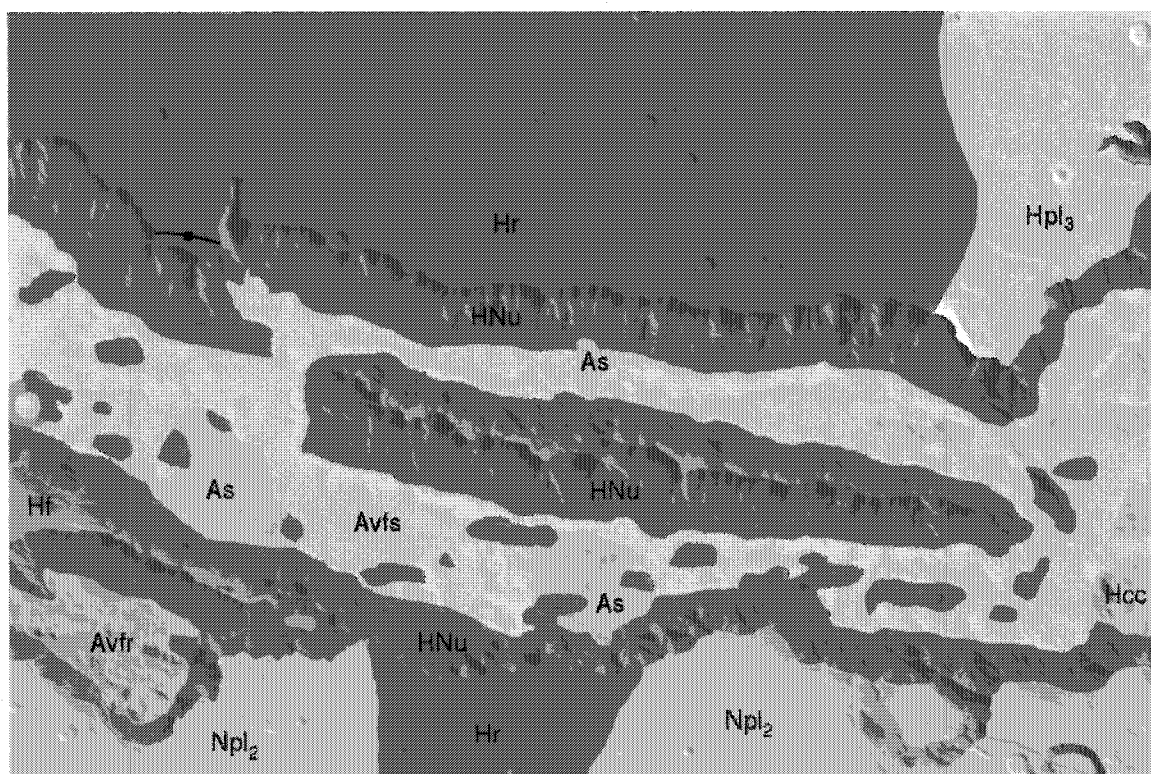


Figure 4.20: This geologic map is simplified from the Witbeck et al. (1991) map. The following units are defined on that map: As - Slide material, Hcc - Chasma chaotic material, Avfs - Smooth floor material, Avfr - Rough floor material, Hpl₃ - Smooth unit, Npl₂ - Subdued cratered unit, Hf - Younger fractured material, Hr - Ridged plains, HNu - Undivided material. The black line and circle denote a fault that was identified by Witbeck et al. (1991) and is discussed in this study.

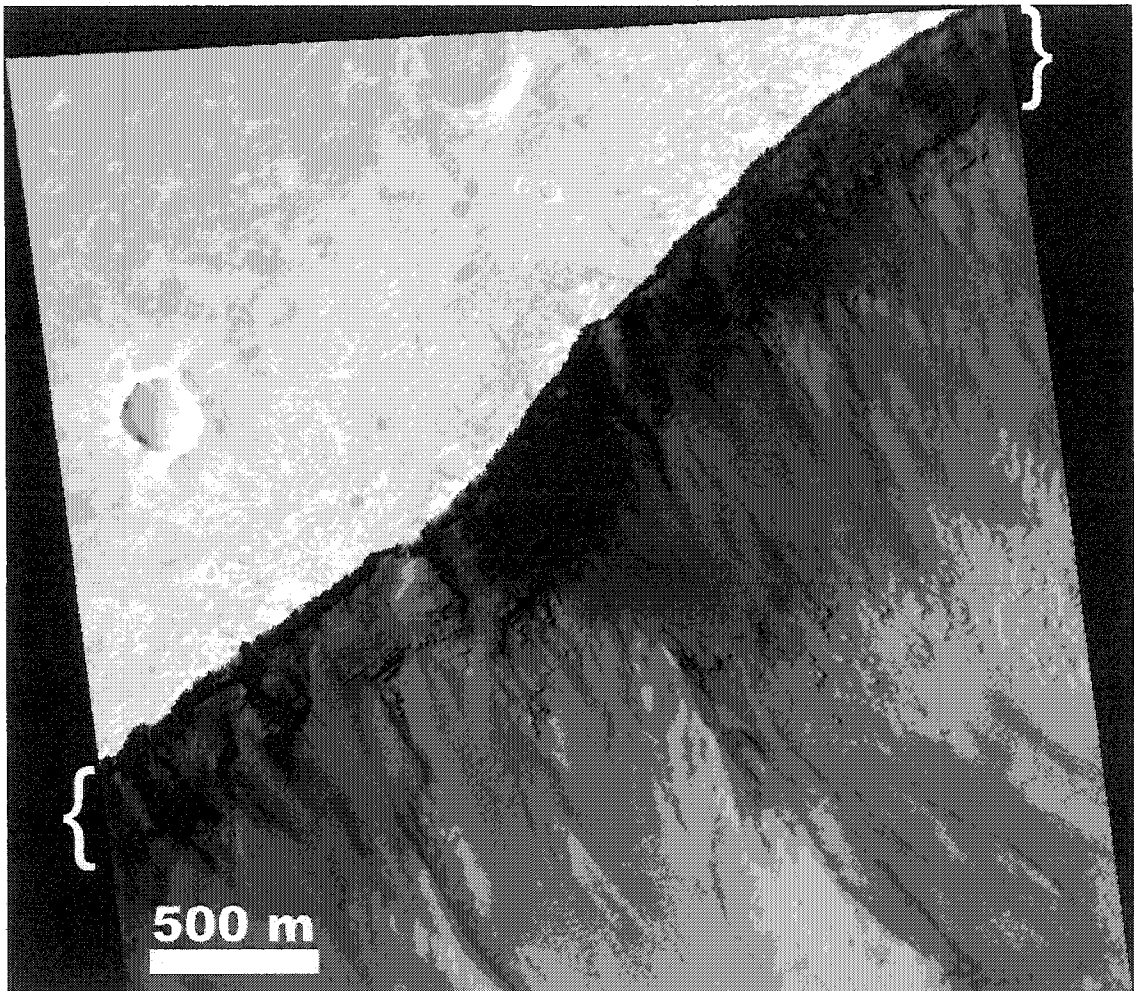


Figure 4.21: This portion of the MOC image E05/02164 shows that instead of a single, thin strong layer, there is a stack of resistant layers that underlie the the plateau here. This sequence is indicated with the brackets.

M09/04970 (Figure 4.25) also covers the northern slope of this little chasma. It also shows a competent unit near the cliff's edge around 1750 m elevation.

The short, shallow depression's depth appears to be limited by a resistant unit that outcrops from 1050 m to 700 m elevation. The morphology of the depression indicates that it was perhaps a channel formed by sapping into the massive layer down to the more resistant unit. Further northeast along the Capri Chasma rim, E09/02363 and M08/05759 show a stack of resistant layers that form the chasma rim, then a massive unit, and another resistant unit from 800 to 500 m elevation. M07/01362 (Figure 4.26) shows a strong cliff edge, and the dust cover on the plateau appears to have receded back here revealing a more rocky surface which appears to be the top of a layered stack 70 m thick, a massive section, and then resistant layering from 880 to 640 m elevation. Even further northeast, M11/01959 also displays a distinct resistant layered stack that forms the chasma rim which is also 70 m thick. This image also shows a massive section and then a resistant layered unit from 1040 to 840 m in elevation.

The expression of a ≥ 70 m thick unit of cliff-forming layers at the chasma rim followed by a massive unit or talus covering, and then a resistant unit of 200 to 300 m thickness is observed along a 250 km stretch of Capri Chasma. These observations indicate a relatively consistent stratigraphy over a large distance and may also be indicative of the stratigraphy that underlies the entire Aurorae Planum. The elevation of the top of that 70 m thick unit varies by 200 m along that distance, but is still relatively flat-lying. Similarly, the outcrops of the resistant layer within the slope vary, but are also relatively flat-lying.

4.4.6 Topmost Strong Layer Thickness and Extent

We were unable to make a direct measurement with MOLA data of the thickness of the topmost layer in Coprates Chasma. However, based on elevation and slope information from the various outcrop locations and plan form extents in narrow angle MOC images, we estimate that the thickness of the layer itself is about 10 m.

Our MOC and THEMIS VIS surveys of Coprates Chasma indicate that the

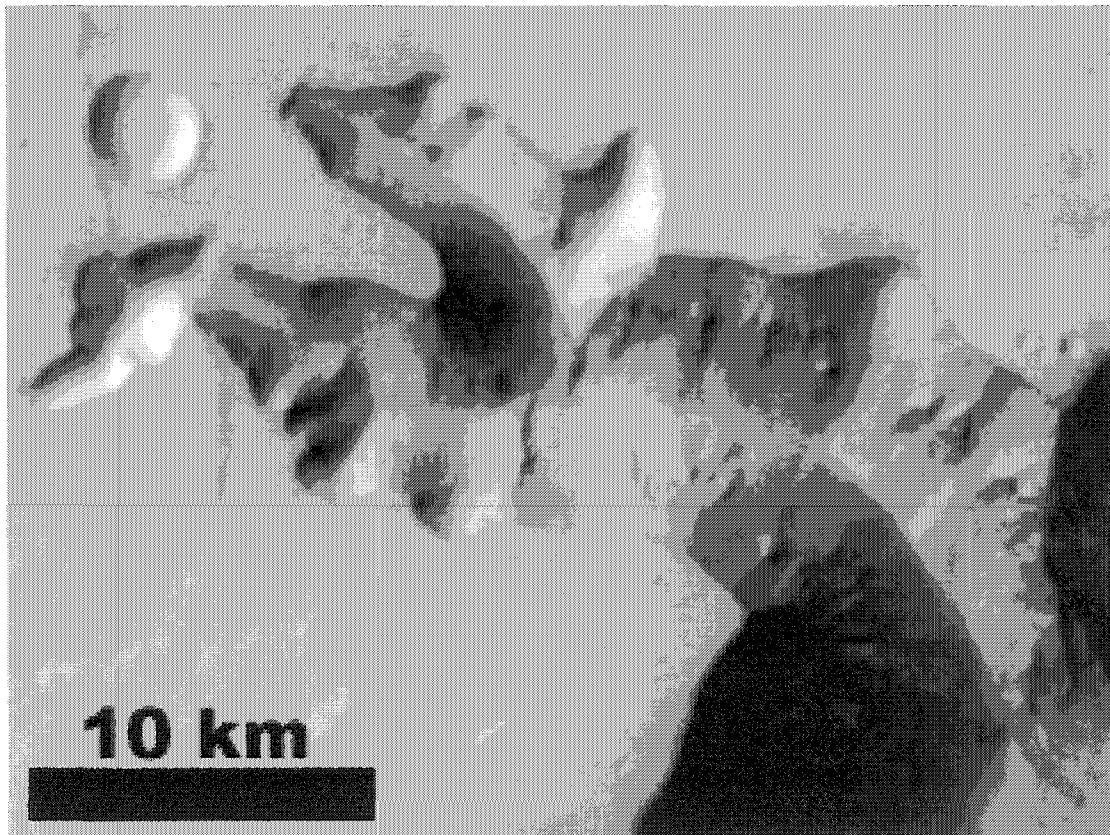


Figure 4.22: This is a portion of the daytime THEMIS IR image I01875001, which shows the small side chasma that cuts into the slope of Capri Chasma (Figure 4.23) near 308° E, 13° S.

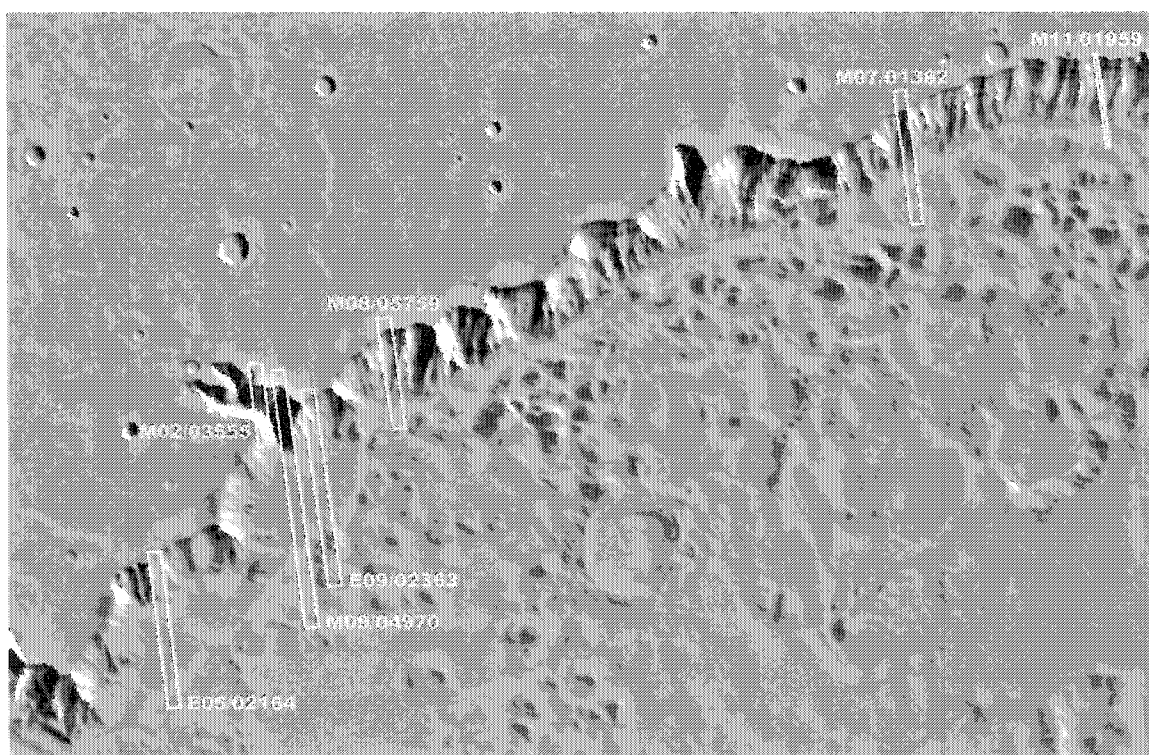


Figure 4.23: This Viking mosaic (MDIM2), shows the Capri Chasma slope and Aurorae Planum above it. The locations of MOC narrow-angle images that were used in this study are indicated by their outlines in yellow.

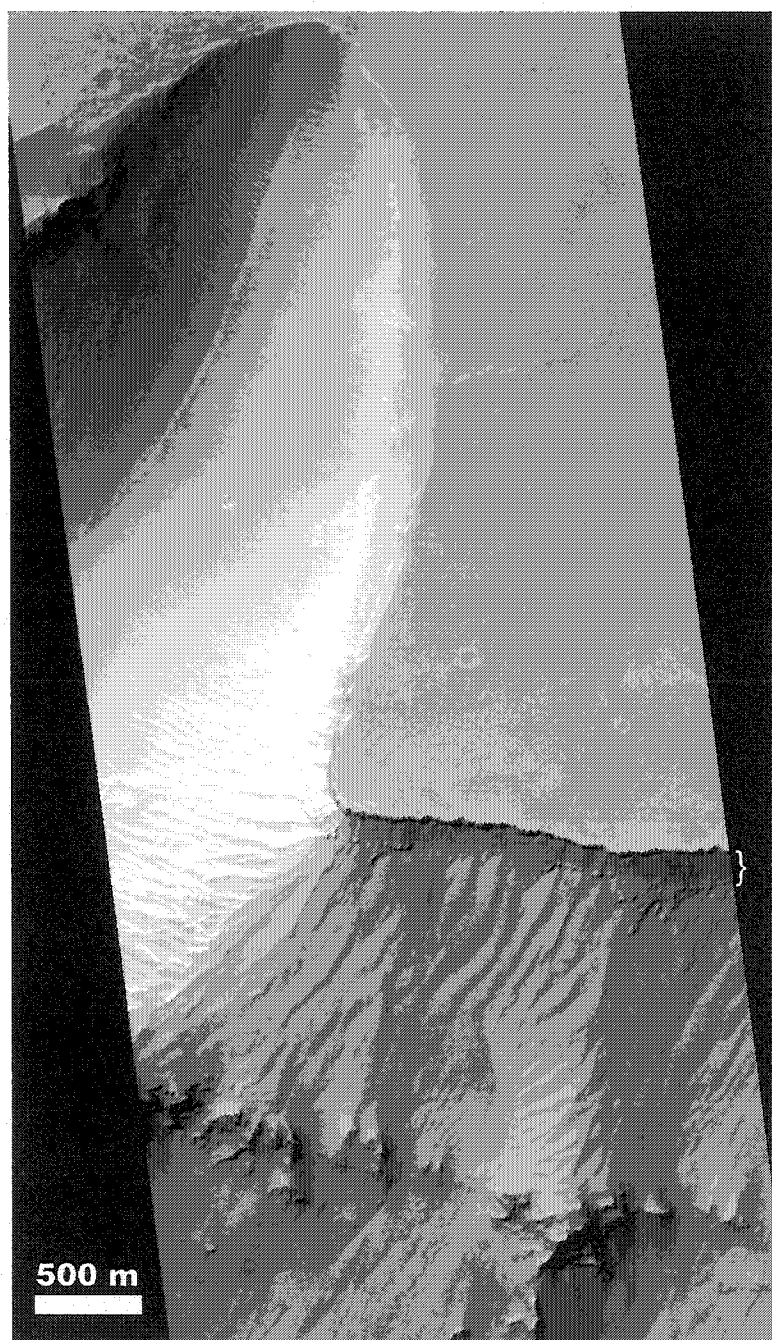


Figure 4.24: MOC image M02/03555 shows a side chasma from Capri Chasma and a shallow northward depression. A cliff-forming sequence can be seen along the north rim of the main chasma (indicated with the bracket), but it becomes less discernable along the shallow depression's east rim.

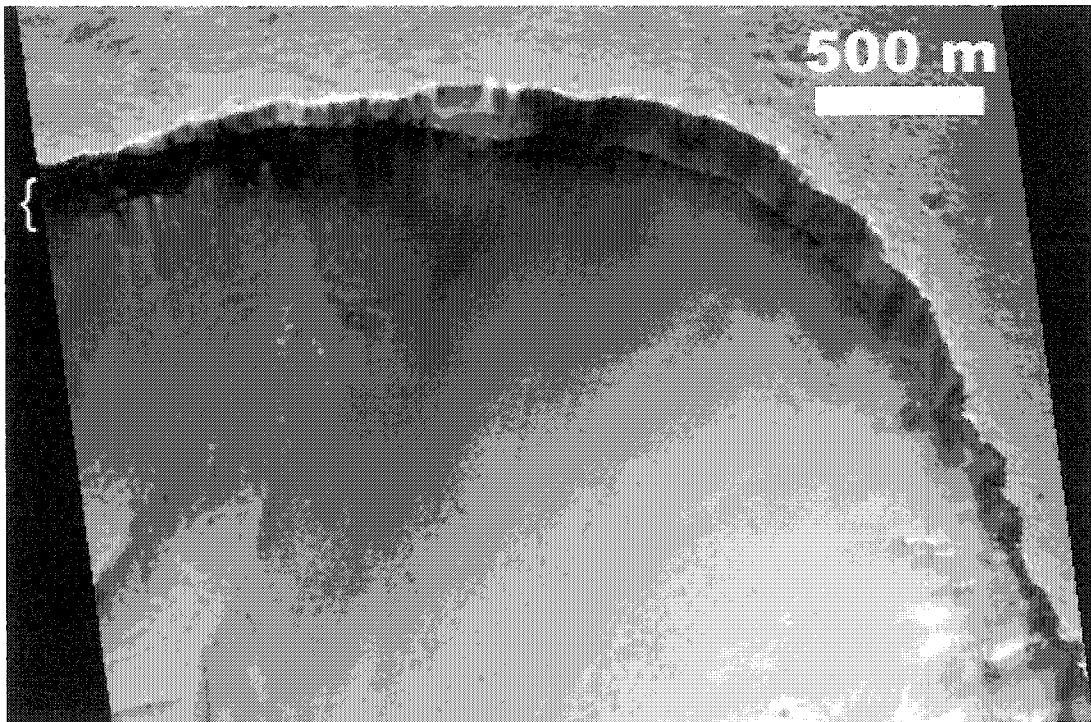


Figure 4.25: MOC image M09/04970 shows a side chasma from Capri Chasma (further east from Figure 4.24). A sequence of strong layers can be seen to outcrop below the plateau surface (indicated with the bracket). It is more difficult to make out in this image than in Figure 4.24 because of the resolution difference (that image has 2.84 m/pixel, this one has 5.67 m/pixel).

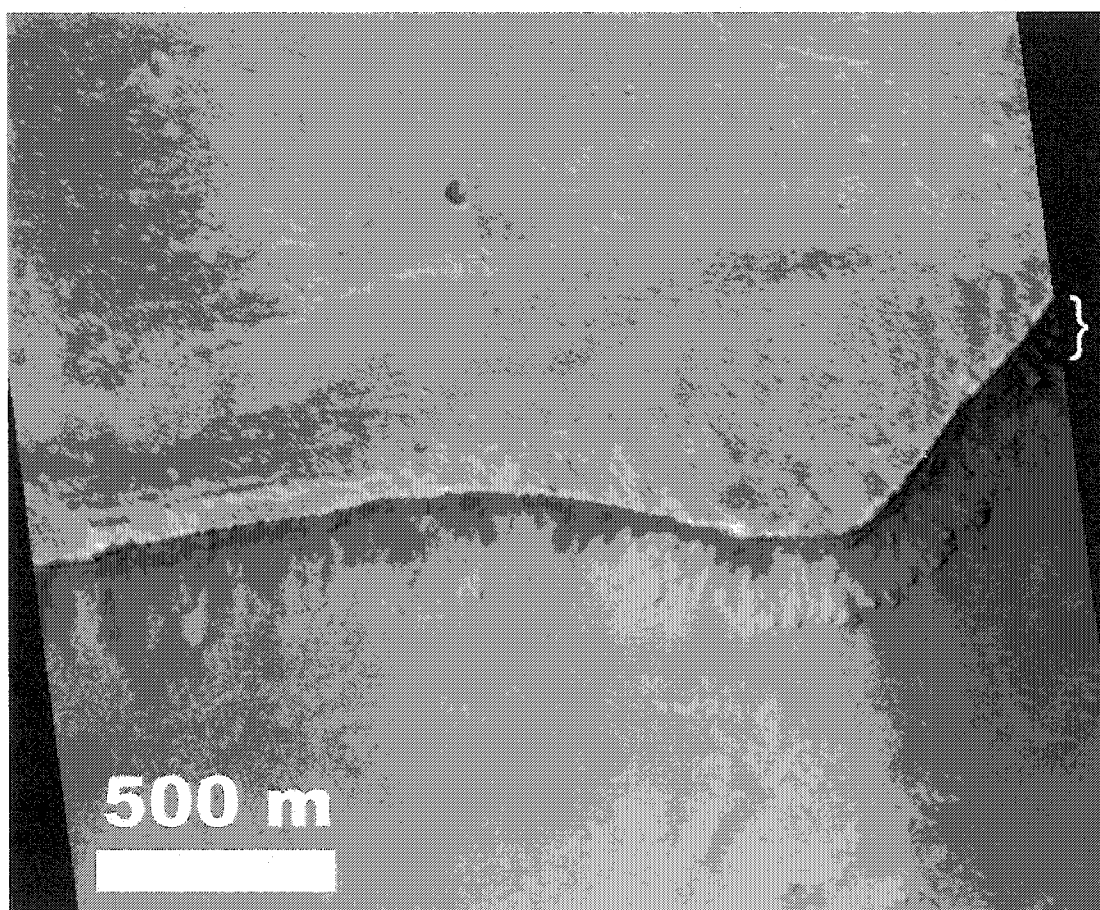


Figure 4.26: MOC image M07/01362 along the edge of Capri Chasma shows that the plateau's dust layer seems to have receded back from the cliff edge which shows the top surface of a resistant sequence of layered materials (indicated by the bracket), and there is a 70 m elevation difference between the top of the stack and the slope break on the chasma slope.

topmost competent dark layer seen in the massif is also positively identified in the slope of Coprates Chasma directly north of the massif (Figure 4.19). If we draw a simple polygon connecting these outcrops, we estimate a 8700 km² areal extent. This estimate doesn't take into account the unknown amount of north-south extension between the north slope and the massif. If we assume 60° fault surfaces, and that the floor of Coprates Chasma between the massif and the north wall was the plateau surface, we can estimate that extension around 7 km (the estimate rises to 8 km if the graben block is buried by a kilometer of fill). If we take this estimate of extension into account, then the area is only about 7000 km². However, both of these estimates assume that the layer terminates just inside the north wall, and doesn't account for how extensive the layer might have been before erosion of the chasma. Due to this uncertainty, the true areal extent of this layer is likely to be greater than the above quoted values.

4.5 Discussion

We hypothesize that the stratigraphy exposed along the north rim of this section of eastern Coprates Chasma, along the edges of the massif, and along the rim of Capri Chasma are all a part of the same extensive stratigraphic stack present in this region. At many locations we observe a single, approximately 10 m thick, dark-toned, competent layer that appears to act as a resistant cap just below the break in slope between plateau surfaces and chasma slopes (Table 4.1, Figure 4.19). Below that layer, there are a few hundred meters of lighter-toned, finely layered material that appears less competent. Below that we see a sequence of darker-toned competent layers, on the order of a hundred meters thick. Since this pattern is seen along the north rim of eastern Coprates Chasma, along the edge of the flat-topped areas of the massif, and to a lesser extent along the rim of Capri Chasma, we think that we are observing different portions of an extensive set of layers.

Given the dark tone and relatively high strength of the occasional competent layers, we think that their most likely composition is that of a relatively dense basalt.

The topmost competent layer exhibits a morphology and extent that is comparable to terrestrial flood basalts and inflated sheet flows (e.g. Keszthelyi and Self, 1998; Thordarson and Self, 1998; Keszthelyi et al., 2000). The presence of flood lavas on Mars has been suspected for some time (e.g. Greeley and Spudis, 1981; Mouginis-Mark et al., 1992; McEwen et al., 1999; Keszthelyi et al., 2000), and suggested recently by Ori and Karna (2003). The other competent layers further down the stack are more difficult to characterize, and may be sequences of thin flows interbedded with tephra or other sediments. A basaltic composition for Valles Marineris in general is indicated by Phobos ISM (Murchie et al., 2000), TES (Bandfield et al., 2000), and THEMIS (Christensen et al., 2003b) measurements although specific layers are not resolved. Given the footprint sizes of these instruments (22 km/pixel for Phobos ISM, 3×9 km pixels for TES, and 100 m/pixel for THEMIS), they are probably sampling the intervening weak layers and talus to a large extent, although the strong layers could have stronger absorption bands, dominating the signal. The relatively weak layers (either volcanic tephra or sediments derived from competent volcanic material) are probably not thick competent lava flows, but could have a basaltic composition. It is expected that there is a much greater ratio of tephra to lava on Mars than on Earth (Wilson and Head, 1994). However, given the overall strength of the slopes (Schultz, 2002), the intervening relatively weak sequences are probably lithified, but not as strong as the thin dark-toned sequences.

4.5.1 Tectonic Implications

In order to interpret our measurements of the topmost strong layer, we must make some assumptions about its original position. The topmost strong layer was either emplaced horizontally and subsequently altered by tectonic forces into the exposures that we measure today, or it was emplaced over an undulatory pre-existing surface, and the elevations where we observe it are the original locations of these outcrops, or a combination of these two. Based on the data that are available to us, we cannot truly determine which of these scenarios occurred, but there is some evidence that leads us to think that the layer was emplaced horizontally (for the most part), and

the offsets observed within the massif are due to tectonic activity.

The slopes measured between the outcrops within the massif (q.v. §4.4.1) and the north rim (q.v. §4.4.2) are all quite low, the largest being 3.65° dipping down to the south within the massif. Keszthelyi and Self (1998) indicate that long lava flows on the Earth can occur on slopes up to about 5° , and that the effect of reduced gravity would allow long lava flows on steeper slopes. So these slopes on their own, do not suggest tectonic movement. However, it is notable that the layer observed in the north rim is significantly more flat-lying than the layer in the massif (Figure 4.8). If we attempt to project the plane of the layer in the massif both to the north and south we can use the two extremes of north-south dip angle to determine where the layer should outcrop on the north and south rims. We begin with the almost zero north-south dip observed at the western end of the massif which would put the topmost strong layer 370 m below where it is observed to outcrop on the north rim. At this elevation there is no evidence of a singular strong layer on the north slope. Similarly, if the layer is projected south, it ends up above the plateau surface. This estimate might be consistent since we do not observe the competent layer on the south rim here, so perhaps it has been removed. However, we do expect it to resist erosion, so this presents a quandry. If we take the more extreme dip of 3.65° at the eastern end of the massif measurements, and project the layer southwards, it should outcrop at -1700 m elevation, but no evidence of it is seen there. If we project it northwards, it should outcrop 4 km above the plateau surface, and yet it is seen less than 100 m below that surface. This information by itself does not rule out the possibility that the topmost layer was emplaced on an undulatory surface with a variety of local surface slopes.

However, in all locations where the next most competent sequence is observed (q.v. §4.4.1), it has a consistent elevation difference with the topmost strong layer. Again, this by itself might only argue that the next most competent sequence was also laid down on an undulatory surface, making its surface undulatory, and the overlying strata (topmost strong layer included) simply conformed to this surface.

However, all of these data together, combined with the observation of the down-

dropped block in the massif and the promontory to the west, that is down-dropped by an amount similar to the elevation offset between the topmost strong layer outcrops in the massif and the north rim, lead us to the conclusion that the topmost strong layer was emplaced mostly horizontally. Therefore, the variety of elevations at which the topmost strong layer is observed are the result of tectonic movements, not just original emplacement at a variety of elevations. Additionally, this supports the theory that eastern Coprates Chasma underwent some north-south extensional motion and subsidence (Schultz, 1991, 1997, 1998; Lucchitta et al., 1992; Peulvast et al., 2001) and the massif here is a horst block. In addition to this large scale horst and graben structure, the down-dropped block on the largest flat-topped area near the western end of the massif indicates that extensional forces were acting on smaller scales within the massif as well. This portion of Coprates Chasma displays a kind of blunt-canyon morphology in the rim to the northwest of the massif, and there is a short north-south oriented re-entrant cut into the slope there (Figure 4.15). That might be the remnant of a cross-fault (Wilkins and Schultz, 2003) that demarcated the western extent of the massif block.

According to our measurements, the massif block subsided on the order of a hundred meters (over 350 m at the west end and 150 m at the east end), and it must have tilted down slightly to the west either during chasma formation or in the time since. Similarly, since we get two different measures of the north-south dip of the topmost strong layer in the massif, there must also be faults within the massif that are responsible for the dip angle difference and allowed for a twisting motion within the massif. Additionally, the promontory to the west indicates subsidence on the south side of the graben identified by Witbeck et al. (1991) of about 150 m as well.

While the dip angles in the massif layer display a greater tilt than the relatively flat-lying layer in the north slope, the measurements of the topmost layer outcrops there display a faint dip down towards the west. These measurements are consistent with the gradient of 0.03° found by Smith et al. (1999b) in the floor of Coprates Chasma east of about 300° E longitude. This similarity indicates that the gradient

of the chasma floor may not be independent of the chasma slope rock strata in this region.

A qualitative observation can be made that the rim of Coprates Chasma directly north of the massif has a mostly straight strike, however further westwards, the northern slope of Coprates Chasma contains more arcuate landslide alcoves, as do portions of the slope south of the massif. We hypothesize that these occasional strong layers are contributing to this morphology. These sequences of more resistant rock may be acting to provide structural support, and therefore their presence or absence is an important factor in the overall morphology of the slope. Thickness of individual resistant sequences, vertical density of such sequences, and even fault patterns within those sequences may be governing whether a particular stretch of chasma rim has a mostly straight strike with small spur-and-gully morphology or whether the rim is susceptible to large landslides. As slopes are eroded, the presence of resistant layers will cause locally steepened slopes below them, making these areas more susceptible to catastrophic failure, perhaps triggered by a seismic event (Schultz, 2002).

4.5.2 Boulders and Blocks

Malin and Edgett (2001) note that there are few boulders observed at the bases of the slopes within Valles Marineris. They infer that particles derived from wall materials do not have sufficient strength to maintain large sizes during their descent to the base of the slope. Malin and Edgett (2000) indicate that where steep scarps occur in obviously volcanic terrain, boulders are often seen downslope.

In order to gain an understanding of the competency and strength of eroding units, we surveyed all MOC images with resolutions better than 4 m/pixel in the Eastern Coprates Chasma region to look for boulders and blocks. Most of these images had resolutions of 1.41 m/pixel or 2.82 m/pixel, with a few of 2.98 m/pixel. Objects must be at least two pixels in diameter to be observed under the best conditions. Objects would have to be many more pixels in diameter if the photometric conditions were less than perfect, or if the objects were largely buried. Given these

size parameters we are looking for objects that fall into the very coarse boulder to coarse block categories of Blair and McPherson (1999). However, in order to make our grammar less cumbersome we will sacrifice specificity and refer to these particles generically as blocks.

We observed blocks in some images, at a host of different elevations on the slopes, but none on the flat floor of Coprates Chasma or near the base of the slopes. In all cases where we did observe blocks, it was clear that these blocks had been shed from strong layers immediately upslope of their locations (Figure 4.27). We conclude that the strong layers here produce blocks of similar sizes seen elsewhere on Mars, but that they do not survive transport over more than about 1 km.

Perhaps as the strong layers within the slope are broken up by the landslide process, the resultant particles either ride the surface of the landslide or are displaced upward from within. Either way, the blocks would suffer less damage than they would otherwise experience if they were to roll and fall down the entire slope (as suggested by Malin and Edgett, 2001). This scenario would explain why boulders and blocks are seen on landslide deposits on the Valles Marineris floor (Malin and Edgett, 2001), but not on the floor materials in general.

4.5.3 Wrinkle Ridges and Topmost Strong Layer Extent

Wrinkle ridges are observed on Ophir Planum (Watters, 1991, 1993; Zuber and Aist, 1990; Mueller and Golombek, 2004), and the recent quantitative model by Schultz (2000) indicates that wrinkle ridges are formed when a blind thrust fault occurs below layers which are capable of bedding plane slip, have large strength contrasts, or both. This stratigraphic situation is exactly what we observe along the north rim of Coprates Chasma. In fact, the topmost competent layer is only observed where the ridged plains unit is cut by slopes (Figures 4.19 and 4.20). If blind thrust faults occur at depth below the planum surface, then bedding plane slip might occur between the layers of different strength that we observe in the stratigraphic stack here. This slip could result in those layers forming a wrinkle ridge in the plateau surface material, as is observed across Ophir Planum. The observation of wrinkle

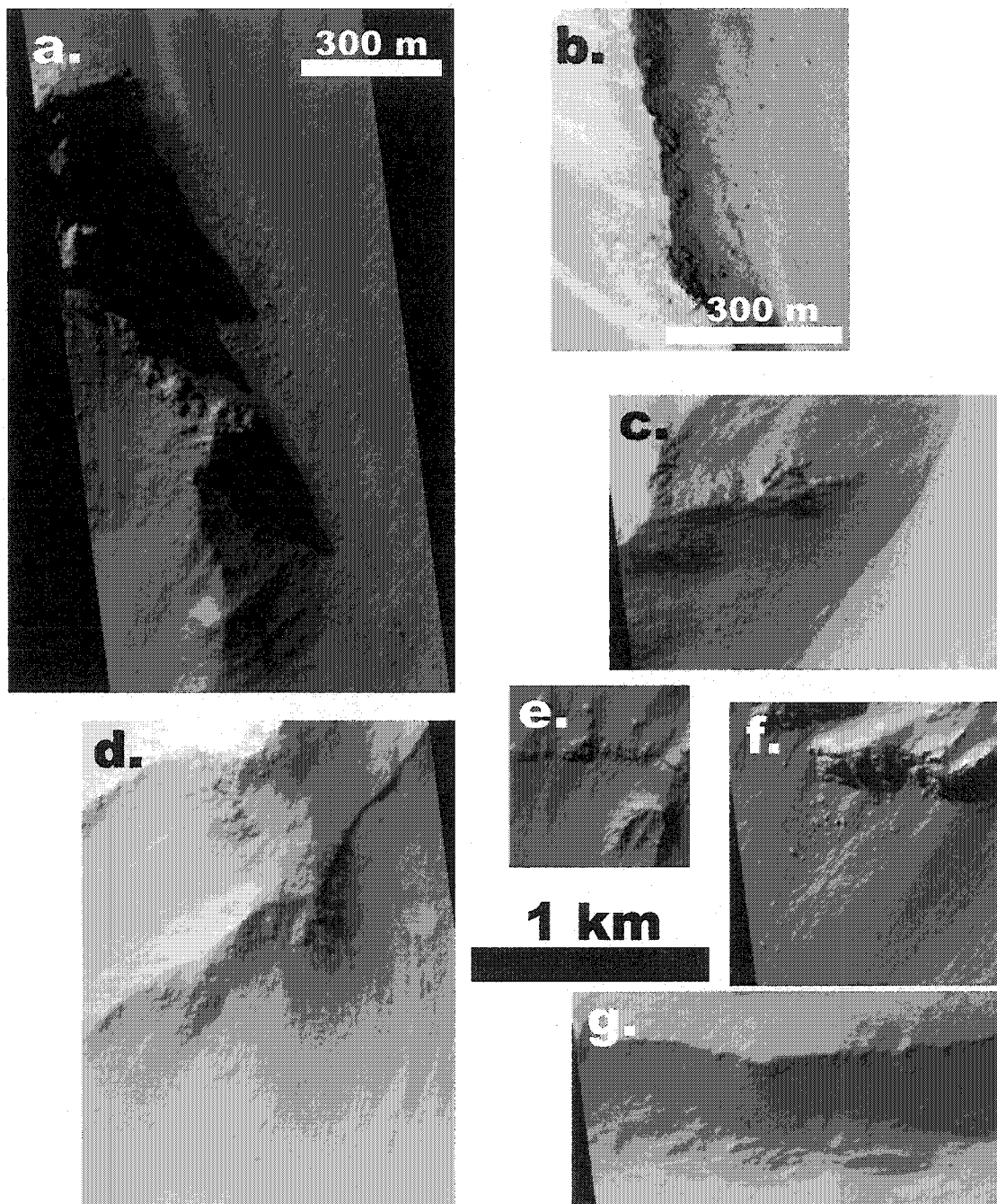


Figure 4.27: These MOC images show boulders and blocks on the slopes of Coprates Chasma. *a.* Portion of MOC image M00/02438. *b.* Portion of MOC image M07/00865. *c.*, *d.*, & *e.* Portions of MOC image E01/02131. *f.* Portion of MOC image M21/01517. *g.* Portion of MOC image M00/02870. Figures c through g share the same 1 km scale bar.

ridges on Ophir Planum may be an indication that there is a uniformity of strata that underlies Ophir Planum, and more specifically we hypothesize that the topmost strong layer may underlie Ophir Planum.

If this hypothesis is true, then the interpretation of the competent layers observed on the north rim of Coprates Chasma further west of the massif as belonging to the topmost competent layer is strengthened (Figure 4.28) since wrinkle ridges and the ridged plains unit extend westwards. However, whether it underlies the smooth unit (Hpl₃) and the younger fractured material (Hf) (Witbeck et al., 1991) of Ophir Planum west of 298° E is unknown. Schultz (1991) suggests that the ridged plains may underlie this area, with the wrinkle ridges buried beneath several hundred meters of material, but it is clear that he thinks it unlikely. Our limited observations of the rim in this area indicate that unlike the topmost resistant layer seen near the massif, there is almost no indication of weaker material above the edge. It is possible that the same unit underlies both terrains, and that different tectonic forces, or different stratigraphies at depth are affecting its surface expression in different ways.

If the topmost strong layer is an extensive and continuous lava flow, there are only two ways for it to achieve the anticlinal shape indicated by the MOLA data (Figure 4.18). One way is for the source vent for this sheet to be somewhere on the local elevation maxima, in which case this last volcanic flow would have occurred after the broad topography formed. Alternately, this sheet could have been emplaced mostly horizontally prior to crustal flexure in this area (Banerdt et al., 1992; Schultz and Tanaka, 1994; Mège and Masson, 1996), and then folded into an anticline. However this theory is speculative, as we cannot determine if the resistant layer observed in western Coprates Chasma along the north rim is the same topmost strong layer observed near the massif in the east. A greater amount of high-resolution coverage would be required along the chasma rim to make this correlation.

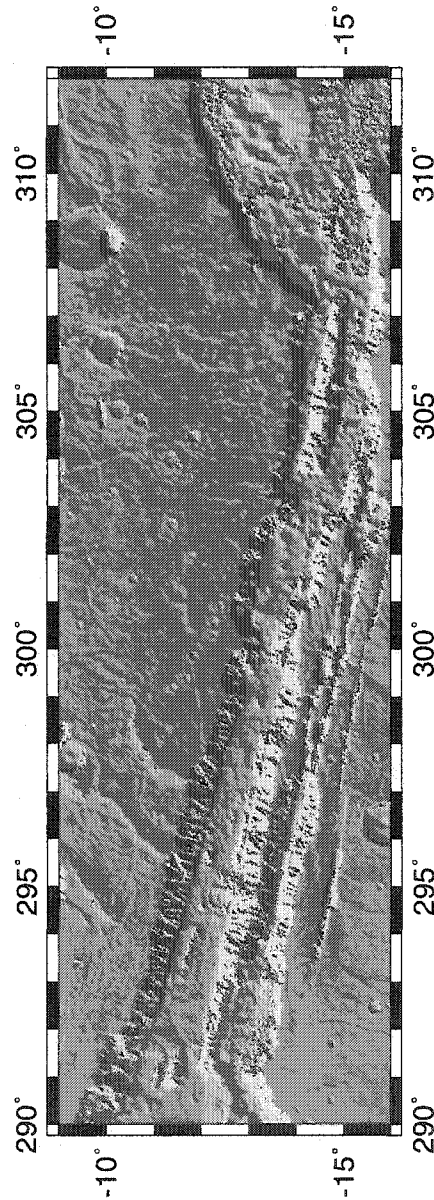


Figure 4.28: This regional 1/128th degree MOLA shaded relief map shows the locations where MOC and MOLA data have been aligned to provide various outcrop elevations. The green marks are identical to those in Figure 4.19 and show the locations where the topmost strong layer has been positively identified in the region near the massif. The blue dots indicate those locations noted in Table 4.2 where a resistant layer is observed, but it is uncertain as to whether it is the same dark, competent layer noted by the green marks. The red dots indicate the locations of the approximately 70 m thick unit of resistant layers that cap the Capri Chasma edge.

4.5.4 Depositional Implications

When we couple our conservative areal estimate of the topmost strong layer (7000 km^2) with our estimated 10 m thickness, we get a volume estimate of 70 km^3 . If the material is a single lava flow, then this minimum volume of lava is similar to the smaller volume flood lava flow fields within the Columbia River Basalts on Earth (e.g. Tolan et al., 1989; Reidel et al., 1989; Keszthelyi and Self, 1998). For example, the Roza flow is 1300 km^3 (Keszthelyi and Self, 1998).

That value is also within the range of lava flows measured on Mars. Cattermole (1990) measured flows on the Alba Patera volcano ranging from 0.6 km^3 , for flows within the caldera and near the summit, to 5484 km^3 , for flank flows. Similarly Lopes and Kilburn (1990) measured flows on Alba Patera and found individual flow volumes from 1.6 to 2310 km^3 . Mouginis-Mark and Tatsumura Yoshioka (1998) measured flows on Elysium Planitia that were nominally in the range from 17.7 to 68.1 km^3 , and estimated one up to 246 km^3 . Additionally in the Athabasca Valles region, Lanagan and McEwen (2004) have measured an individual flow at 1800 km^3 .

If we assume that this topmost strong layer underlies a sizable portion of the Witbeck et al. (1991) ridged plains (Hr) unit in Ophir Planum, then the volume estimate rises to over 2100 km^3 . Although it is a large volume, it is still near the largest volume for a single terrestrial flood lava flow (Tolan et al., 1989; Reidel et al., 1989; Keszthelyi and Self, 1998), and still within reasonable values for measured martian flows.

The hypothesis that the topmost strong layer underlies, and is in fact partially responsible for the ridged plains of Ophir Planum has implications for the boundary between Ophir Planum and Aurorae Planum. As we mentioned above, there is not only a morphological change across this boundary as noted by Witbeck et al. (1991), but there is also a subtle elevation drop of a few hundred meters from Ophir to Aurorae. Finally, the topmost strong layer is not observed at the Capri Chasma rim. We hypothesize that the boundary between Ophir and Aurorae Plana is the easternmost extent of the volcanic layer that we have been indentifying as the

topmost strong layer which crops out in Coprates Chasma. The stack of resistant layers that marks the Capri Chasma rim may be the next sequence of resistant layers that is observed stratigraphically below the topmost strong layer in eastern Coprates Chasma in both massif and north rim outcrops (e.g. Figure 4.29). The difference in elevation between Ophir Planum and Aurorae Planum could be because the topmost strong layer is not present, and the less resistant material observed between the topmost layer and the next resistant sequence has been eroded away (or was never there), such that the top of that resistant sequence forms the basement for the Aurorae Planum surface. As observed along both Coprates and Capri Chasmata the topmost resistant layer is often covered with a mantle up to 100 m thick. This mantling material covers the surfaces of both Ophir and Aurorae Planum, smoothing the surficial transition between the two.

If we assume that the minimally 70 m thick unit that sits at the Capri Chasma rim at least underlies the Witbeck et al. (1991) smooth material (Hpl₃) unit (Figure 4.20) of Aurorae Planum, its volume would be at least 4000 km³, more than that if it also underlies some portion of Ophir Planum. However, this unit is not a single lava flow, but many individual flows (we estimate each about 10 m thick) layered on top of one another.

The south rim of Coprates Chasma shows no evidence for the topmost strong layer seen on the north rim and in the massif. Its absence may be partially responsible for the varying elevation of the south rim in this area. Erosional processes could act on the less resistant materials exposed here that are capped to the north by the topmost strong layer. The massif retains its flat-topped plateau remnants because that topmost strong layer and to a lesser extent the next resistant unit below it have been capping the massif against erosion, and strengthening it against mass wasting.

The topmost strong layer isn't observed along the south rim of Coprates Chasma. Additionally, the next most competent unit seen in the massif and the north rim are not identified here (possibly because its morphologic indicators are either buried by talus). Why those sequences are not present in the south rim is unknown, but here are three hypotheses: 1) Perhaps the lava flow simply did not get that far during

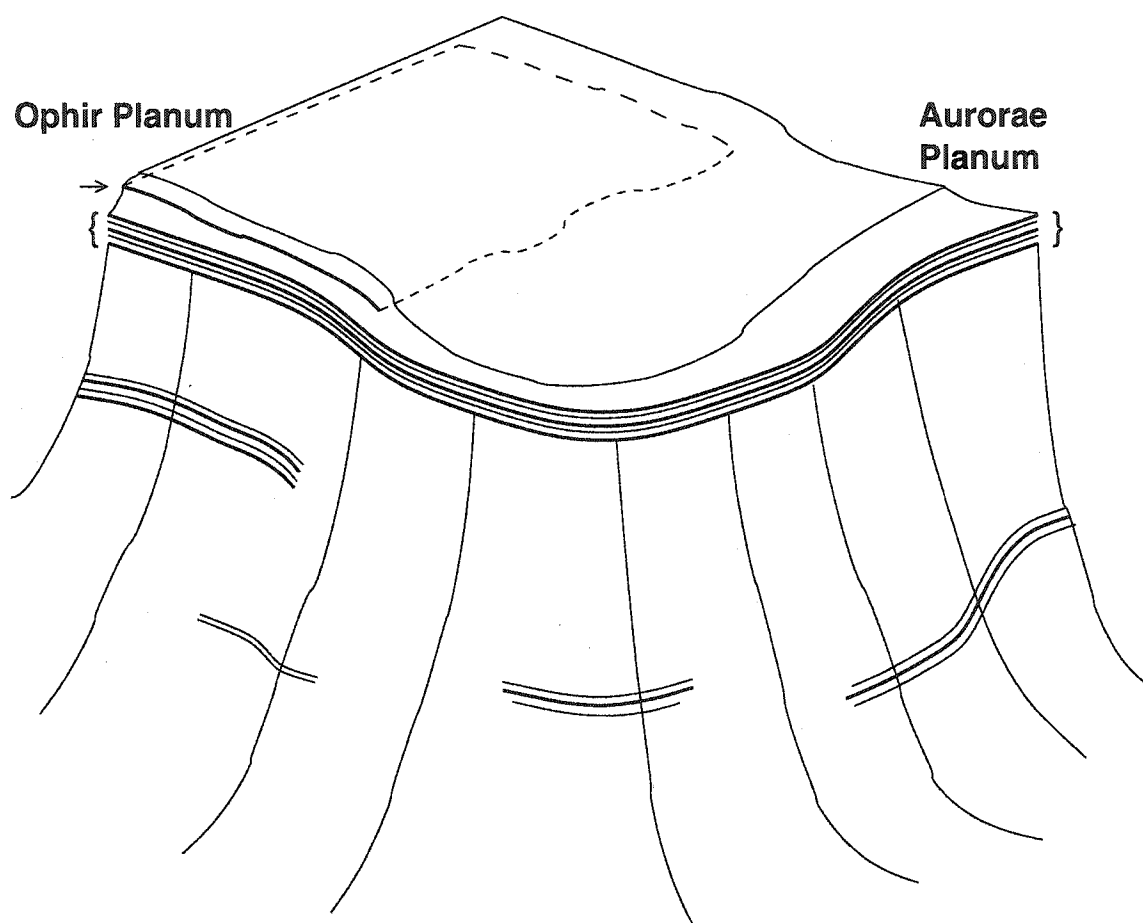


Figure 4.29: This cartoon is a perspective view looking northwest at the boundary between Ophir and Aurorae Plana. To the left is Coprates Chasma and to the right Capri Chasma. This cartoon illustrates the hypothesis that the boundary between Ophir and Aurorae Plana is due to the eastern extent of the topmost strong layer (arrow). This cartoon also illustrates the hypothesis that the next most resistant layer (indicated by the brackets) observed below the topmost strong layer along the rim of Coprates Chasma is the same as the resistant sequence that forms the rim in Capri Chasma. The strong layers displayed below that are schematic.

emplacement. 2) Perhaps the topography was inverted, the area that is now the southern rim of the chasma was originally topographically higher than the areas that became the massif and north rim when the layer was emplaced. 3) Alternately, it may also be due to differential timing in the opening of the chasma. Perhaps the trough between what is now the massif and the south rim opened, then the strong layer was emplaced over the area of the plateau north of this proto-chasma, and then later the trough that separated the massif and the north rim opened.

The concept of a kilometers deep megaregolith a few kilometers below the surface (e.g. Carr, 1979, pp. 3000-3001; Tanaka and Golombek, 1989, p. 386; Davis and Golombek, 1990, pp. 14,244-14,245; Clifford, 1993, p. 10,975) no longer seems viable (McEwen et al., 1999) in this area. The topmost strong layer observed in Coprates Chasma, and the resistant sequence that forms the Capri Chasma rim show that indurated, bedded units are just below the plateau surfaces. However, these resistant layers are topped by a variable thickness of mantling material (less than 100 m). There are a few images where there may be a hint of bedding in this material, but it mostly appears fine-grained and massive. There appears to be a rough correlation with the thickness of this mantle with proximity to large craters, suggesting that some of this material is impact ejecta, with the rest being deposited by other processes.

The individual strong layer that we see near the top of the layered stack of materials in this portion of Coprates Chasma is the exception, not the norm. We do not observe another individual layer by itself of this thickness, competency, or extent further down-section in the strata where it outcrops. More resistant bedded sequences are observed further down-section that have a darker tone than surrounding units, and also form more resistant knobs and spurs. In locations not obscured by talus and mantling between these resistant units we observe lighter-toned, finely bedded units which are not as resistant to erosion. It is this material which appears to make up the largest part of the stratigraphic stack.

This dichotomy of strength in the slope materials is evident in the distribution of blocks within eastern Coprates Chasma. There is certainly an observational bias

based on where there are images with resolutions better than 4 m/pixel, but blocks are only observed downslope of resistant layers. If entire slopes were composed primarily of resistant volcanic layers, we might expect a larger amount of observed blocks. Similarly, if the materials that formed the slopes were devoid of cliff-forming material, then no blocks should be seen. The fact that they are observed downslope of dark-toned, layered outcrops, indicates that these units are indeed relatively strong, but also infrequent in the stratigraphic stack. Lava breaks into blocks about the thickness of the lava unit, or the size of columnar joints within that unit (Milazzo et al., 2003). Blocks are not seen everywhere a resistant layer crops out perhaps because they are buried by talus, or roll down the slope so far that they are broken into smaller fragments. This lack of blocks is not surprising because it is rare on the Earth for such large blocks to be transported far without disruption.

4.6 Conclusions

Observations of the layering in eastern Coprates Chasma indicate that the material into which the chasma is carved consists of alternating strong and weak layers. The presence and extent of the occasional strong layers has a large impact on chasma and slope morphology and that of the surrounding plana. Different combinations of strong and weak layers may have some impact into the varying morphologic character of chasmata within the Valles Marineris, as well as the locations and sizes of landslides. This difference in strength properties could also explain the paucity of observed boulders and blocks on Valles Marineris slopes if the thin strong layers are the only source of boulder-sized and larger particles.

Understanding the stratigraphy has also led us to identify a strong layer near the top of the stratigraphic stack both in the north slope of eastern Coprates Chasma, and near the crest of the massif there. This massif is notable because it is one of the rare free-standing massifs within the Valles Marineris to retain its original flat-topped plateau surface. The massif preserves this surface because the strong layers are helping the massif resist erosion and collapse.

There is an elevation offset between the outcrops of this layer in the northern chasma slope and its outcrops in the massif indicating subsidence of the massif, most likely due to extensional fault motion. There are several models for how the Valles Marineris formed, including different combinations of rifting, collapse, and mass wasting. These observations confirm that extensional faulting was a contributing factor in the formation of this portion of Coprates Chasma.

It is still difficult to determine the origin of the thin layers that make up the majority of the stratigraphic sequence of the Valles Marineris. Whether the thin layers in the Valles Marineris are fluvial, aeolian, or volcanic sedimentary layers, thin lava layers, welded tuff layers, or some combination of these, their contrast to the occasional strong units indicates a change in either the volcanic source or environmental conditions when these layers were emplaced.

The observations of the topmost strong layer in eastern Coprates Chasma indicate that the last basaltic lava flow in this area covered at least 7000 km², and possibly an increased area that consists of a large portion of Ophir Planum, either prior to or during chasma formation. The boundary between Ophir and Aurorae Plana may be the easternmost extent of this layer. Similarly, outcrops along Capri Chasma indicate that the Aurorae Planum surface is underlain by a stack of resistant layers that is also present stratigraphically below the strong layer which outcrops in eastern Coprates Chasma. These resistant layers are buried by 100 m or less of mantling material, which obscures the transition between the plana.

CHAPTER 5

Constraints on the origin of fine layers in Ganges Mensa and Hebes Mensa, Mars

5.1 Overview

This chapter is being prepared for submission to the *Geophysical Research Letters*, by Ross A. Beyer and Alfred S. McEwen. Alfred McEwen aided in focusing certain elements of the analysis and discussion, and he contributed to the overall style and presentation of the manuscript.

Ganges Mensa and Hebes Mensa are large mesas in the Valles Marineris system on Mars. They have long been identified as having a different origin from the strata exposed in the slopes of their enclosing chasmata. Their surfaces and slopes display a variety of layering within the mensae. Layering at the finest scales that can be resolved by the Mars Orbital Camera (MOC) is indicative of the processes that formed the layers and the mensae in general. The MOC can resolve layer exposures wider than ~ 5 m, but the observed cross-section of the layer depends on the slope and viewing angle. At a few places the dip angle and dip direction of these very thin layers can be measured with a combination of MOC and Mars Orbital Laser Altimeter (MOLA) data. Our measurements indicate horizontal to shallow dip angles for these fine layers, which place some constraints on their origins.

5.2 Introduction

Ganges Mensa is located near 311° E, 7.5° S (Figures 5.1 and 5.2), and has been studied ever since it was first resolved with the Mariner 9 spacecraft. Masursky (1973) indicated that this was a finely layered deposit, and that those layers did not match the layering seen in the canyon slopes. Sharp (1973) noted that the layers

appeared near-horizontal. Hebes Mensa is located near 283° E, 1° S (Figures 5.3 and 5.4), and is within the entirely closed Hebes Chasma. It also has been a subject of study since the early Mariner days. Observations by the Viking spacecraft indicated that there were light and dark layers of uniform thickness within these mensae (Blasius et al., 1977), and the similarity to other layered mesas and deposits in the Valles Marineris was noted (Komatsu et al., 1993). However, Malin and Edgett (2001) showed that some of the albedo patterns previously attributed to layering were not bedrock layers, but topographic benches where dark toned aeolian material accumulated (their Figure 26). Komatsu et al. (2004) show a similar example of dark toned material collecting on a topographic bench on Hebes Mensa (their Figure 11). Ganges and Hebes Mensae are indeed layered, but the layers are too thin to have been resolved by cameras before MOC (Malin and Edgett, 2001).

Many hypotheses for the origin of structures like Ganges and Hebes Mensae have been discussed (see Lucchitta et al., 1992, for a review). One of them, deposition in a low-energy lacustrine environment (Nedell et al., 1987; Malin and Edgett, 2000), accounts for the thin, areally extensive, bedded layers that are observed. Layers deposited in this fashion should be horizontal unless they were tilted by tectonic activity.

More recently, Lucchitta et al. (1994) noted that these mensae appeared to have steep sides, and suggested similarities to Icelandic tuya which are volcanic constructs that erupt and are built sub-glacially. They often become large enough to rise above the glacial ice and erupt sub-aerially. Chapman and Tanaka (2001) and Komatsu et al. (2004) further explored the tuya analog for these mensae and other similar structures in the Valles Marineris. They found similarities in that the easily eroded flanks of tuya may be similar to the fluted flanks of the mensae. Chapman and Tanaka (2001) indicated that Ganges and Hebes Mensae had an ideal tuya form and that the fine layers were dipping in a down-slope direction with horizontal to steep dips. Chapman (2002) stated that even crudely bedded materials observed in the slopes of Ganges Mensa are steeply dipping.

These studies were the first to raise the issue of these fine layers being non-

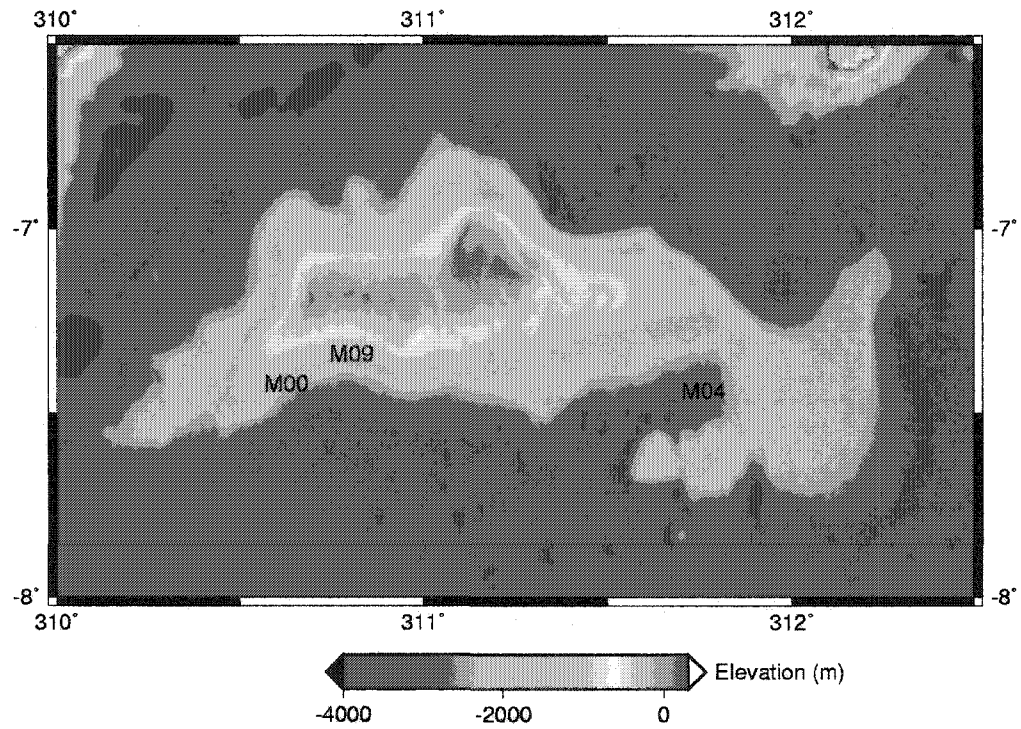


Figure 5.1: The shading on this map of Ganges Mensa is the from the MDIM, and the colors are from the 1/128th degree gridded MOLA elevation data. The three markers on the map indicate the approximate location of the portions of three MOC images that are discussed in this study. *M00*: M00/02988, Figure 5.9. *M09*: M09/03505, Figure 5.6. *M04*: M04/01737, Figure 5.10.

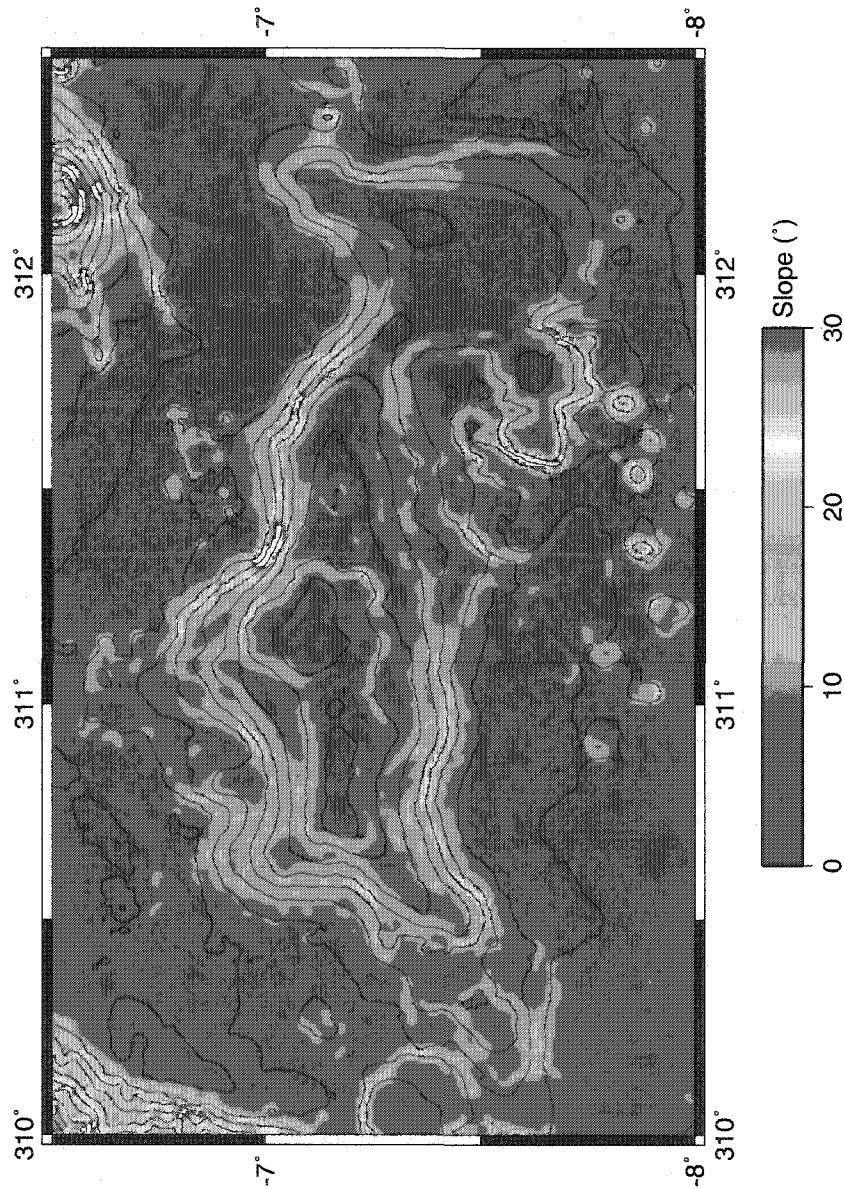


Figure 5.2: Slope map of Ganges Mensa created from 1/128th degree gridded MOLA data. Slopes greater than 30° are white, 500 m elevation contours.

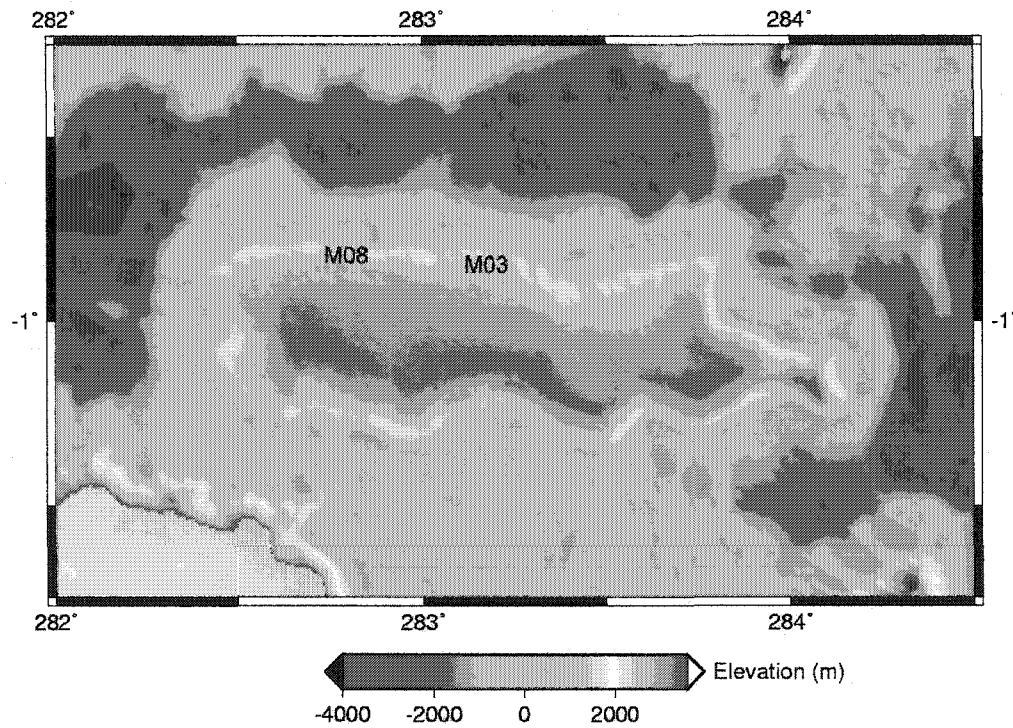


Figure 5.3: The shading on this map of Hebes Mensa is from the MDIM, and the colors are from the 1/128th degree gridded MOLA elevation data. The two markers on the map indicate the approximate location of the portions of two MOC images that are discussed in this study. *M08*: M08/06285, Figure 5.7. *M03*: M03/00648, Figure 5.8.

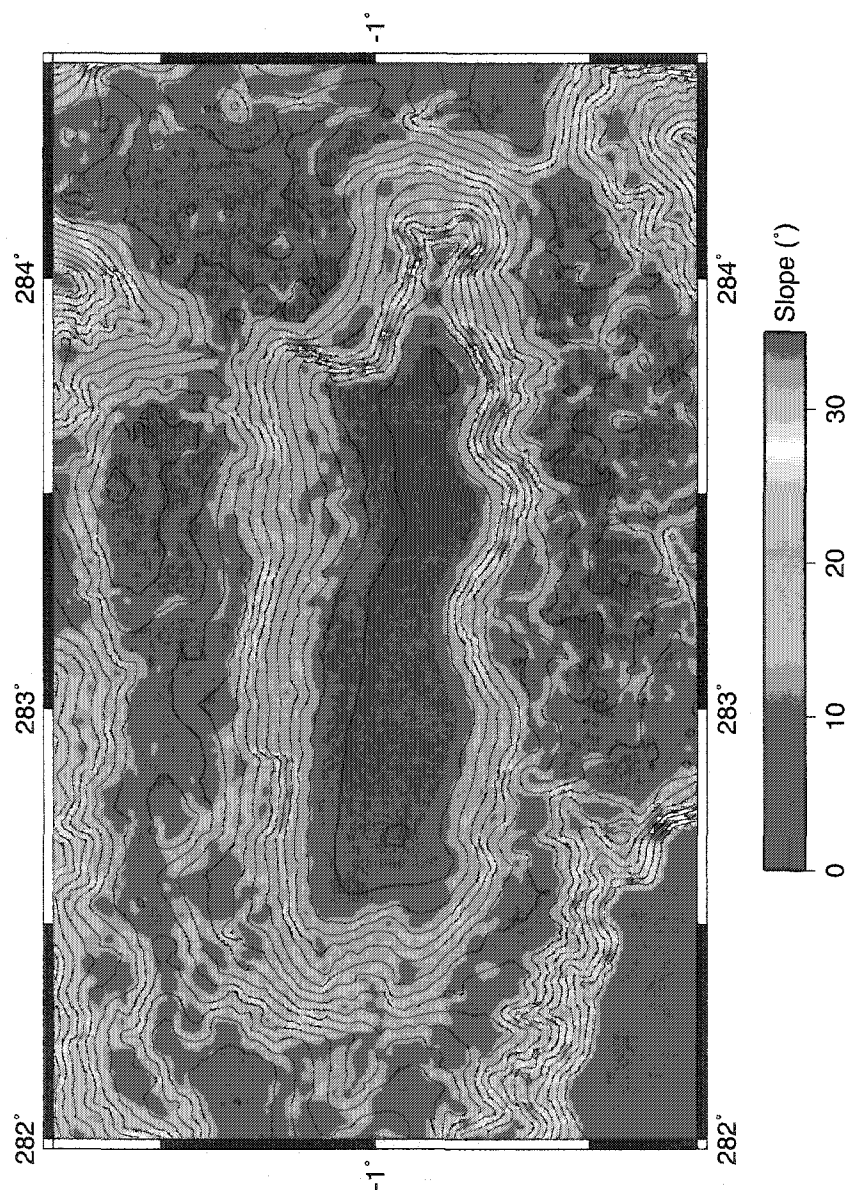


Figure 5.4: Slope map of Hebes Mensa created from 1/128th degree gridded MOLA data. Slopes greater than 35° are white, 500 m elevation contours.

horizontal. Many qualitative descriptions of the orientations of these fine layers have been made, but none have made quantitative measurements of the dip angle or dip direction. A definitive measurement might help to support one particular origin hypothesis over another. Unfortunately, measuring such characteristics on the flanks of the mensae is difficult. It can be accomplished in a few locations using data from the Mars Orbital Camera (MOC) (Malin et al., 1992; Malin and Edgett, 2001) and the Mars Orbital Laser Altimeter (MOLA) (Zuber et al., 1992; Smith et al., 2001). These measurements are difficult because the fine layers are not very distinct. If MOC images are separated even by just a few hundred meters, it is not clear which layers match between the two images. Therefore images with overlapping coverage, and multiple MOLA tracks are the ideal circumstances for accurate measurements. Such conditions are rare, but morphological comparisons, shadow measurements, and individual MOLA tracks aligned with MOC images can help to narrow parameter space and constrain dip angle and direction.

We were only able to make one certain dip measurement, but we were able to constrain the dip angles of beds in the mensae. Measuring these values certainly raises more questions than it answers, and it does not particularly help to differentiate between the different origin hypotheses. However, these measurements constrain the dip angle of the finest beds observed in the mensae which does have implications for the various origin hypotheses.

5.3 Observations

5.3.1 Layer Dip Angles and Surface Slope Angles

A first order constraint on the dip angle of bedded units can be made from the overall angle of the slope on which they are observed and the surface features of that slope. Lucchitta (1981) first indicated that the fluting on the flanks of these mensae was shaped like yardangs, a landform generally carved from indurated but friable materials (e.g. Ward, 1979; Greeley and Iversen, 1985; Livingstone and Warren, 1996). Yardangs have the shape of inverted boat-hulls, and so a simple model

of a layered volume cut by a sloping surface with yardangs on it might look like Figure 5.5. This figure shows that beds which have a dip direction parallel to the dip direction of the overall surface slope have a different morphology when viewed from above if the beds are dipping more or less steeply than the overall slope. The expression of these layers from above is very similar (Figures 5.5d and g), and we cannot differentiate reliably between layers whose dip direction is parallel to the dip direction of the overall slope (as in Figure 5.5e), those whose dip direction is into the direction of the slope, (or 180° from the dip direction of the overall slope as in Figure 5.5h), or even horizontal layers.

Figure 5.6 shows thin layers exposed on the south face of Ganges Mensa that are exposed in the yardang forms that cover this surface. The surface expression of the layers resembles Figure 5.5d or g, not Figure 5.5a, indicating that these layers are dipping less steeply than the overall surface slope. The slope in this area is about 25° , so these layers must be dipping at an angle less than that.

Similarly, Figures 5.7 and 5.8 show thin layers exposed on the north face of Hebes Mensa. Again, the morphology that we observe is similar to Figure 5.5d or g, indicating that these layers are also dipping at an angle less than the overall surface slope. That slope is 10 to 15° for the portion of M03/00648 in Figure 5.8. The portion of M08/05285 shown in Figure 5.7 has two broad slope regions, one from 10 to 15° and the other up to 30° .

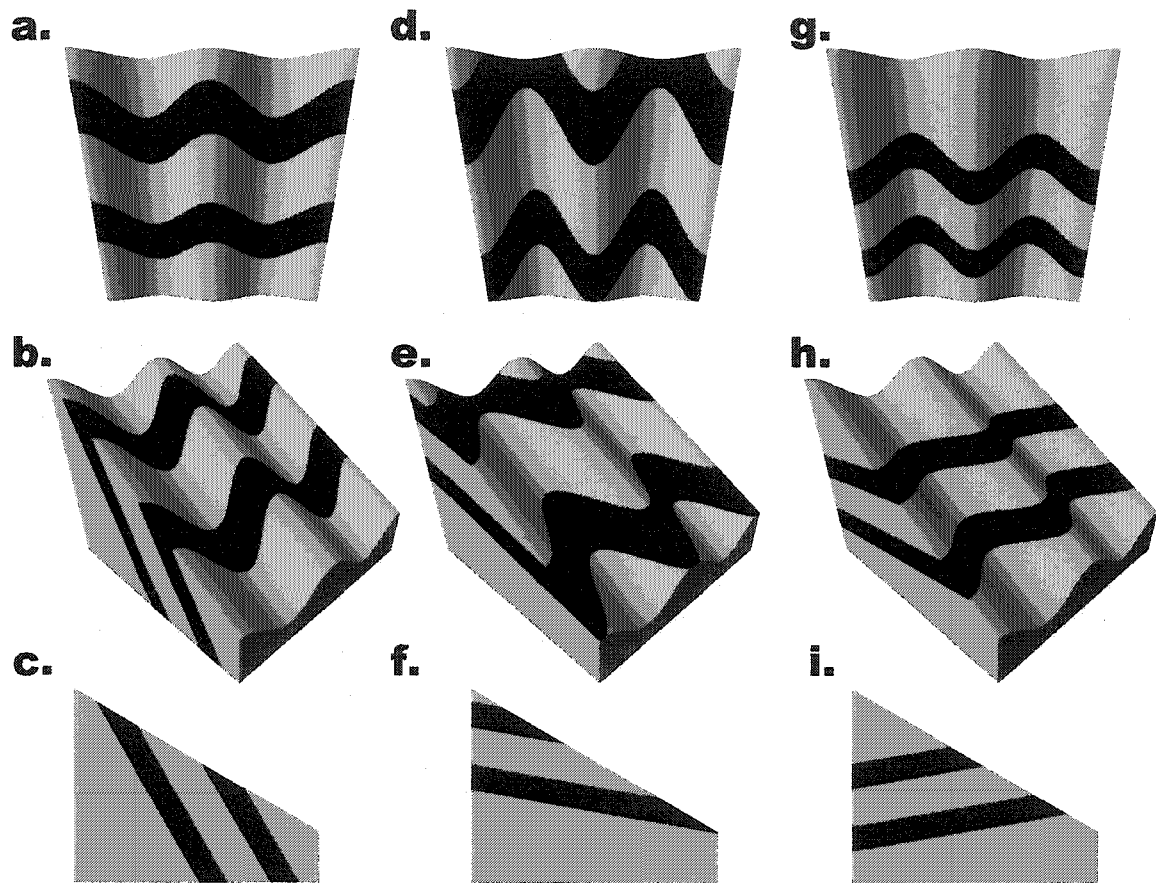


Figure 5.5: These cartoons show how layers with dips steeper and shallower than the overall slope are expressed. The upper surface is sinusoidal and tilted at 30° . North is to the top of figures a, d, & g, the block is illuminated by a 2 P.M. sun, an illumination angle similar to that of MOC images at the equator. *a.* View from above of layers dipping more steeply than slope of upper surface. *b.* Perspective of layers dipping more steeply than slope of upper surface. *c.* Side view of layers dipping at an angle steeper than the slope of the upper surface. *d.* View from above of layers dipping less steeply than slope of upper surface. *e.* Perspective of layers dipping less steeply than slope of upper surface. *f.* Side view of layers dipping at an angle shallower than the slope of the upper surface. *g.* View from above of layers dipping shallower than slope of upper surface, but dipping into the slope, rather than along, or parallel to the slope as in d. *h.* Perspective of layers with shallower dips than slope of upper surface, but dipping into the slope, rather than along, or parallel to the slope as in e. *i.* Side view of layers dipping at an angle shallower than the slope of the upper surface, but dipping into the slope, rather than along, or parallel to the slope as in f. Naturally, horizontal beds would be very similar to d or g.

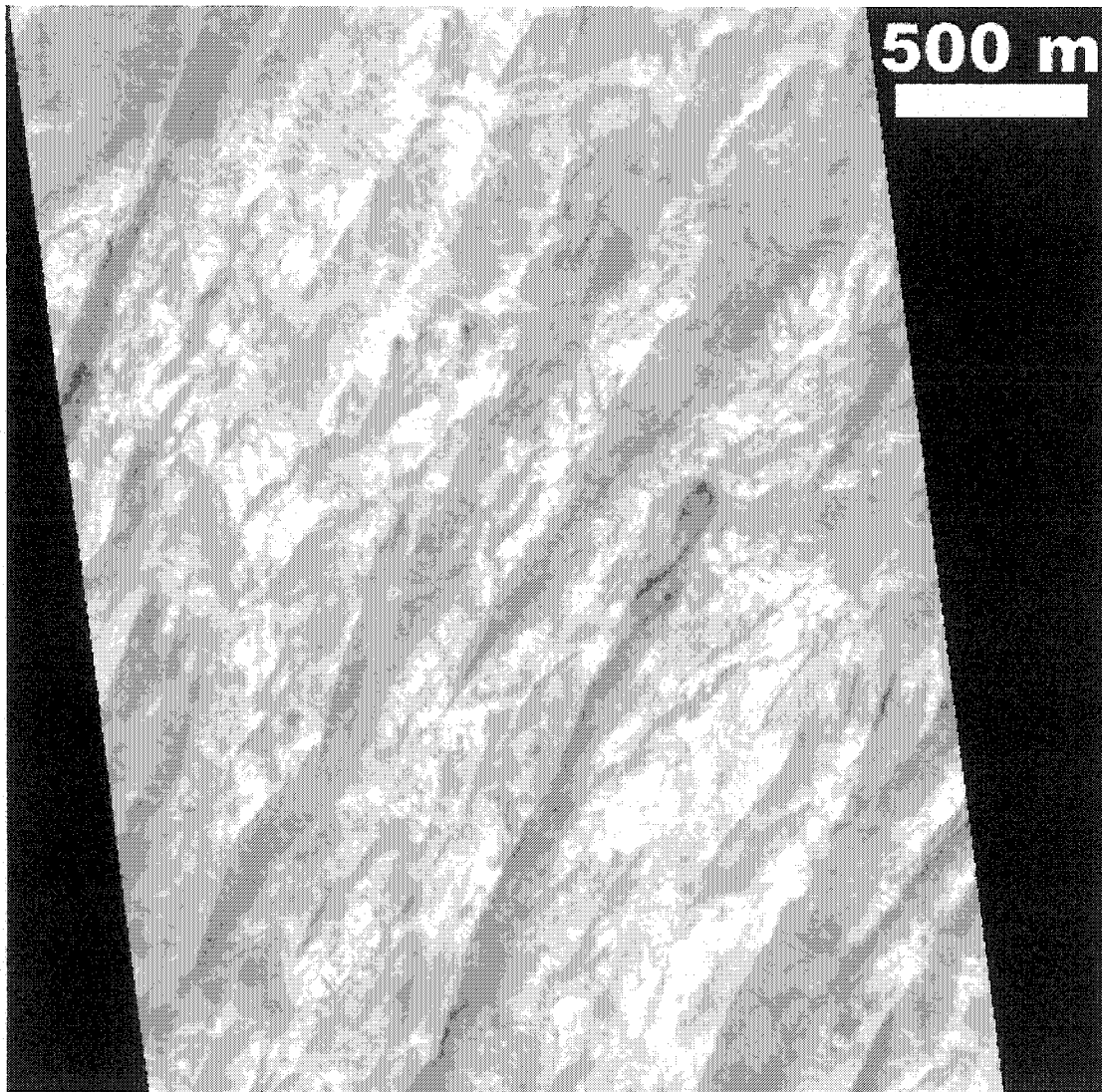


Figure 5.6: This is a portion of the MOC image M09/03505, it shows thin layers on the south face of Ganges Mensa that are exposed in the yardang forms that cover this surface.

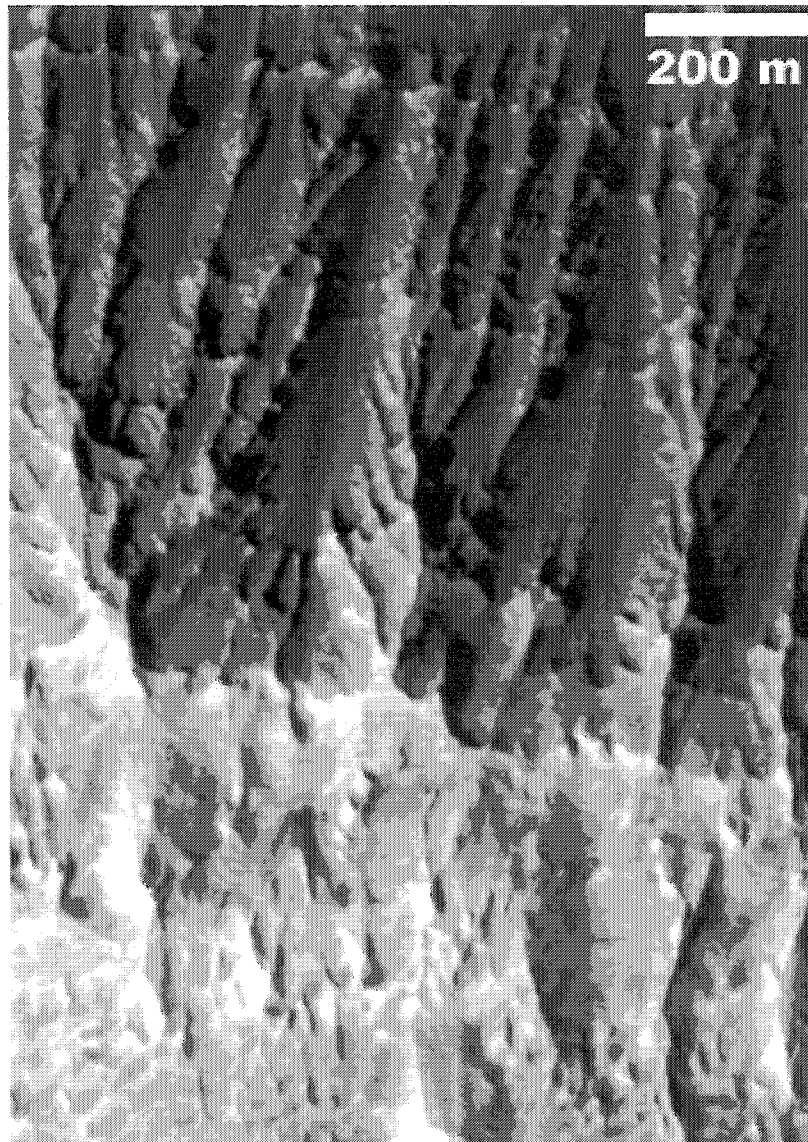


Figure 5.7: This is a portion of the MOC image M08/06285, it shows thin layers on the north face of Hebes Mensa that are exposed in the yardang forms that cover this surface. There are two regions of broad overall slope here. The northern half of this image has a slope of $\sim 30^\circ$ and displays an almost spur-and-gully type of morphology. The southern portion of the image has a general slope of 10 to 15° .

5.3.2 Dip Angles in a Large Yardang

The MOC image M00/02988 (Figure 5.9) shows a large yardang form on the south face of Ganges Mensa. This yardang appears to have lineations on its southeast flank. Since this yardang casts a shadow, we can use shadow measurements to determine the height of the ridge above the base, and the slope of the southeast flank, from which we can determine the dip angle of the lineations.

The shadow measurements of the southern portion of the yardang indicate that its highest points are 150 to 180 m above the local surface, and that the slope of the flank is therefore about 64° . If the lineations represent layers, those layers would dip northwards (180° in azimuth from the dip direction of the overall mensa slope here) at a steep angle of 66° , whereas the local surface slope is only 16° in this region.

5.3.3 Dip Angles in a Finely Layered Sequence

In the southeast region of Ganges Mensa the MOC images M03/04405 and M04/01737 overlap, such that the finely layered sequence that they display can be correlated across the width of both images. Additionally, there are four MOLA tracks that cross the layered unit in these two images. We were able to pick out two individual layers for which four MOLA shots occurred on top of or nearby. More than three points overdetermine a plane, and we were able to obtain a least squares solution for each layer.

Unfortunately, the four locations for each layer were very near to being collinear. As such, the solutions for those planes end up being unstable and very sensitive to errors in the measurements. Even though the dip angles of these planes were reasonable (8° and 18°), their dip directions were almost 90° apart. The poor stability of the solutions resulting from the almost collinearity of the measured points makes the solutions for those planes almost meaningless.

While we cannot obtain a good solution for the dip angles of these layers, we can at least constrain their dip in another way. The finely layered sequence in M04/01737 appears to have a morphology that shows the topmost layers of the



Figure 5.8: This is a portion of the MOC image M03/00648, it shows thin layers exposed in yardang forms that cover this 10 to 15° slope, showing that those layers must be dipping at a shallow angle.

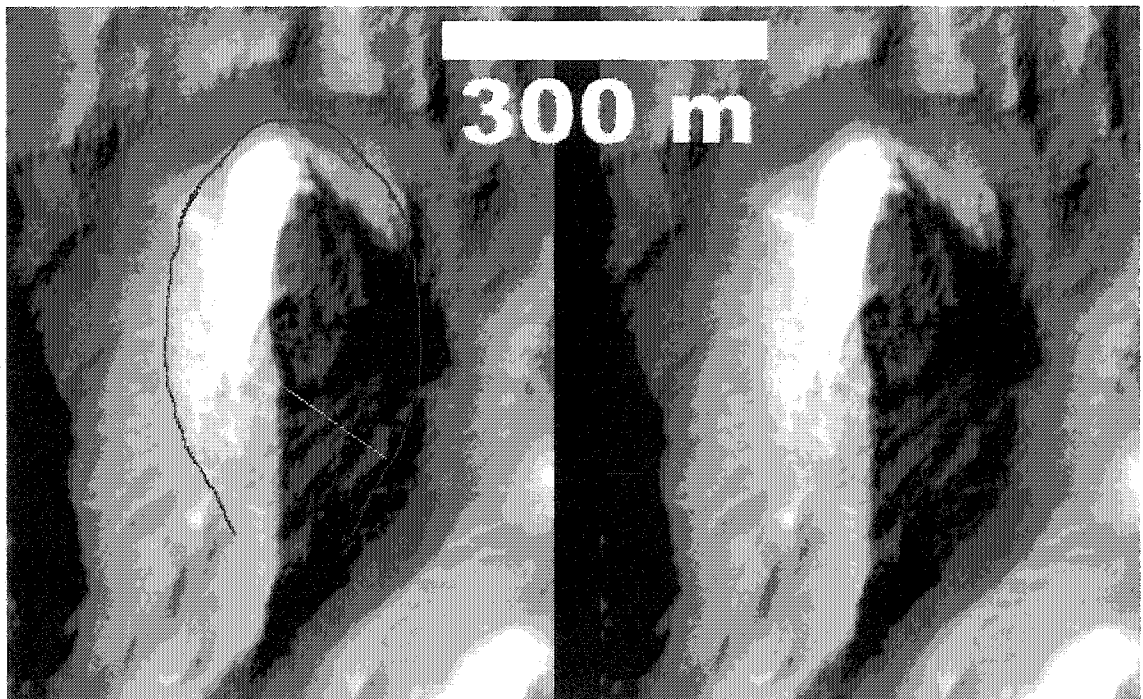


Figure 5.9: This portion of the MOC image M00/02988 shows a large yardang on the south face of Ganges Mensa (N is to the top). The red boundary indicates the outline of what we think is the extent of this yardang. The yellow line indicates the line in the down-sun direction that was used to estimate the slope of the flank of the yardang.

sequence towards the north, and the stratigraphically lowest layers towards the south. If this sequence were flat-lying, we would expect the elevations of those layers to smoothly transition from high elevations towards the north to low elevations towards the south. However, close examination of the MOLA data that correspond to this image indicate that these layers may not be entirely horizontal (Figure 5.10). The morphology exposed in the MOC image indicates that these layers have been weathered back into a stair-step-like pattern. However, the MOLA data indicate that these layers may have been rotated down to the north, such that the southern portions of the stratigraphically lower layers have a higher absolute elevation than those layers which are stratigraphically above them (Figure 5.11).

The absolute elevation differences in this case are only tens of meters, and the point to point slopes are only a few degrees. However, this combination of MOC and MOLA data indicate that this particular sequence of fine layers dips down very slightly in a northwards direction, which is into the slope of Ganges Mensa, not parallel to it (radially outwards from the mensa).

5.4 Discussion

Allen (1979) measured the overall slopes of five Icelandic tuya and found that the mean of the steepest slopes was $34^\circ \pm 4^\circ$. Chapman (2002) shows a figure of the north face of Ganges Mensa, and indicates that it has “steeply dipping” beds and displays a cartoon showing these beds (her Figure 15). Unfortunately, the precise meaning of “steeply dipping” is not defined. However, the beds in this cartoon are only dipping $15 - 20^\circ$ downslope. Her figure (which contains portions of the MOC images M03/04405 and M04/01737) displays morphology which is consistent with Figure 5.5d or g, and the average slope in this area is around 30° (Figure 5.2). This indicates that the dip angle of the beds is less than 30° and is consistent with the cartoon in Figure 15 of Chapman (2002), but characterizing this angle as “steep” is probably not appropriate.

This morphology is very common in MOC observations of the flanks of Ganges

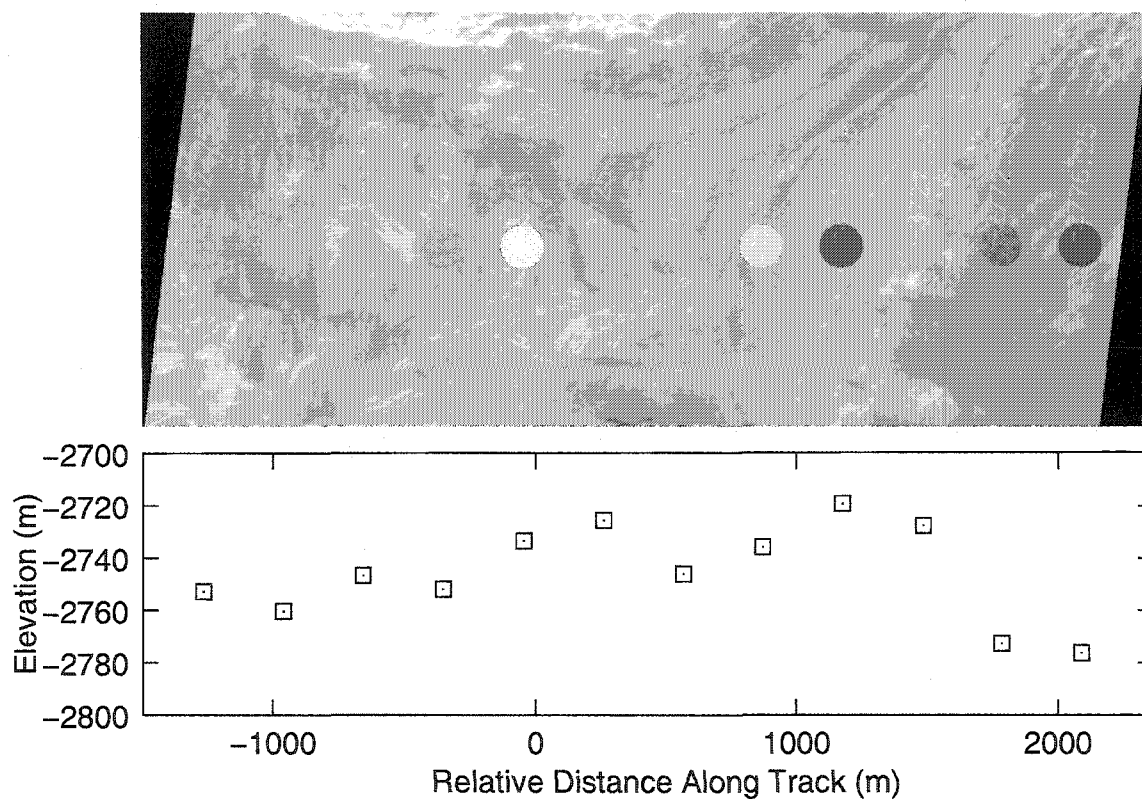
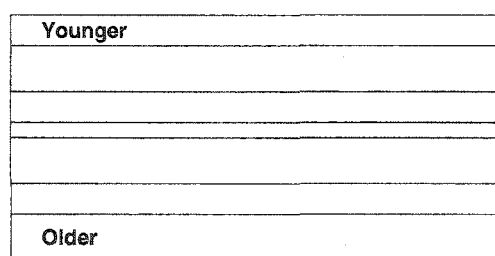


Figure 5.10: The image is a portion of MOC image M04/01737, and the colored circles are the footprints of MOLA track 11994 (168 m in diameter), annotated with the MOLA elevations. The plot is a profile view of the MOLA data from the side, it has no vertical exaggeration.

a.



b.

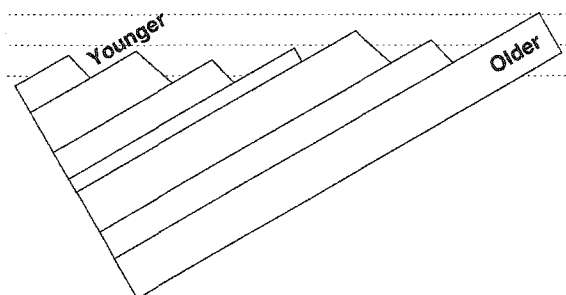


Figure 5.11: This cartoon shows an example of originally horizontal layers in *a.*, with the youngest layer on the top and the oldest layer on the bottom. The cartoon in *b.* shows a possible configuration if these layers were eroded and tilted. It can be seen that stratigraphically older layers can have absolute elevation values higher than stratigraphically younger layers.

and Hebes Mensae. Since the slopes are generally less than 30° (Figures 5.2 and 5.4), we can make the generalization that most of the fine layers observed on the flanks of these mensae are dipping at angles of less than 30° . It is important to note that this observation would also be consistent with completely horizontal layers. Similarly, it would be consistent with layers that dip shallowly in a direction parallel to the overall slope (radially outwards from the mensae, like Figure 5.5f), or in a dip direction into the slope (radially inwards to the mensae, like Figure 5.5i).

There may be exceptions to this, and the lineations on the large yardang in section 5.3.2, may be an example. In this case if the lineations do represent layers, then they are steeply dipping, but their dip direction is into the slope, not parallel to the dip direction of the overall slope. However, these lineations are poorly resolved, and may be features that do not represent actual strata, but remnants of the processes that formed this yardang, or subsequent aeolian modification.

Since we do not find widespread evidence of layering which dips steeply in a direction radially outwards from these mensa, then the layers can not be analogous to the steeply dipping foreset beds often observed in terrestrial tuya. Furthermore, the mensae have very shallow slopes overall (Figures 5.2 and 5.4), which is inconsistent with the ideal tuya form that has been proposed for these mensae in the past. Even if steeply dipping foreset beds had been eroded into the slopes that we observe on these mensae then morphologies like that in Figure 5.5a should be common on the shallow flank slopes that we observe.

These observations do not necessarily preclude the mensae from having formed in a manner broadly similar to terrestrial tuya. as these characteristics could be consistent with a more severely eroded tuya. The steeply dipping foreset beds may have been eroded away or be preserved in unimaged or buried locations, and the fine layering that is observed may be from the inner core of the tuya. Alternately, the mensae are many times the size of terrestrial tuya, and it is possible that subglacial edifices of this size do not have the steeply dipping foreset beds observed on terrestrial tuya. In this manner, the physical processes of volcanic construction of such a large edifice beneath and through many kilometers of ice on Mars may have

fundamental differences from those of terrestrial tuya that we do not yet appreciate.

In most of the origin hypotheses prior to the tuya origin ideas, the chasmata were formed, some other material filled them up, and then they had to be excavated again, leaving the mensae behind. The mechanism of initial chasma formation notwithstanding, this filling and then excavation would have moved on the order of hundreds of thousands of cubic kilometers of material into and then out of the chasmata in order to leave behind on the order of ten thousand cubic kilometers of material for Ganges and Hebes Mensae.

Malin and Edgett (2000, 2001) have implied that the only the initial opening of the chasmata was required, and the material that the mensae consist of was always there, and was exhumed by the initial chasmata formation. This hypothesis eliminates a great deal of material transport, but fails to account for why the mensae, which appear to consist of material that is more friable than the material in the wall rock of the chasmata, are left behind during chasmata formation.

The tuya origin is an attractive hypothesis because the subsequent fill material would be ice, not heavier and more persistent rock or sediment. If the chasmata were filled with many kilometers of ice, a change in climate would cause it to disappear. However, the problem with filling the chasmata with ice is not limited to just the chasmata. In order for chasmata ≥ 4 km deep at the equator to be filled with ice, the whole planet would need to be wrapped in an intense ice age. Mars climate modeling by Richardson and Wilson (2002) indicate that during periods of high obliquity, ice could be stable at the equator. However, Head et al. (2003) indicate that the topography doesn't appear to support large ice sheets equatorward of 30° in the recent past. For the tuya origin model of the mensae, there is a big difference between stable ground ice, and many kilometers of glacial ice sitting on the surface.

An unexpected new observation from this study is that of the one instance of fine layers located on the south slope of Ganges Mensa which appear to have a very slight dip down to the north. This would not be consistent with the hypothesis that this mensa is a tuya. We do not know if this dip is indicative of originally dipping beds of some kind or if this sequence, or the mensa as a whole, was tectonically

tilted down to the north. Volcanic layers can be emplaced at shallow angles, but the orientation of these layers indicates that the source would have been to the south. There is a pair of finely layered mounds to the south, but they do not appear to be obvious volcanic sources.

5.5 Conclusions

We do not find any evidence of layering which dips steeply in a direction radially outwards from the mensae in Ganges or Hebes Chasmata. Similarly, the MOLA topography indicates that the overall slopes of these mensae are relatively shallow, not steep. The similarity of the morphologies of these mensae to that of terrestrial tuya is therefore not good, although subglacial volcanic edifices of this magnitude may have a distinctly different expression on Mars.

We find that the fine layers observed on the flanks of Ganges and Hebes Mensae dip at an angle shallower than the overall surface slope of the mensae flanks (with one possible exception). That overall slope of the flanks of the mensae is mostly between 5 and 15° for Ganges Mensa and about 5° higher for Hebes Mensa at the 1/128th degree gridded MOLA data scale.

The finest layers in Ganges and Hebes Mensae are horizontal to shallowly dipping. Unfortunately, this does not particularly exclude any of the various hypotheses for the origins of these mensae. However, any formation hypothesis must take these measurements into account.

Finally, a sequence of layers on the south slope of Ganges Mensa that dips down to the north has been identified for the first time. If these layers were emplaced horizontally, then this sequence or the mensa as a whole was tectonically tilted down to the north. If these layers were emplaced at that angle, it potentially indicates a volcanic origin whose source is south of this outcrop.

REFERENCES

- Acton, C. H. (1996). Ancillary data services of NASA's Navigation and Ancillary Information Facility. *Planetary and Space Science*, **44**, pp. 65–70.
- Acton, C. H. (1999). SPICE Products Available to the Planetary Science Community. In *Lunar and Planetary Science XXX*, #1233. Lunar and Planetary Institute, Houston (CD-ROM).
- Aharonson, O., N. Schorghofer, and M. F. Gerstell (2003). Slope streak formation and dust deposition rates on Mars. *Journal of Geophysical Research*, **108**(E12), pp. 12–1. doi:10.1029/2003JE002123.
- Allen, C. C. (1979). Volcano-ice interactions on Mars. *Journal of Geophysical Research*, **84**, pp. 8048–8059.
- Anderson, J. D., E. L. Lau, W. L. Sjogren, G. Schubert, and W. B. Moore (1997). Europa's differentiated internal structure: Inferences from two Galileo encounters. *Science*, **276**, pp. 1236–1239.
- Arvidson, R. E., F. P. Seelos, K. S. Deal, W. C. Koeppen, N. O. Snider, J. M. Kieniewicz, B. M. Hynek, M. T. Mellon, and J. B. Garvin (2003). Mantled and exhumed terrains in Terra Meridiani, Mars. *Journal of Geophysical Research*, **108**(E12), pp. 14–1. doi:10.1029/2002JE001982.
- Bandfield, J. L., V. E. Hamilton, and P. R. Christensen (2000). A Global View of Martian Surface Compositions from MGS-TES. *Science*, **287**(5458), pp. 1626–1630.
- Banerdt, W. B., M. P. Golombek, and K. L. Tanaka (1992). Stress and tectonics on Mars. In Kieffer, H. H., B. M. Jakosky, C. W. Snyder, and M. S. Matthews (eds.) *Mars*, chapter 8, pp. 249–297. The University of Arizona Press, Tucson.

- Beyer, R. A., A. S. McEwen, and R. L. Kirk (2003). Meter-scale slopes of candidate MER landing sites from point photoclinometry. *Journal of Geophysical Research*, **108**(E12), pp. 26–1. doi:10.1029/2003JE002120.
- Binder, A. B., R. E. Arvidson, E. A. Guinness, K. L. Jones, T. A. Mutch, E. C. Morris, D. C. Pieri, and C. Sagan (1977). The geology of the Viking Lander 1 site. *Journal of Geophysical Research*, **82**, pp. 4439–4451.
- Blair, T. C. and J. G. McPherson (1999). Grain-Size and Textural Classification of Coarse Sedimentary Particles. *Journal of Sedimentary Research*, **69**(1), pp. 6–19.
- Blasius, K. R., J. A. Cutts, J. E. Guest, and H. Masursky (1977). Geology of the Valles Marineris - First analysis of imaging from the Viking 1 orbiter primary mission. *Journal of Geophysical Research*, **82**, pp. 4067–4091.
- Bourke, M., M. Balme, R. A. Beyer, K. K. Williams, and J. Zimbelman (2004). How High is that Dune? A Comparison of Methods Used to Constrain the Morphometry of Aeolian Bedforms on Mars. In *Lunar and Planetary Science XXXV*, #1831. Lunar and Planetary Institute, Houston (CD-ROM).
- Bresenham, J. E. (1965). Algorithm for Computer Control of a Digital Plotter. *IBM Systems Journal*, **4**(1), pp. 25–30.
- Burr, D. M. (2003). Hydraulic calculations for Athabasca Vallis, Mars. *Hydrological Sciences Journal*, **48**(4), pp. 655–664.
- Burr, D. M., P. A. Carling, and R. A. Beyer (2002a). Investigations into Dune Features in Athabasca Valles, Mars. *AGU Fall Meeting Abstracts*, (#P71A-0445).
- Burr, D. M., P. A. Carling, R. A. Beyer, and N. Lancaster (2004a). Diluvial Dunes in Athabasca Valles, Mars: Morphology, Modeling and Implications. In *Lunar and Planetary Science XXXV*, #1441. Lunar and Planetary Institute, Houston (CD-ROM).

- Burr, D. M., P. A. Carling, R. A. Beyer, and N. Lancaster (2004b). Flood-formed dunes in Athabasca Valles, Mars: morphology, modeling, and implications. *Icarus*, in press.
- Burr, D. M., J. A. Grier, A. S. McEwen, and L. P. Keszthelyi (2002b). Repeated Aqueous Flooding from the Cerberus Fossae: Evidence for Very Recently Extant, Deep Groundwater on Mars. *Icarus*, **159**(1), pp. 53–73.
- Burr, D. M., A. S. McEwen, and S. E. H. Sakimoto (2002c). Recent aqueous floods from the Cerberus Fossae, Mars. *Geophysical Research Letters*, **29**(1), pp. 13–1. doi:10.1029/2001GL013345.
- Cabrol, N. A., E. A. Grin, M. H. Carr, B. Sutter, J. M. Moore, J. D. Farmer, R. Greeley, R. O. Kuzmin, D. J. DesMarais, M. G. Kramer, H. Newsom, C. Barber, I. Thorsos, K. L. Tanaka, N. G. Barlow, D. A. Fike, M. L. Urquhart, B. Grigsby, F. D. Grant, and O. de Goursac (2003). Exploring Gusev Crater with Spirit: Review of science objectives and testable hypotheses. *Journal of Geophysical Research*, **108**(E12), pp. 17–1. doi:10.1029/2002JE002026.
- Carling, P. A. (1996a). A preliminary palaeohydraulic model applied to Late-Glacial gravel dunes: Altai Mountains, Siberia. In Branson, J., A. G. Brown, and K. J. Gregory (eds.) *Global Continental Changes: the Context of Palaeohydrology*. Geological Society of London.
- Carling, P. A. (1996b). Morphology, sedimentology and palaeohydraulic significance of large gravel dunes, Altai Mountains, Siberia. *Sedimentology*, **43**, pp. 647–664.
- Carr, M. H. (1979). Formation of Martian flood features by release of water from confined aquifers. *Journal of Geophysical Research*, **84**, pp. 2995–3007.
- Carr, M. H. (1996). *Water on Mars*. Oxford University Press.
- Cassen, P., R. T. Reynolds, and S. J. Peale (1979). Is there liquid water on Europa. *Geophysical Research Letters*, **6**, pp. 731–734.

- Cattermole, P. (1990). Volcanic flow development at Alba Patera, Mars. *Icarus*, **83**, pp. 453–493.
- Chapman, M. G. (2002). *Volcano-Ice Interaction on Earth and Mars*, chapter Layered, massive and thin sediments on Mars: possible Late Noachian to Late Amazonian tephra?, pp. 273–293. Number 202 in Geological Society, London, Special Publications. The Geological Society of London.
- Chapman, M. G. and K. L. Tanaka (2001). Interior trough deposits on Mars: Subice volcanoes? *Journal of Geophysical Research*, **106**(E5), pp. 10087–10100.
- Christensen, P. R., J. L. Bandfield, J. F. Bell, N. Gorelick, V. E. Hamilton, A. Ivanov, B. M. Jakosky, H. H. Kieffer, M. D. Lane, M. C. Malin, T. McConnochie, A. S. McEwen, H. Y. McSween, G. L. Mehall, J. E. Moersch, K. H. Nealson, J. W. Rice, M. I. Richardson, S. W. Ruff, M. D. Smith, T. N. Titus, and M. B. Wyatt (2003a). Morphology and Composition of the Surface of Mars: Mars Odyssey THEMIS Results. *Science*, **300**(5628), pp. 2056–2061.
- Christensen, P. R., J. L. Bandfield, J. F. Bell, V. E. Hamilton, A. Ivanov, B. M. Jakosky, H. H. Kieffer, M. D. Lane, M. C. Malin, T. McConnochie, A. S. McEwen, H. Y. McSween, J. E. Moersch, K. H. Nealson, J. W. Rice, M. I. Richardson, S. W. Ruff, M. D. Smith, and T. N. Titus (2003b). Early Results from the Odyssey THEMIS Investigation. In *Lunar and Planetary Science XXXIV*, #1519. Lunar and Planetary Institute, Houston (CD-ROM).
- Christensen, P. R., J. L. Bandfield, R. N. Clark, K. S. Edgett, V. E. Hamilton, T. Hoefen, H. H. Kieffer, R. O. Kuzmin, M. D. Lane, M. C. Malin, R. V. Morris, J. C. Pearl, R. Pearson, T. L. Roush, S. W. Ruff, and M. D. Smith (2000). Detection of crystalline hematite mineralization on Mars by the Thermal Emission Spectrometer: Evidence for near-surface water. *Journal of Geophysical Research*, **105**(E4), pp. 9623–9642.

- Christensen, P. R., B. M. Jakosky, H. H. Kieffer, M. Malin, H. Y. McSween, K. Nealson, G. Mehall, S. Silverman, and S. Ferry (1999). The Thermal Emission Imaging System (THEMIS) Instrument for the 2001 Orbiter. In *Lunar and Planetary Science XXX*, #1470. Lunar and Planetary Institute, Houston (CD-ROM).
- Clifford, S. M. (1993). A model for the hydrologic and climatic behavior of water on Mars. *Journal of Geophysical Research*, **98**(E6), pp. 10973–11016.
- Crisp, J. A., M. Adler, J. R. Matijevic, S. W. Squyres, R. E. Arvidson, and D. M. Kass (2003). Mars Exploration Rover mission. *Journal of Geophysical Research*, **108**(E12), pp. 2–1. doi:10.1029/2002JE002038.
- Crumpler, L. S. and K. L. Tanaka (2003). Geology and MER target site characteristics along the southern rim of Isidis Planitia, Mars. *Journal of Geophysical Research*, **108**(E12), pp. 21–1. doi:10.1029/2002JE002040.
- Davis, P. A. and M. P. Golombek (1990). Discontinuities in the shallow Martian crust at Lunae, Syria, and Sinai Plana. *Journal of Geophysical Research*, **95**, pp. 14231–14248.
- Eliason, E. M., J. A. Anderson, J. M. Barrett, K. J. Becker, T. L. Becker, D. A. Cook, L. A. Soderblom, T. L. Sucharski, and K. T. Thompson (2001). ISIS Image Processing Capabilities for MGS/MOC Imaging Data. In *Lunar and Planetary Science XXXII*, #2081. Lunar and Planetary Institute, Houston (CD-ROM).
- Freeman, H. (ed.) (1980). *Interactive Computer Graphics*. EHO 156-0. Library of Congress no. 79-91237.
- Frey, H. (1979). Thaumasia - A fossilized early forming Tharsis uplift. *Journal of Geophysical Research*, **84**, pp. 1009–1023.
- Gaddis, L., J. Anderson, K. Becker, T. Becker, D. Cook, K. Edwards, E. Eliason, T. Hare, H. Kieffer, E. M. Lee, J. Mathews, L. Soderblom, T. Sucharski, J. Torson, A. McEwen, and M. Robinson (1997). An Overview of the Integrated Software

- for Imaging Spectrometers (ISIS). In *Lunar and Planetary Science Conference*, volume 28, p. 387.
- Garvin, J. B., J. J. Frawley, and J. B. Abshire (1999). Vertical roughness of Mars from the Mars Orbiter Laser Altimeter. *Geophysical Research Letters*, **26**(3), pp. 381–384.
- Golombek, M. P., J. A. Grant, T. J. Parker, D. M. Kass, J. A. Crisp, S. W. Squyres, A. F. C. Haldemann, M. Adler, W. J. Lee, N. T. Bridges, R. E. Arvidson, M. H. Carr, R. L. Kirk, P. C. Knocke, R. B. Roncoli, C. M. Weitz, J. T. Schofield, R. W. Zurek, P. R. Christensen, R. L. Fergason, F. S. Anderson, and J. W. Rice (2003). Selection of the Mars Exploration Rover landing sites. *Journal of Geophysical Research*, **108**(E12), pp. 13–1. doi:10.1029/2003JE002074.
- Golombek, M. P., H. J. Moore, A. F. C. Haldemann, T. J. Parker, and J. T. Schofield (1999). Assessment of Mars Pathfinder landing site predictions. *Journal of Geophysical Research*, **104**(E4), pp. 8585–8594.
- Greeley, R. and J. D. Iversen (1985). *Wind as a geological process on Earth, Mars, Venus, and Titan*. Cambridge University Press.
- Greeley, R. and P. D. Spudis (1981). Volcanism on Mars. *Reviews of Geophysics and Space Physics*, **19**, pp. 13–41.
- Haldemann, A. F. and F. S. Anderson (2002). Mars Exploration Rover Landing Site Hectometer Slopes. In *American Geophysical Union, Fall Meeting*, #P22A-0390.
- Head, J. W., J. F. Mustard, M. A. Kreslavsky, R. E. Milliken, and D. R. Marchant (2003). Recent ice ages on Mars. *Nature*, **426**, pp. 797–802.
- Hurford, T. A., R. A. Beyer, and R. Greenberg (2003). Flexure of Europa's lithosphere due to ridge-loading. *AAS/Division for Planetary Sciences Meeting*, **35**(#06.06).

- Hurford, T. A., B. Preblich, R. A. Beyer, and R. Greenberg (2004). Flexure of Europa's Lithosphere Due to Ridge-Loading. In *Lunar and Planetary Science XXXV*, #1831. Lunar and Planetary Institute, Houston (CD-ROM).
- Keszthelyi, L., A. S. McEwen, and T. Thordarson (2000). Terrestrial analogs and thermal models for Martian flood lavas. *Journal of Geophysical Research*, **105**(E6), pp. 15027–15050.
- Keszthelyi, L. and S. Self (1998). Some physical requirements for the emplacement of long basaltic lava flows. *Journal of Geophysical Research*, **103**(B11), pp. 27447–27464.
- Kirk, R. L., E. Howington-Kraus, T. Hare, E. Dorrer, D. Cook, K. Becker, K. Thompson, B. Redding, J. Blue, D. Galuszka, E. M. Lee, L. R. Gaddis, J. R. Johnson, L. A. Soderblom, A. W. Ward, P. H. Smith, and D. T. Britt (1999). Digital photogrammetric analysis of the IMP camera images: Mapping the Mars Pathfinder landing site in three dimensions. *Journal of Geophysical Research*, **104**(E4), pp. 8869–8888.
- Kirk, R. L., E. Howington-Kraus, B. Redding, D. Galuszka, T. M. Hare, B. A. Archinal, L. A. Soderblom, and J. M. Barrett (2003). High-resolution topomapping of candidate MER landing sites with Mars Orbiter Camera narrow-angle images. *Journal of Geophysical Research*, **108**(E12), pp. 29–1. doi:10.1029/2003JE002131.
- Kirk, R. L., K. T. Thompson, T. L. Becker, and E. M. Lee (2000). Photometric Modeling for Planetary Cartography. In *Lunar and Planetary Science XXXII*, #2025, pp. 2025–+. Lunar and Planetary Institute, Houston (CD-ROM).
- Kirk, R. L., K. T. Thompson, and E. M. Lee (2001). Photometry of the Martian Atmosphere: An Improved Practical Model for Cartography and Photoclinometry. In *Lunar and Planetary Science XXXII*, #1874. Lunar and Planetary Institute, Houston (CD-ROM).

- Komatsu, G., P. E. Geissler, R. G. Strom, and R. B. Singer (1993). Stratigraphy and erosional landforms of layered deposits in Valles Marineris, Mars. *Journal of Geophysical Research*, **98**(E6), pp. 11105–11121.
- Komatsu, G., G. G. Ori, P. Ciarcelluti, and Y. D. Litasov (2004). Interior layered deposits of Valles Marineris, Mars: analogous subice volcanism related to Baikal Rifting, Southern Siberia. *Planetary and Space Science*, **52**(1-3), pp. 167–187.
- Kuzmin, R. O., R. Greeley, R. Landheim, N. A. Cabrol, and J. D. Farmer (2000). *Geologic Map of the MTM-15182 and MTM-15187 Quadrangles, Gusev Crater-Ma'adim Vallis Region, Mars*. United States Geologic Survey.
- Lanagan, P. and A. S. McEwen (2004). Geomorphic Analysis of the Cerberus Plains: Constraints on the Emplacement of the Youngest Lava Flows on Mars. *Icarus*, **in revision**.
- Livingstone, I. and A. Warren (1996). *Aeolian Geomorphology: An Introduction*. Addison Wesley Longman Limited.
- Lopes, R. M. C. and C. R. J. Kilburn (1990). Emplacement of lava flow fields - Application of terrestrial studies to Alba Patera, Mars. *Journal of Geophysical Research*, **95**, pp. 14383–14397.
- Lucchitta, B. K. (1981). Valles Marineris - Faults, Volcanic Rocks, Channels, Basin Beds. In *Reports of Planetary Geology Program*, number 84211 in NASA Technical Memorandum, pp. 419–421.
- Lucchitta, B. K., N. K. Isbell, and A. Howington-Kraus (1994). Topography of Valles Marineris: Implications for erosional and structural history. *Journal of Geophysical Research*, **99**(E2), pp. 3783–3798.
- Lucchitta, B. K., A. S. McEwen, G. D. Clow, P. E. Geissler, R. B. Singer, R. A. Schultz, and S. W. Squyres (1992). The canyon system on Mars. In Kieffer, H. H., B. M. Jakosky, C. W. Snyder, and M. S. Matthews (eds.) *Mars*, chapter 14, pp. 453–492. The University of Arizona Press, Tucson.

- Malin, M. C., G. E. Danielson, A. P. Ingersoll, H. Masursky, J. Veverka, M. A. Ravine, and T. A. Soulanille (1992). Mars Observer Camera. *Journal of Geophysical Research*, **97**(E5), pp. 7699–7718.
- Malin, M. C. and K. S. Edgett (2000). Sedimentary Rocks of Early Mars. *Science*, **290**, pp. 1927–1937.
- Malin, M. C. and K. S. Edgett (2001). Mars Global Surveyor Mars Orbiter Camera: Interplanetary cruise through primary mission. *Journal of Geophysical Research*, **106**(E10), pp. 23429–23570.
- Masursky, H. (1973). An Overview of Geological Results from Mariner 9. *Journal of Geophysical Research*, **78**, pp. 4009–4030.
- McEwen, A. S. (1986). Exogenic and endogenic albedo and color patterns on Europa. *Journal of Geophysical Research*, **91**, pp. 8077–8097.
- McEwen, A. S. (1991). Photometric functions for photoclinometry and other applications. *Icarus*, **92**, pp. 298–311.
- McEwen, A. S., M. C. Malin, M. H. Carr, and W. K. Hartmann (1999). Voluminous volcanism on early Mars revealed in Valles Marineris. *Nature*, **397**, pp. 584–586.
- Mège, D., A. C. Cook, E. Garel, Y. Lagabriele, and M. Cormier (2003). Volcanic rifting at Martian grabens. *Journal of Geophysical Research*, **108**(E5), pp. 10–1. doi:10.1029/2002JE001852.
- Mège, D. and P. Masson (1996). Stress models for Tharsis formation, Mars. *Planetary and Space Science*, **44**, pp. 1471–1497.
- Milam, K. A., K. R. Stockstill, J. E. Moersch, H. Y. McSween, L. L. Tornabene, A. Ghosh, M. B. Wyatt, and P. R. Christensen (2003). THEMIS characterization of the MER Gusev Crater landing site. *Journal of Geophysical Research*, **108**(E12), pp. 19–1. doi:10.1029/2002JE002023.

- Milazzo, M. P., L. P. Keszthelyi, A. S. McEwen, and W. Jaeger (2003). The Formation of Columnar Joints on Earth and Mars. In *Lunar and Planetary Science XXXIV*, #2120. Lunar and Planetary Institute, Houston (CD-ROM).
- Minnaert, M. (1941). The reciprocity principle in lunar photometry. *Astrophys. J.*, **93**, pp. 403–410.
- Miyamoto, H., J. M. Dohm, R. A. Beyer, and V. R. Baker (2003). Rheological properties of slope streaks with anastomosing patterns on Mars. *AGU Fall Meeting Abstracts*, (#P42A-0423).
- Miyamoto, H., J. M. Dohm, R. A. Beyer, and V. R. Baker (2004a). Fluid dynamical implications of anastomosing slope streaks on Mars. *Journal of Geophysical Research*, **109**(E6). doi:doi:10.1029/2003JE002234.
- Miyamoto, H., J. M. Dohm, R. A. Beyer, and V. R. Baker (2004b). Numerical Simulations of Anastomosing Slope Streaks on Mars. In *Lunar and Planetary Science XXXV*, #1287. Lunar and Planetary Institute, Houston (CD-ROM).
- Morris, E. C. (1982). Aureole deposits of the Martian volcano Olympus Mons. *Journal of Geophysical Research*, **87**, pp. 1164–1178.
- Morris, E. C. and K. L. Jones (1980). Viking 1 Lander on the surface of Mars - Revised location. *Icarus*, **44**, pp. 217–222.
- Mouginis-Mark, P. and M. Tatsumura Yoshioka (1998). The long lava flows of Elysium Planitia, Mars. *Journal of Geophysical Research*, **103**(E8), pp. 19389–19400.
- Mouginis-Mark, P. J., L. Wilson, and M. T. Zuber (1992). The physical volcanology of Mars. In Kieffer, H. H., B. M. Jakosky, C. W. Snyder, and M. S. Matthews (eds.) *Mars*, chapter 13, pp. 424–452. The University of Arizona Press, Tucson.
- Mueller, K. and M. Golombek (2004). Compressional Structures on Mars. *Annual Review of Earth and Planetary Sciences*, **32**, pp. 435–464.

- Murchie, S., L. Kirkland, S. Erard, J. Mustard, and M. Robinson (2000). Near-Infrared Spectral Variations of Martian Surface Materials from ISM Imaging Spectrometer Data. *Icarus*, **147**(2), pp. 444–471.
- Mutch, T. A., R. E. Arvidson, E. A. Guinness, A. B. Binder, and E. C. Morris (1977). The geology of the Viking Lander 2 site. *Journal of Geophysical Research*, **82**, pp. 4452–4467.
- Nedell, S. S., S. W. Squyres, and D. W. Andersen (1987). Origin and evolution of the layered deposits in the Valles Marineris, Mars. *Icarus*, **70**, pp. 409–441.
- Neumann, G. A., J. B. Abshire, O. Aharonson, J. B. Garvin, X. Sun, and M. T. Zuber (2003). Mars Orbiter Laser Altimeter pulse width measurements and footprint-scale roughness. *Geophysical Research Letters*, **30**(11), pp. 15–1. doi: 10.1029/2003GL017048.
- Oberst, J., W. Zeitler, and M. Kuschel (2000). Where is Viking Lander 2? In *Lunar and Planetary Science XXXI*, #1612. Lunar and Planetary Institute, Houston (CD-ROM).
- Ori, G. G. and A. Karna (2003). The Uppermost Crust of Mars and Flood Basalts. In *Lunar and Planetary Science XXXIV*, #1539. Lunar and Planetary Institute, Houston (CD-ROM).
- Parker, T. J. and R. L. Kirk (1999). Location and Geologic Setting for the Three U.S. Mars Landers. In *Fifth International Conference on Mars*, #6124. Lunar and Planetary Institute, Houston (CD-ROM).
- Parker, T. J., R. L. Kirk, and M. E. Davies (1999). Location and Geologic Setting for the Viking 1 Lander. In *Lunar and Planetary Science XXX*, #2040. Lunar and Planetary Institute, Houston (CD-ROM).
- Peulvast, J.-P., D. Mège, J. Chiciak, C. François, and P. L. Masson (2001). Morphology, Evolution and Tectonics of Valles Marineris Wallslopes (Mars). *Geomorphology*, **37**, pp. 329–352.

- Reidel, S. P., T. L. Tolan, P. R. Hooper, M. H. Beeson, K. R. Fecht, R. D. Bentley, and J. L. Anderson (1989). The Grande Ronde Basalt, Columbia River Basalt Group; stratigraphic descriptions and correlations in Washington, Oregon, and Idaho. In Reidel, S. P. and P. R. Hooper (eds.) *Volcanism and Tectonism in the Columbia River Flood-Basalt Province*, number 239 in Special Papers (Geological Society of America), pp. 21–53. Geological Society of America, Inc.
- Richardson, M. I. and R. J. Wilson (2002). Investigation of the nature and stability of the Martian seasonal water cycle with a general circulation model. *Journal of Geophysical Research*, **107**, pp. 7–1. doi:10.1029/2001JE001536.
- Schorghofer, N., O. Aharonson, and S. Khatiwala (2002). Slope streaks on Mars: Correlations with surface properties and the potential role of water. *Geophysical Research Letters*, **29**(23), pp. 41–1. doi:10.1029/2002GL015889.
- Schultz, R. A. (1991). Structural development of Coprates Chasma and western Ophir Planum, Valles Marineris Rift, Mars. *Journal of Geophysical Research*, **96**, pp. 22777–22792.
- Schultz, R. A. (1997). Displacement-length scaling for terrestrial and Martian faults: Implications for Valles Marineris and shallow planetary grabens. *Journal of Geophysical Research*, **102**(B6), pp. 12009–12016.
- Schultz, R. A. (1998). Multiple-process origin of Valles Marineris basins and troughs, Mars. *Planetary and Space Science*, **46**, pp. 827–834.
- Schultz, R. A. (2000). Localization of bedding plane slip and backthrust faults above blind thrust faults: Keys to wrinkle ridge structure. *Journal of Geophysical Research*, **105**(E5), pp. 12035–12052.
- Schultz, R. A. (2002). Stability of rock slopes in Valles Marineris, Mars. *Geophysical Research Letters*, **29**(19), pp. 38–1. doi:10.1029/2002GL015728.

- Schultz, R. A. and K. L. Tanaka (1994). Lithospheric-scale buckling and thrust structures on Mars: The Coprates rise and south Tharsis ridge belt. *Journal of Geophysical Research*, **99**(E4), pp. 8371–8385.
- Sharp, R. P. (1973). Mars: Troughed Terrain. *Journal of Geophysical Research*, **78**, pp. 4063–4072.
- Shepard, M. K., B. A. Campbell, M. H. Bulmer, T. G. Farr, L. R. Gaddis, and J. J. Plaut (2001). The roughness of natural terrain: A planetary and remote sensing perspective. *Journal of Geophysical Research*, **106**(E12), pp. 32777–32796.
- Shorthill, R. W., R. E. Hutton, H. J. Moore, R. F. Scott, and C. R. Spitzer (1976a). Physical properties of the Martian surface from the Viking 1 lander - Preliminary results. *Science*, **193**, pp. 805–809.
- Shorthill, R. W., H. J. Moore, R. E. Hutton, R. F. Scott, and C. R. Spitzer (1976b). The environs of Viking 2 lander. *Science*, **194**, pp. 1309–1318.
- Smith, D. E., G. Neumann, P. Ford, R. E. Arvidson, E. A. Guinness, and S. Slavney (1999a). *Mars Global Surveyor Laser Altimeter Precision Experiment Data Record*. NASA Planetary Data System.
- Smith, D. E., M. T. Zuber, H. V. Frey, J. B. Garvin, J. W. Head, D. O. Muhleman, G. H. Pettengill, R. J. Phillips, S. C. Solomon, H. J. Zwally, W. B. Banerdt, T. C. Duxbury, M. P. Golombek, F. G. Lemoine, G. A. Neumann, and et al. (2001). Mars Orbiter Laser Altimeter: Experiment summary after the first year of global mapping of Mars. *Journal of Geophysical Research*, **106**(E10), pp. 23689–23722.
- Smith, D. E., M. T. Zuber, S. C. Solomon, R. J. Phillips, J. W. Head, J. B. Garvin, W. B. Banerdt, D. O. Muhleman, G. H. Pettengill, G. A. Neumann, F. G. Lemoine, J. B. Abshire, O. Aharonson, D. C. Brown, S. A. Hauck, A. B. Ivanov, P. J. McGovern, H. J. Zwally, and T. C. Duxbury (1999b). The Global Topography of Mars and Implications for Surface Evolution. *Science*, **284**(5419), p. 1495.

- Smith, P. H., J. F. Bell, N. T. Bridges, D. T. Britt, L. Gaddis, R. Greeley, H. U. Keller, K. E. Herkenhoff, R. Jaumann, J. R. Johnson, R. L. Kirk, M. Lemmon, J. N. Maki, M. C. Malin, S. L. Murchie, J. Oberst, T. J. Parker, R. J. Reid, R. Sablotny, L. A. Soderblom, C. Stoker, R. Sullivan, N. Thomas, M. G. Tomasko, W. Ward, and E. Wegryn (1997). Results from the Mars Pathfinder Camera. *Science*, **278**(5344), p. 1758.
- Soderblom, L. A., R. L. Kirk, and K. E. Herkenhoff (2002). Accurate Fine-Scale Topography for the Martian South Polar Region from Combining MOLA Profiles and MOC NA Images. In *Lunar and Planetary Science XXXIII*, #1254. Lunar and Planetary Institute, Houston (CD-ROM).
- Sullivan, R., P. Thomas, J. Veverka, M. Malin, and K. S. Edgett (2001). Mass movement slope streaks imaged by the Mars Orbiter Camera. *Journal of Geophysical Research*, **106**(E10), pp. 23607–23634.
- Tanaka, K. L. and M. P. Golombek (1989). Martian tension fractures and the formation of grabens and collapse features at Valles Marineris. In *Lunar and Planetary Science Conference XIX*, pp. 383–396.
- Thordarson, T. and S. Self (1998). The Roza Member, Columbia River Basalt Group: A gigantic pahoehoe lava flow field formed by endogenous processes? *Journal of Geophysical Research*, **103**(B11), pp. 27411–27445.
- Tolan, T. L., S. P. Reidel, M. H. Beeson, J. L. Anderson, K. R. Fecht, and D. A. Swanson (1989). Revisions to the estimates of the areal extent and volume of the Columbia River Basalt Group. In Reidel, S. P. and P. R. Hooper (eds.) *Volcanism and Tectonism in the Columbia River Flood-Basalt Province*, number 239 in Special Papers (Geological Society of America), pp. 1–20. Geological Society of America, Inc.
- Tufts, B. R. (1998). *Lithospheric Displacement Features on Europa and Their Interpretation*. Ph.D. thesis, The University of Arizona.

- Tufts, B. R., R. Greenberg, P. Geissler, G. Hoppa, R. Pappalardo, R. Sullivan, and Galileo Imaging Team (1997). Crustal displacement features on Europa. *Bulletin of the American Astronomical Society*, **29**(#12.05), p. 983.
- Tufts, B. R., R. Greenberg, G. Hoppa, and P. Geissler (2000). Lithospheric Dilation on Europa. *Icarus*, **146**(1), pp. 75–97.
- Turcotte, D. L. (1997). *Fractals and Chaos in Geology and Geophysics*. Cambridge University Press, New York.
- Turcotte, D. L. and G. Schubert (2002). *Geodynamics*. Cambridge University Press, Second edition.
- Ward, A. W. (1979). Yardangs on Mars - Evidence of recent wind erosion. *Journal of Geophysical Research*, **84**, pp. 8147–8166.
- Ward, A. W., L. R. Gaddis, R. L. Kirk, L. A. Soderblom, K. L. Tanaka, M. P. Golombek, T. J. Parker, R. Greeley, and R. O. Kuzmin (1999). General geology and geomorphology of the Mars Pathfinder landing site. *Journal of Geophysical Research*, **104**(E4), pp. 8555–8572.
- Watters, T. R. (1991). Origin of periodically spaced wrinkle ridges on the Tharsis Plateau of Mars. *Journal of Geophysical Research*, **96**, pp. 15599–15616.
- Watters, T. R. (1993). Compressional tectonism on Mars. *Journal of Geophysical Research*, **98**(E9), pp. 17049–17060.
- Weitz, C. M., T. J. Parker, M. H. Bulmer, F. Scott Anderson, and J. A. Grant (2003). Geology of the Melas Chasma landing site for the Mars Exploration Rover mission. *Journal of Geophysical Research*, **108**(E12), pp. 23–1. doi:10.1029/2002JE002022.
- Wessel, P. and W. H. F. Smith (1991). Free software helps map and display data. *EOS Trans. Amer. Geophys. U.*, **72**(41), pp. 441, 445–446.
- Wessel, P. and W. H. F. Smith (1998). New, improved version of Generic Mapping Tools released. *EOS Trans. Amer. Geophys. U.*, **79**(47), p. 579.

- Wilkins, S. J. and R. A. Schultz (2003). Cross faults in extensional settings: Stress triggering, displacement localization, and implications for the origin of blunt troughs at Valles Marineris, Mars. *Journal of Geophysical Research*, **108**(E6), pp. 10–1. doi:10.1029/2002JE001968.
- Williams, J., D. A. Paige, and C. E. Manning (2003). Layering in the wall rock of Valles Marineris: intrusive and extrusive magmatism. *Geophysical Research Letters*, **30**(12), pp. 25–1. doi:10.1029/2003GL017662.
- Williams, K. K. and R. Greeley (1998). Estimates of ice thickness in the Conamara Chaos region of Europa. *Geophysical Research Letters*, **25**(23), pp. 4273–4276.
- Williams, S. H. (1991). Dark Talus Streaks on Mars are Similar to Aeolian Dark Streaks. In *Lunar and Planetary Science XXII*, p. 1509. Lunar and Planetary Institute, Houston.
- Wilson, L. and J. W. Head (1994). Mars: Review and analysis of volcanic eruption theory and relationships to observed landforms. *Reviews of Geophysics*, **32**, pp. 221–263.
- Witbeck, N. E., K. L. Tanaka, and D. H. Scott (1991). *Geologic Map of the Valles Marineris Region, Mars*. MAP I-2010. United States Geologic Survey.
- Wolfe, R. (ed.) (1998). *Seminal Graphics: Pioneering Efforts That Shaped The Field*. ACM SIGGRAPH. ACM order no. 435985, ISBN 1-58113-052-X.
- Zeitler, W. and J. Oberst (1999). The Mars Pathfinder landing site and the Viking control point network. *Journal of Geophysical Research*, **104**(E4), pp. 8935–8942.
- Zuber, M. T. and L. L. Aist (1990). The shallow structure of the Martian lithosphere in the vicinity of the ridged plains. *Journal of Geophysical Research*, **95**, pp. 14215–14230.

Zuber, M. T., D. E. Smith, S. C. Solomon, D. O. Muhleman, J. W. Head, J. B. Garvin, J. B. Abshire, and J. L. Bufton (1992). The Mars Observer laser altimeter investigation. *Journal of Geophysical Research*, **97**(E5), pp. 7781–7797.